Searches for Gluino Mediated Sbottom Production with the ATLAS Detector

Thesis submitted in accordance with the requirements of the University of Liverpool for the degree of Doctor in Philosophy by

Graham John Sellers

November 2012

Abstract

A search for the supersymmetric process of gluino mediated $s$bottom production is presented. This search was carried out using 2.05 fb^{-1} of 7 TeV proton-proton collisions in the ATLAS detector at the LHC. The data used were collected during the 2011 ATLAS run.

In the search, six distinct signal regions are defined in order to identify candidate events for the signal process. These regions are distinguished by requiring events to possess an effective mass of at least 500 GeV, 700 GeV or 900 GeV and by requiring at least 1 b-jet or at least 2 b-jets in the final state. The data observed in these signal regions are compared to Monte Carlo simulation of known Standard Model processes, which form the background to this search.

No excess in the data above the Standard Model background is seen in any of the signal regions and therefore limits are set on the exclusion of this supersymmetric process in the gluino-$s$bottom mass plane. The limits set are derived from two distinctly different statistical foundations, one using a frequentist approach and the other using a Bayesian approach. The two methods are compared in the final limits they provide and are found to be in good agreement with one another.

Acknowledgements

Firstly, I would like to thank Sergey Burdin for his excellent supervision over a four year period, his help and assistance have been invaluable every step of the way. His patience with my questions and general guidance throughout has been very much appreciated. I would also like to thank Barry King for his general support and advice, especially with all things statistical and for his assistance with any technical issues when it comes to the setting of limits.

Special thanks also go to Paul Laycock and Monica D'Onofrio for everything they helped me out with throughout and for their general guidance in the field of supersymmetry and general assistance in programming related issues. Thanks too to Helen Hayward in all issues relating to ATLAS data quality, her help was always extremely useful and much appreciated.

I'd like to thank everybody in the ATLAS SUSY b-jets group for being so accepting and for all the answers they provided to my questions. A special thank you also to everyone in the University of Liverpool particle physics research group, in particular those who I had the pleasure of sharing an office with both at CERN and in Liverpool, for all their assistance along the way and for always making it such an enjoyable experience to work alongside them.

And finally, I would like to thank my family. My brother and my parents have always supported me every step of the way and without their support I would never have had the opportunity to undertake this thesis, or a degree in physics, in the first place.

Contents

Chapter 1

Introduction

Over the past century larger and more powerful particle accelerators have been constructed in order to create greater energies in the induced collisions of particles to facilitate the creation of previously undiscovered particles and probe matter at an ever deeper level. The latest, and currently most powerful, of these accelerators is the Large Hadron Collider (LHC). The LHC is a proton-proton collider located at CERN [1], built across the French-Swiss border near Geneva, Switzerland. It is a storage ring accelerator with a circumference of 27km.

There are four main detectors located around the LHC ring, each one located at a different interaction point. At these four interaction points the two beams of protons are brought together to induce collisions and the detectors are designed to record these 'events' for later analysis. The four detectors are ATLAS, CMS, LHCb and ALICE. Of these ATLAS and CMS are both general purpose detectors, which have been designed to look for new physics in as broad a spectrum as possible. In contrast the other two detectors both have very specialised functions. The LHCb detector is optimised for making precise measurements of events containing b-quarks with the primary goal of understanding the source and nature of CP violation. The ALICE experiment is focussed on the study of the quark-gluon plasma which is formed from the collision of the nuclei of lead atoms in place of the individual protons ordinarily used in the LHC.

This thesis presents an analysis carried out on the ATLAS experiment [2]. The main focus of this analysis is on the search for 'supersymmetry', which is one of the theoretically predicted forms of new physics that this experiment was designed to search for and which predicts a supersymmetric partner for each of the currently known particles. The motivation for this prediction will be introduced in the following chapter. Specifically, in this thesis, a search for the production of the supersymmetric partner of the bottom quark has been performed.

Thesis Outline

In chapter 2 an overview of the current Standard Model of particle physics is given, providing a platform for the introduction of supersymmetry and for an explanation of some of the motivations behind its introduction. The signal process central to this analysis is also introduced. In chapter 3 the LHC accelerator and the ATLAS detector in particular are described, including details of the various sub-detector systems and the roles they play in the recording of data and the subsequent analysis of the events within it. Chapter 4 describes the experimental data taking process and specifically the data quality procedures applied to this process, with a focus on the tools created to assist in judging this data quality in the SCT sub-detector. In chapter 5 the process of the reconstruction and identification of objects present within individual events from the recorded data is explained, this is done with a focus on the properties of events that are particularly important to this analysis. Chapter 6 presents a study of the performance of the methods used to identify the b-jets critical to this analysis. Chapter 7 details the primary analysis undertaken and a comparison of the results obtained from the data with Monte Carlo simulation. Chapter 8 describes the application of these results in producing confidence limits on the exclusion of this process in the gluino-$s$bottom mass plane and a discussion on a comparison of these limits using different independent statistical approaches. Finally, a summary of the results and conclusion are given in chapter 9.

Chapter 2

The Standard Model and Supersymmetry

In this chapter the theory of supersymmetry is introduced and the possibilities for the production of the particles it predicts, along with their possible experimental signatures at the LHC are discussed. In the first section the already experimentally established Standard Model of particle physics is introduced as a basis for providing a context for introducing supersymmetry as well as to outline some of the already known processes that will be discussed later. This introduction includes a description of the known fundamental particles and each of the forces that give rise to their interactions, but it also includes a discussion of its known incompleteness as a full description of nature at a fundamental level and some of its currently unsolved problems.

Finally, the supersymmetric 'signal' process, namely gluino mediated $s$bottom production, which is the focus of the analysis presented in this thesis, is introduced and the motivations for this particular search strategy are detailed.

2.1 The Standard Model

The Standard Model (SM) of particle physics is a theoretical framework which is currently the best description of the properties and interactions of the fundamental particles in nature. It describes these particles as fitting into one of two principal categories, depending on the property of quantum mechanical spin. Those particles which constitute physical matter and have a spin of $\frac{1}{2}$, known as *fermions*, are one group and those which transmit the forces through which all of the particles interact and have a spin of 1, known as *bosons*, are the second. Within the fermionic group of particles there exists a further sub-division giving rise to two separate families of fermions, *quarks* and *leptons*. These families are distinguished from one another by whether or not they are susceptible to the strong nuclear force, the quarks do experience the strong force whereas the leptons do not.

There are six different types of quarks, namely the *up, down, charm, strange, top* and *bottom* and six types of lepton, the *electron, electron neutrino, muon, muon neutrino, tau* and *tau neutrino*. The quarks possess the property of colour charge, the fundamental property which determines a particle's interaction with the strong force. There are three different values this property can take which are given the labels *red, green* and *blue* colour charge. This therefore means that there exist three distinct possible particles for each of the six types of quark, one quark possessing any of the three values of colour charge. The result is that there are a total of 18 fundamentally distinct types of quark in nature. Unlike the quarks, as the leptons do not experience the strong force, they do not carry this property and are thus colour charge neutral and exist in only 6 types.

All six types of quark and three of the leptons, the electron, muon and tau leptons, possess the property of electric charge and therefore experience the electromagnetic force. The property of electric charge, unlike colour charge, has only two values, labelled positive and negative. The neutrinos, which do not carry

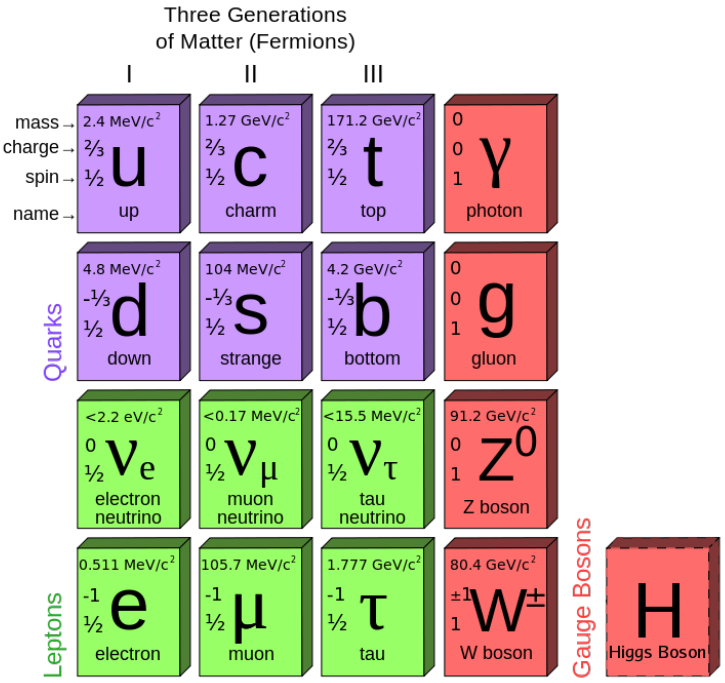

Figure 2.1: The elementary particles of the Standard Model of particle physics [3].

colour charge, do not possess this property either and therefore do not experience the strong force *or* the electromagnetic force. A corresponding anti-particle exists for every charged Standard Model particle, possessing the same mass and spin, but with an opposite electric charge. This means there are 36 (twice the set of 18) known distinct types of quarks/anti-quarks and up to twelve known types of lepton/anti-leptons.

The quarks and leptons are also divided into three separate generations where the masses of these fermionic particles are greatest in the third generation and smallest in the first generation. None of the fermions from the second or third generations are observed to be stable in nature, nor any hadrons comprised of these heavier fermions. Figure 2.1 shows a complete picture of the Standard Model particles, with the fermions separated into these three generations. Also shown along with each particle are its corresponding mass and internal quantum numbers of spin and electric charge.

In addition to the particles that make up matter there are four known fundamental forces in nature which mediate their interactions with one another, two of which have been discussed already in the context of their role in helping to categorise the particles. Of these four forces only three are described by the Standard Model, these are electromagnetism, the strong nuclear force and the weak nuclear force. Each of these forces has its own corresponding gauge boson(s), shown in red in figure 2.1 above. Electromagnetism has the *Photon* (γ), the Strong force has the *gluon* (g) and the Weak force has the $W^{\pm}$ and Z bosons, these forces and their respective gauge bosons will be discussed in detail in the following sections. There are 8 different types of gluon as they can be viewed as carrying any *two* values of the colour charge property[1]. The photon, gluons and Z boson are their own anti-particles and the W^+ and W^- are anti-particles of each other. As is summarised in figure 2.2, this means that, with 24 fermions, 24 anti-fermions, 12 gauge bosons and 1 Higgs boson, there are a total of 61 fundamentally distinct particles described by the Standard Model.

Particle	# Types	# Generations	Anti-particle	Colours	Total
Quarks	2	3	Yes	3	**36**
Leptons	2	3	Yes	-	**12**
Gluons	1	1	No	8	**8**
W boson	1	1	Yes	-	**2**
Z boson	1	1	No	-	**1**
Photon	1	1	No	-	**1**
Higgs boson	1	1	No	-	**1**
Total Standard Model Particles					**61**

Figure 2.2: A summary of the total particles content of the Standard Model [4].

The fourth fundamental force, Gravity, currently has no accepted quantum mechanical description and hence no corresponding gauge boson (the hypothetical

[1]Though in reality they can be in a superposition of multiple states such as $(r\bar{b} + \bar{r}b) / \sqrt{2}$, where r = red and b = blue colour charge.

Graviton) appears in the Standard Model. One further gauge boson which does appear in the Standard Model is the Higgs Boson and it is through interactions with this boson that the other particles are provided with their mass.

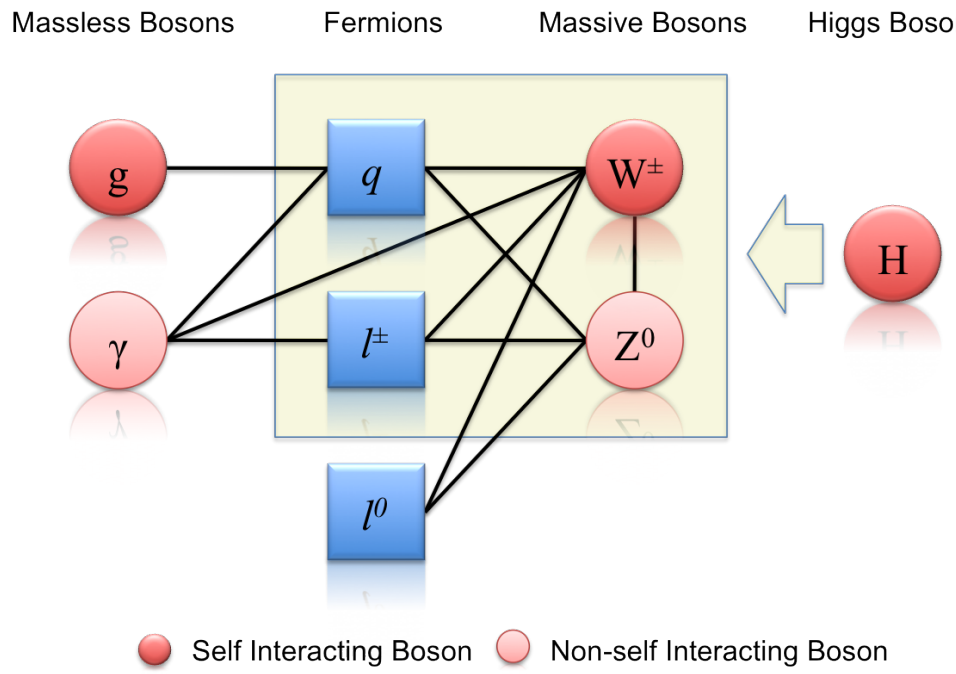

Figure 2.3: A summary of the possible interactions between the different Standard Model particles.

Not every particle (fermion or boson) in the Standard Model couples to all of the gauge bosons and if a particle doesn't couple to the boson that propagates a particular force then that particle doesn't experience that force in any way. In addition to this coupling with other bosons some of the bosons 'self-interact', which means that they themselves experience the force that they propagate. The combination of possible interactions described by the Standard Model is illustrated in figure 2.3. As can be seen the gluon only couples to the quarks and itself, no other particles experience the strong nuclear force. The photon couples to all of the quarks and the three charged leptons as well as the $W^{\pm}$ bosons, but is itself electrically neutral and so doesn't self interact. The $W^{\pm}$ and Z bosons couple to

all the fermions in the Standard Model which results in them all being susceptible to the weak nuclear force and they also couple to each other. As alluded to above, the Higgs boson couples to any particle with mass and is the means by which they are endowed with their mass, this includes itself via self-interaction, the $W^{\pm}$ and Z bosons of the weak nuclear force and all of the fermions[2]. The Higgs doesn't couple to either the gluon or the photon and they are massless.

The full symmetry group of the Standard Model is $SU(3) \times SU(2)_L \times U(1)_Y$. The $SU(3)$ component gives rise to the strong nuclear force, and $SU(2)_L \times U(1)_Y$ describes the electroweak interaction, where the label L denotes the fact that the weak nuclear force only acts on chirally *left*-handed particles and the label Y denotes that $U(1)_Y$ acts on a particles *weak hypercharge*[3]

2.1.1 Quantum Electrodynamics

The first theory developed of those which today form the heart of the Standard Model was that describing the Electromagnetic force, *Quantum Electrodynamics* (QED). This theory describes how the electrically charged particles of the Standard Model interact via the exchange of the quantum of the electromagnetic field, the photon.

This is achieved in QED with the introduction of the Dirac Lagrangian describing a free fermion field ψ for a particle with spin $\frac{1}{2}$ and mass m [5]

$$\mathcal{L}_D = \bar{\boldsymbol{\psi}}(i\gamma^\mu \partial_\mu - m)\boldsymbol{\psi}, \tag{2.1}$$

where γ^μ are the Dirac γ matrices. This Lagrangian is invariant under *global* $\boldsymbol{U}(1)$ transformations, meaning that in this form it acts on the field the same way

[2]With the caveat that in the conventional Standard Model the neutrinos *don't* interact with the Higgs boson, this situation is explained in section 2.2.1

[3]$Y = 2(q - I_3)$, where q is the particles electric charge and I_3 is the third component of isospin.

at every point in space-time, but it is not invariant under *local* transformations where there is an explicit space-time dependence, such as

$$\boldsymbol{\psi}(x,t) \longrightarrow e^{-iq\chi(x,t)}\boldsymbol{\psi}(x,t), \tag{2.2}$$

where $\chi(x,t)$ is an arbitrary, space-time dependent, function. In order to turn this Lagrangian from a globally into a locally invariant one, the 'gauge principle' is invoked whereby the standard derivative ∂_μ is replaced by the covariant derivative $\boldsymbol{D}_\mu = \partial_\mu + iq\boldsymbol{A}_\mu$. Here, what is called the gauge field, $\boldsymbol{A}_\mu$, is introduced as an extra term in this covariant form and this field is defined as transforming under the $\boldsymbol{U}(1)$ transformation as

$$\boldsymbol{A}_\mu \longrightarrow \boldsymbol{A}_\mu + \partial_\mu\chi. \tag{2.3}$$

The propagation of this field is described by an appropriately gauge invariant kinetic term in the Lagrangian, which is given by

$$\mathcal{L}_{Kinetic} = -\frac{1}{4}\boldsymbol{F}_{\mu\nu}\boldsymbol{F}^{\mu\nu}, \tag{2.4}$$

where $\boldsymbol{F}_{\mu\nu}$ is defined in terms of the covariant derivative whose definition is given above, so $\boldsymbol{F}_{\mu\nu} = \frac{i}{q}[\boldsymbol{D}_\mu, \boldsymbol{D}_\nu] = \partial_\mu\boldsymbol{A}_\nu - \partial_\nu\boldsymbol{A}_\mu$. So with the introduction of this kinetic term the final form of the QED Lagrangian is

$$\mathcal{L}_D = \bar{\boldsymbol{\psi}}(x)(i\gamma^\mu\boldsymbol{D}_\mu - m)\boldsymbol{\psi}(x) - \frac{1}{4}\boldsymbol{F}_{\mu\nu}\boldsymbol{F}^{\mu\nu}. \tag{2.5}$$

This form of the Lagrangian describes the interaction of the original spin $\frac{1}{2}$ particle with the gauge field $\boldsymbol{A}_\mu$ and this field, when quantized, is the quantum

of electromagnetism, the photon. This photon must be massless as inserting a mass term into this Lagrangian would destroy the local gauge invariance.

2.1.2 The Electroweak Model and Symmetry Breaking

The theory of the weak nuclear force describes the interaction of Standard Model particles through the exchange of $W^{\pm}$ and Z^0 bosons. Unlike electromagnetism, *every* Standard Model fermion feels the influence of the weak force, as seen in figure 2.3 above. Additionally unlike the photon of electromagnetism, the $W^{\pm}$ and Z^0 bosons possess mass, the result of this being that, whereas the range of the electromagnetic force is infinite, the weak force operates only on distance scales $\sim 10^{-18}$ metres [6].

In the Standard Model, however, these two forces are not independent of each other, but different manifestations of the same underlying force. This description is realised through the electroweak model, which unifies the electromagnetic and weak nuclear forces under the gauge group $SU(2)_L \times U(1)_Y$. The introduction of this group produces three corresponding gauge boson states for the $SU(2)_L$ component, $\mathbf{W}^i_\mu$ where (i = 1, 2, 3), and one for the $U(1)_Y$ component, $\mathbf{B}_\mu$. The coupling constants, defining the strength of the interaction in each case, are g and g' respectively.

The concept of electroweak symmetry breaking arises from what is known as the 'Higgs Mechanism' [7]. This mechanism breaks the $SU(2)_L \times U(1)_Y$ symmetry through the introduction of an $SU(2)_L$ doublet of a complex scalar field ϕ, which is defined as

$$\phi(x) = \begin{pmatrix} \phi^\dagger \\ \phi^0 \end{pmatrix} = \frac{1}{\sqrt{2}} \begin{pmatrix} \phi_1(x) + i\phi_2(x) \\ \phi_3(x) + i\phi_4(x) \end{pmatrix}. \tag{2.6}$$

The effect of this doublet appearing in the Higgs Lagrangian shown in equation 2.7 gives rise to the 'Higgs boson' and, if treated with a method obeying

local gauge invariance, also produces mass terms for the gauge bosons.

$$\mathcal{L}_H = (\partial_\mu \phi)^\dagger (\partial^\mu \phi) - \frac{\lambda}{2}\left(\phi^\dagger \phi - \frac{1}{2}\phi_0^2\right)^2. \tag{2.7}$$

The two physical W bosons of the Standard Model, described above, can now both be described as mixtures of the first two $\mathbf{W}_\mu$ states, as follows

$$W^+ = \frac{\mathbf{W}_\mu^1 + i\mathbf{W}_\mu^2}{\sqrt{2}}, \tag{2.8}$$

$$W^- = \frac{\mathbf{W}_\mu^1 - i\mathbf{W}_\mu^2}{\sqrt{2}}. \tag{2.9}$$

The Z boson and photon field, A, similarly result from the mixing of the third $\mathbf{W}_\mu$ and $\mathbf{B}_\mu$ states

$$A = \mathbf{W}_\mu^3 \sin\theta_W + \mathbf{B}_\mu \cos\theta_W, \tag{2.10}$$

$$Z = \mathbf{W}_\mu^3 \cos\theta_W - \mathbf{B}_\mu \sin\theta_W, \tag{2.11}$$

where $\theta_W = \tan^{-1}(g'/g)$ is the electroweak mixing angle or 'Weinberg angle', which is a free parameter of the theory and, as shown in equations 2.10 and 2.11, describes the degree of mixing between the weak boson states $\mathbf{W}_\mu^3$ and $\mathbf{B}_\mu$.

Although the absolute value for the masses of the electroweak bosons is another free parameter of the theory, the ratio between the mass of the W and that of the Z boson in terms of this mixing angle is given by $M_W/M_Z = \cos\theta_W$. The experimentally measured mass of the $W^\pm$ bosons is, $m_{W^\pm} = 80.399 \pm 0.023$ GeV and that of the Z^0 boson, $m_{Z^0} = 91.1876 \pm 0.0021$ GeV, with an additional experimental constraint on the difference between the two W masses of, $m_{W^+} - m_{W^-} = -0.2 \pm 0.6$ GeV [8].

2.1.3 Quantum Chromodynamics

The interactions between particles through the strong nuclear force are explained in the Standard Model by the theory of *Quantum Chromodynamics* (QCD), which gives rise to the gluons as the mediating bosons of this force. The symmetry group in this theory is SU(3) and this remains an unbroken symmetry in nature, the consequence of which is that the gluons are massless, like the photon of electromagnetism, but unlike the W and Z bosons of the weak nuclear force described in the previous section. The Lagrangian of QCD is given by

$$\mathcal{L}_{QCD} = \sum_q \bar{\psi} \left(i\gamma^\mu \delta_{ab} - g_s \gamma^\mu t^C_{ab} \mathcal{A}^C_\mu - m_q \delta_{ab} \right) \psi - \frac{1}{4} F^A_{\mu\nu} F^{A\mu\nu}, \tag{2.12}$$

where the repeated indices are summed over and the colour index a runs from $a = 1$ to $N_a = 3$, representing the three different types of quark colour charge. The γ^μ are the Dirac γ-matrices, $\psi_{q,a}$ are quark field spinors for a quark of flavour q and mass m_q and g_s is the QCD coupling constant. The terms of $\mathcal{A}^C_\mu$ correspond to the interacting gluon fields with C running from 1 to $N_a^2 - 1 = 8$, representing the eight different types of gluon. The field tensor, $F_{\mu\nu}$ is given by

$$F^A_{\mu\nu} = \partial_\mu \mathcal{A}^A_\nu - \partial_\nu \mathcal{A}^A_\mu - g_s f_{ABC} \mathcal{A}^B_\mu \mathcal{A}^C_\nu, \tag{2.13}$$

where f_{ABC} are the structure constants of the SU(3) group. Unlike the electroweak theories, QCD is a non-abelian gauge theory, which gives rise to the gluon self-interaction. This means that just like the quarks the gluons themselves experience the strong force that they transmit.

2.2 Problems with the Standard Model

Despite the successes of the Standard Model, such as the numerous experimental confirmations and level of accuracy of many of its predictions, the theory leaves open questions and there are various issues relating to it, which suggest that it is very unlikely to be a complete or final description of matter and the fundamental forces. The following sections outline some of these issues.

2.2.1 Neutrino Masses

When any particle interacts with a Higgs Boson its chirality is inverted[4], meaning a left-handed particle becomes a right-handed particle and vice-versa. Unlike all other particles, only left-handed neutrinos (and right-handed anti-neutrinos) are observed to exist in nature and so the conventional Standard Model predicts that, as they have no chirally opposite counterparts to transform between, they therefore do not acquire mass through this method and must be mass-*less*.

This, however, is not observed to be the case experimentally [9]. Experiments have found evidence for a phenomenon known as neutrino oscillation, a process by which neutrinos oscillate between the three different neutrino types (the electron, muon and tau flavours of neutrino). This process is only possible if the neutrinos possess a non-zero mass.

This apparent contradiction is less of a problem for the Standard Model than the other issues that will be described in this section as, although the source of the neutrino masses is currently unknown, it is possible to resolve this issue entirely within the context of the current framework in a number of different ways. One of these solutions is through the presumption of the existence of right-handed neutrinos which, necessarily, must interact much more weakly with the W and Z bosons than their left-handed counter-parts and thus have not been observed,

[4]The chirality of a particle refers to the direction of its spin vector in relation to its motion, in right-handed particles the two are aligned, in left-handed they are opposite

but whose existence allows for the generation of mass in the observed neutrinos in the same way as other massive particles. Alternatively, very massive right-handed neutrinos could exist whose mass could preclude their coupling to the W and Z bosons, but nonetheless allow for the very light neutrino masses observed.

There also exist possible solutions that do lie outside the confines of the current Standard Model, such as those provided by some supersymmetric models [10], but these particular models of supersymmetry are not a focus of this thesis and therefore are not discussed in detail here.

2.2.2 Grand Unification

It is known that no full unification of all the Standard Model forces occurs when their respective coupling constants are extrapolated to higher energy scales. If these coupling constants are α_1, α_2 and α_3, then they can be defined as [11]

$$\alpha_1 = \frac{5}{3}\frac{g'^2}{4\pi} = \frac{5\alpha}{3}\cos^2\theta_W, \tag{2.14}$$

$$\alpha_2 = \frac{g^2}{4\pi} = \frac{\alpha}{\sin^2\theta_W}, \tag{2.15}$$

$$\alpha_3 = \frac{g_s^2}{4\pi}, \tag{2.16}$$

where α is the fine structure constant, g, g' and g_s are the $U(1)_Y, SU(2)_L$ and $SU(3)$ coupling constants respectively and θ_W is the weak mixing angle introduced above. Assuming the Standard Model is valid up to the unification scale, the three coupling constants α_i (where $i = 1, 2, 3$) are inversely proportional to $log\,(Q^2)$ where Q is the the energy scale and can be given by

$$\frac{1}{\alpha_i(Q^2)} = \frac{1}{\alpha_i(\mu^2)} - \frac{b_i}{4\pi} ln\left(\frac{Q^2}{\mu^2}\right), \tag{2.17}$$

where for the Standard Model the coefficients b_i are given by

$$b_i^{SM} = \begin{pmatrix} b_1 \\ b_2 \\ b_3 \end{pmatrix} = \begin{pmatrix} 0 \\ -22/3 \\ -11 \end{pmatrix} + N_{Gen} \begin{pmatrix} 4/3 \\ 4/3 \\ 4/3 \end{pmatrix} + N_{Higgs} \begin{pmatrix} 1/10 \\ 1/6 \\ 0 \end{pmatrix}, \tag{2.18}$$

where N_{Gen} is the number of generations of fermions and N_{Higgs} is the number of Higgs doublets. In the Standard Model $N_{Gen} = 3$ and $N_{Higgs} = 1$, this gives the components of b_i as $b_1 = 41/10$, $b_2 = -19/6$ and $b_3 = -7$. The result of this dependence of $1/\alpha_i$ on the energy scale is shown on the left in figure 2.4.

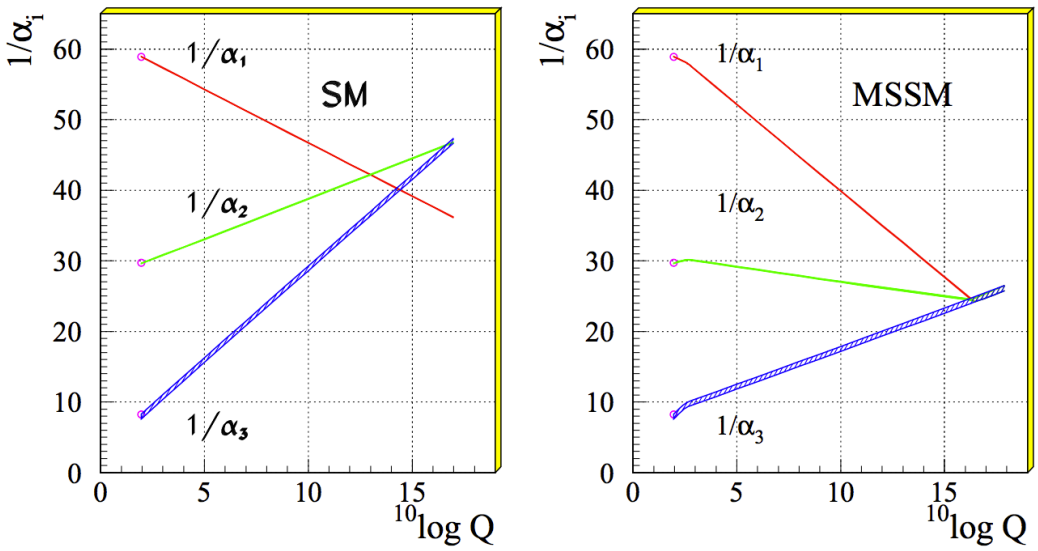

Figure 2.4: Extrapolation from LEP data to higher energy scales of the coupling constants, in the Standard Model (left) and in MSSM (right) [11].

In one form of Supersymmetry known as the 'Minimal Supersymmetric Standard Model' (MSSM), introduced in section 2.3.1, these coefficients are modified due to the introduction of the new set of supersymmetric particles and are then given by

$$b_i^{MSSM} = \begin{pmatrix} b_1 \\ b_2 \\ b_3 \end{pmatrix} = \begin{pmatrix} 0 \\ -6 \\ -9 \end{pmatrix} + N_{Gen} \begin{pmatrix} 2 \\ 2 \\ 2 \end{pmatrix} + N_{Higgs} \begin{pmatrix} 3/10 \\ 1/2 \\ 0 \end{pmatrix}, \tag{2.19}$$

where in this case $N_{Gen} = 3$ as before, but $N_{Higgs} = 2$, which gives correspondingly $b_1 = 33/5$, $b_2 = 1$ and $b_3 = -3$. If the mass scale of the supersymmetric particles is of the order of 1 TeV then [12], as seen on the right in figure 2.4, the three coupling constants may be unified at an energy scale $\sim 10^{16}$ GeV. This is one motivation for the search for supersymmetry.

2.2.3 The Hierarchy Problem

The Hierarchy problem arises from the fact that the absolute strengths of the forces described by the Standard Model are so significantly different in magnitude and that the energy scale at which quantum gravity becomes comparable to these forces is so different to that at which all the currently known Standard Model particles reside.

This energy scale at which quantum gravity becomes non-negligible is known as the Planck scale $M_P = (8\pi G_N)^{-\frac{1}{2}} \simeq 2.4 \times 10^{18}$ GeV, where G_N is the gravitational constant [13]. As the electroweak scale, the current limit of experimental exploration, is $M_W \sim 100$ GeV, the ratio of the two M_P/M_W is some 16 orders of magnitude.

This problem is also related to the stability of the Higgs mass. The electrically neutral part of the Standard Model Higgs field is a complex scalar H with a classical potential of

$$V = m_H^2|H|^2 + \lambda|H|^4. \tag{2.20}$$

The Standard Model requires a non-zero vacuum expectation value for the Higgs field H at the minimum point of this potential. If $\lambda > 0$ and $m_H^2 < 0$ then this will be the case and this value $\langle H \rangle = \sqrt{-m_H^2/2\lambda}$. It is know experimentally from measurements on the nature of the weak interaction that $\langle H \rangle \sim 174$ GeV and therefore m_H^2 is very approximately of the order of $-(100 \text{ GeV})^2$. However, m_H^2 should receive quantum corrections to its value from the virtual effects of every particle that it couples to, the overall result being huge.

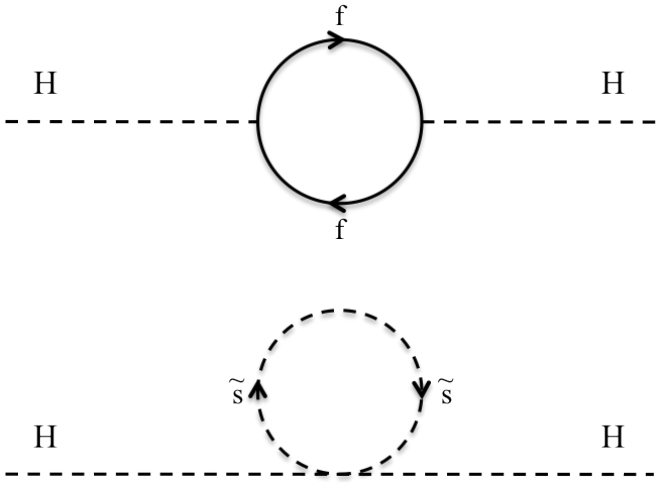

Figure 2.5: One loop quantum corrections to the Higgs Mass squared, m_H^2, due to a SM fermion f (above) and a supersymmetric scalar $\widetilde{s}$ (below).

This phenomenon is illustrated in figure 2.5, where in the first process the Higgs field couples to a Standard Model fermion f, leading to a correction

$$\Delta m_H^2 = -\frac{|\lambda_f|^2}{8\pi^2}\Lambda_{UV}^2 + \dots \tag{2.21}$$

where λ_f is the coupling constant and Λ_{UV} is an energy scale cutoff interpreted as the limit up to which the Standard Model is valid with no new required physics additions. If there is no new physics beyond the Standard Model up to the Planck scale then the Higgs mass will diverge.

One, but not the only, possible resolution to this problem is through the postulation of a whole new set of scalar particles. As illustrated by the second process in figure 2.5, if there exists a heavy complex scalar particle $\widetilde{s}$ with a mass $m_{\widetilde{s}}$ that also couples to the Higgs, then this leads to further corrections of the form

$$\Delta m_H^2 = \frac{|\lambda_{\widetilde{s}}|^2}{16\pi^2}[\Lambda_{UV}^2 - 2m_{\widetilde{s}}^2 \ln(\Lambda_{UV}/m_{\widetilde{s}}) + \ldots] \tag{2.22}$$

If these hypothetical scalar particles couple to the Higgs with a strength, relative to the Standard Model fermions, of $\lambda_s \sim |\lambda_f|^2$ then the first terms of equations 2.21 and 2.22 cancel with each other and the two sets of particles together prevent the divergence of the Higgs mass. As supersymmetry introduces just this set of particles this is a potentially strong theoretical motivation in its favour.

2.2.4 Dark Matter

It is known from astronomical observations that the physical matter visible to us only makes up approximately 4% of the total matter in the universe [8]. The other 96% is thought to come from Dark Matter (∼23%) and Dark Energy (∼73%), the term *Dark* Matter here refers to the fact that this must be a non-luminous and non-absorbing form of matter.

Measurements of the anisotropy of the Cosmic Microwave Background (CMB) radiation and the spatial distribution of galaxies in the Universe give a density of non-baryonic matter (Ω_{non-b}) of [8]

$$\Omega_{non-b}h^2 = 0.110 \pm 0.006, \tag{2.23}$$

where h is the Hubble constant in units of 100 km/(s · Mpc). Whereas the baryonic matter density (Ω_b) is measured as

$$\Omega_b h^2 = 0.0227 \pm 0.0006. \tag{2.24}$$

So although some of the contribution to Dark Matter may come from baryonic sources, such as 'Massive Compact Halo Objects' (MACHOs) [14] or cold molecular gas clouds [15], this can only account for at most ∼20% of total Dark Matter. The rest must come from non-baryonic sources. None of the established particles in the Standard Model can account for this share of the Dark Matter contribution.

There are various suggestions as to the source, or sources, of this unseen contribution to mass in the Universe, but its nature is currently unknown. In some forms of supersymmetry, those where a quantity known as R-parity (discussed in section 2.3.2) is conserved, the lightest of the supersymmetric particles cannot decay, it must be stable, and is thus a possible candidate for constituting Dark Matter.

2.2.5 Gravity

As mentioned previously, three of the four known fundamental forces in nature are represented in the Standard Model, but gravity is not. The force of gravity is described by the theory of General Relativity as resulting from the curvature of space-time, but in the quantum field theories of the Standard Model the gauge fields corresponding to the other forces are described in a flat-space time. Therefore, when an attempt is made to describe gravity in the same way as the other three forces the description breaks down, running into renormalisation problems, generating irreconcilable infinities and failing to produce finite testable results.

Analogous to the Standard Model interpretation of the other forces, this ap-

proach attempts to introduce the idea that the attractive force between two objects of mass again arises from the exchange of gauge bosons, in this case gravitons. In one supersymmetric model, *minimal supergravity* (mSUGRA), the graviton and its supersymmetric equivalent, the *gravitino*, are introduced naturally providing one possible solution to this particular problem.

2.3 Supersymmetry

Although the predictions that the Standard Model *does* make agree to an exceptionally accurate level with experiment, it is nevertheless known for a variety of reasons (partially discussed in the previous sections) that it cannot be a complete description of nature at the fundamental particle level. There must therefore be new physics that exists beyond the Standard Model to account for this incompleteness and many possible theories have been suggested in an attempt to solve these problems, and from a theoretical point of view Supersymmetry (SUSY) is one of the most promising.

The premise of supersymmetry is that of introducing a symmetry between the Fermions and Bosons of the Standard Model, thus predicting the existence of a corresponding Boson (integer spin) for every Standard Model Fermion (half-integer spin) and a corresponding Fermion for every Boson. If supersymmetry was an *un*broken symmetry then every one of these supersymmetric partners would have the same mass and internal quantum numbers (apart from the inherently modified spin) as its Standard Model equivalent. As no such particles have been observed, if it exists, supersymmetry must be a broken symmetry and the masses of the predicted particles must be heavier than their Standard Model equivalents. These masses can in principle take on any heavier value in a broken symmetry, but to help solve the problems of the Standard Model they must be of the order of the TeV scale.

2.3.1 The Minimal Supersymmetric Standard Model

A common approach to the study of supersymmetry is to assume the minimum possible particle content of the new model, this is the 'Minimal Supersymmetric Standard Model' or MSSM for short. The new particles predicted by this model are introduced below and illustrated in figure 2.6. The conventional MSSM naming scheme is used in order to help keep track of the many new particle names required. This scheme assigns the prefix *s-* (standing for *scalar-*) to an SM fermions name to give its MSSM equivalent (fermion $\longrightarrow$ *s*fermion) and the suffix *-ino* is given to the end of an SM bosons name to give its equivalent (boson $\longrightarrow$ bos*ino*).

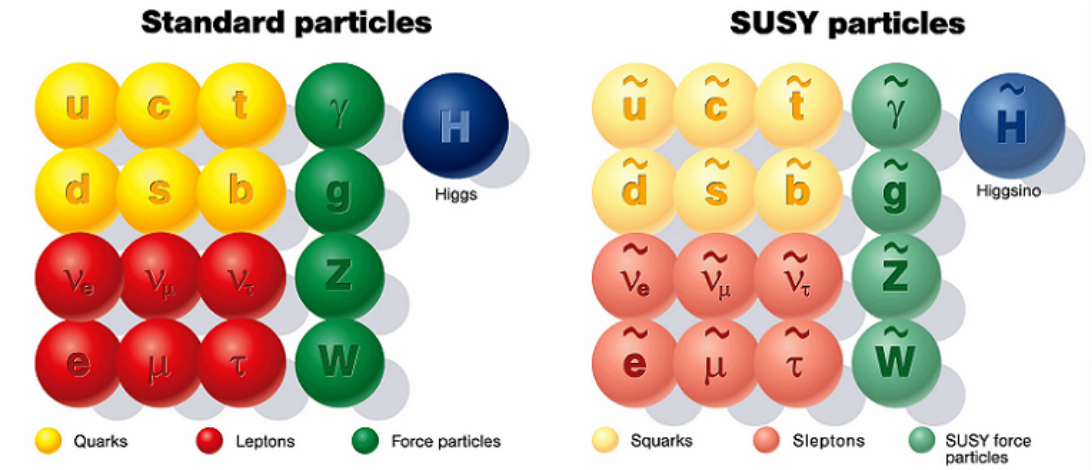

Figure 2.6: The Standard Model particles introduced above alongside their predicted supersymmetric (MSSM) partners [16].

squarks

The *s*quarks or the scalar quarks are the supersymmetric equivalent of the SM quarks, shown in yellow in figure 2.6. As stated above their properties are identical apart from their spin and their unknown masses, the spin of the *s*quarks is 0 in place of $\frac{1}{2}$ for the quarks, hence *scalar* quarks.

Symbolically they are represented by the same letter as their Standard Model partners, except for the addition of a tilde (˜) appended above, this tilde is the distinguishing mark of a SUSY particle symbolically. Their individual names are given in the same manner as the group as a whole, prefixing an *s*- before the name of the individual SM quark, for example the *s*top or the *s*bottom, which is the focus of this analysis.

sleptons

The *s*leptons or the scalar leptons are the supersymmetric equivalent of the SM leptons, shown in red in figure 2.6. Like the *s*quarks the *s*leptons have the same properties as their SM partners other than their spin and mass, and also like the *s*quarks the spin of the *s*leptons is 0.

The names assigned to the individual *s*leptons follows the same pattern as for the *s*quarks, with a prefixed *s*- appearing before the name, for example the *s*electron, *s*muon, *s*tau and *s*neutrino.

gluinos

The gluino, shown in green in figure 2.6, is the supersymmetric partner of the SM gluon, in place of the gluon being spin-1, the gluino is a spin-$\frac{1}{2}$ fermion. The symbol used to represent the gluino is $\widetilde{g}$.

Winos and Zinos

The supersymmetric partners of the Standard Model W and Z bosons are the Wino and Zino respectively. They both possess a spin of $\frac{1}{2}$ and are represented by the equivalent symbols $\widetilde{W}$ and $\widetilde{Z}$. Like their Standard Model counterparts the winos are electrically charged and the zino is electrically neutral. They are also shown in green in figure 2.6.

Higgsinos

The Higgsino is the supersymmetric partner of the Standard Model Higgs boson and has a spin of $\frac{1}{2}$, compared with the scalar SM Higgs, shown in blue in figure 2.6.

Neutralinos and Charginos

Neutralinos and charginos are supersymmetric partners of the Standard Model gauge bosons. They are not individually identified as the direct equivalents of individual gauge bosons, but instead each of the states representing them are seen as linear combinations of the states of the different supersymmetric gauginos. In MSSM there are four distinct neutralinos and two charginos, each a mix of these different gaugino states.

The four neutralinos (referred to, in order of increasing mass, as $\widetilde{\chi}_1^0, \widetilde{\chi}_2^0, \widetilde{\chi}_3^0, \widetilde{\chi}_4^0$) are mixed states of the zino and neutral higgsinos, and they are each identified as their own anti-particles. The two charginos ($\widetilde{\chi}_1^{\pm}, \widetilde{\chi}_2^{\pm}$) are mixed states of the winos and charged higgsinos.

In the supersymmetric model considered in this thesis the lightest neutralino ($\widetilde{\chi}_1^0$) is identified as the lightest of all the supersymmetric particles.

Gravitino

Finally, the gravitino is the supersymmetric partner of the, still unobserved, graviton. It is predicted by supergravity theories which combine together supersymmetry and general relativity.

2.3.2 *R*-parity

In the MSSM form of Supersymmetry it is necessary to introduce a new concept if the conservation of either baryon or lepton number are not to be violated. This is referred to as R-parity and involves the assigning of a new quantum number

to all particles, P_R, defined as

$$P_R = (-1)^{3(B-L)+2s}, \tag{2.25}$$

where B is the Baryon number, L is the Lepton number and s the spin of the particle in question. The assignment of this value is useful because, defined in this way, $P_R = +1$ for all Standard Model particles and $P_R = -1$ for all Supersymmetric particles. Conservation of R-parity states that in any interaction the total value of P_R must be conserved, there are three primary consequences of this, namely

- In particle collisions, such as in the LHC, *s*particles can only be produced in pairs, one *s*particle and one anti-*s*particle at a time, identical to constraints on particle/anti-particle production.
- Every *s*particle heavier than the 'Lightest Supersymmetric Particle' (LSP) must decay to a state involving an odd number of lighter *s*particles (usually just one) and, eventually, via one or more steps, decay to the LSP's (usually just one LSP) alone.
- Finally a specific importance is placed on the LSP, as in order to preserve this parity, this lightest of the *s*particles must be stable.

One further result of this third consequence is that, if the LSP is electrically and colour-charge neutral and hence interacts only via the weak force, then it will not be observable in collider detectors and will escape in much the same way as a Standard Model neutrino, albeit a heavier one. Therefore if *s*particles are produced in the LHC the LSP will cause a significant momentum imbalance in events, which the search described in this work directly relies upon to identify SUSY candidate events.

Supersymmetric models that violate R-parity are also possible, but only one particular model which conserves R-parity is considered here.

2.4 Decays of SUSY Particles and their Experimental Signatures

Every supersymmetric particle produced in the LHC will be unstable and subsequently decay to an array of other particles, with the one exception in the R-parity conserving scenario considered in this thesis being the LSP, which will be stable. For this reason the search for any of these particles, instead of looking directly for the original particle itself, consists of looking for its decay products and determining the nature of the particle that produced them. The stable LSP would be expected to escape the detector region undetected if it interacts with ordinary matter only very weakly and therefore manifests itself in events as relatively large amounts of missing transverse energy ($E_{\mathrm{T}}^{\mathrm{miss}}$).

2.4.1 Squarks and Gluinos

If the supersymmetric particles predicted by the theory are present at the TeV scale, then the production of *s*quarks and gluinos will be one of the most promising channels for the discovery of supersymmetry at the LHC. This is due to the fact that, as the super-partners of quarks and gluons, these particles will interact via the strong force and as a proton-proton collider the LHC will produce them at a significantly higher rate than any other SUSY particles.

Figure 2.7 shows a schematic of a gluino produced in the initial interaction, which then subsequently decays to the lightest supersymmetric particle (assumed to be the lightest neutralino here and labelled 'χ_1^0') through a sequence of intermediate decays into lighter and lighter *s*particles. Typically these gluinos decay to *s*quarks, charginos ($\chi_i^{\pm}$) and neutralinos (χ_i^0), where $i = 1, 2, 3, 4$ and denotes the

mass order of the gauginos, 1 being the lightest. In order to preserve R-parity, each of these decays results in one further *s*particle and an ordinary Standard Model particle.

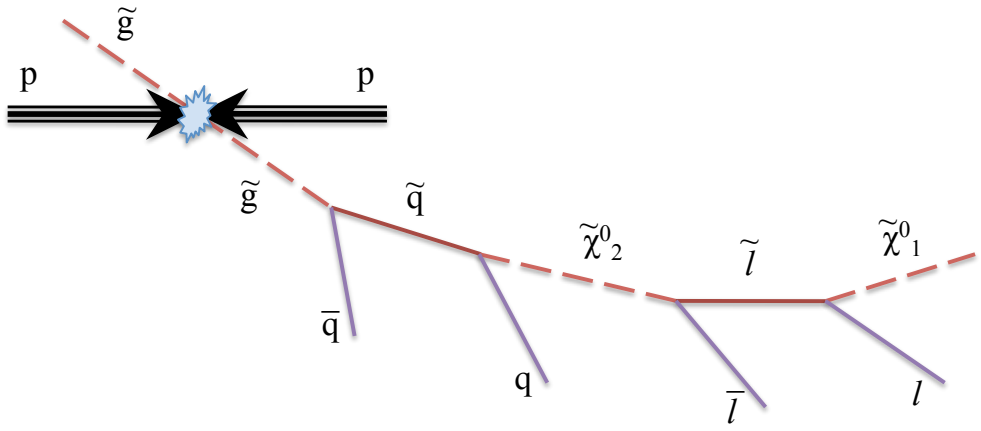

Figure 2.7: The decay chain of a gluino that eventually decays to the lightest supersymmetric particle producing multiple subsidiary quarks and leptons.

In the case where the gluino decays into a *s*quark and ordinary quark at least once in this process, the resultant jets produced by those quarks (depicted in the figure as the prongs labelled 'q') will be present in the final state. One of the *s*particles in the sequence of decays may decay to a supersymmetric lepton and an ordinary Standard Model lepton (represented in the figure as the prongs labelled 'l'), in this case the lepton produced will be present in the final state. In this event topology therefore, there would be expected to be the lightest super symmetric particle accompanied by any number of jets and leptons, in the final state observed in the detector.

Third Generation Squark Production

In the context of the MSSM form of supersymmetry the production of specifically the third generation *s*quarks could be favoured in these decay processes, depending on their relative masses in comparison to the other generations. This is

because the mixing effect of the chiral left- and right-handed states ($\widetilde{q}_L$ *and* $\widetilde{q}_R$) of the *s*quarks is proportional to their corresponding Standard Model quark masses. Due to the fact that the top and bottom quark masses are so much greater than the other quarks, this effect yields lighter masses for the *s*top and *s*bottom and hence, with *relatively* large associated cross-sections, they would be created more often from the collisions. This therefore motivates an attempt to look for supersymmetry by specifically searching for these more readily reproducible third generation *s*quarks.

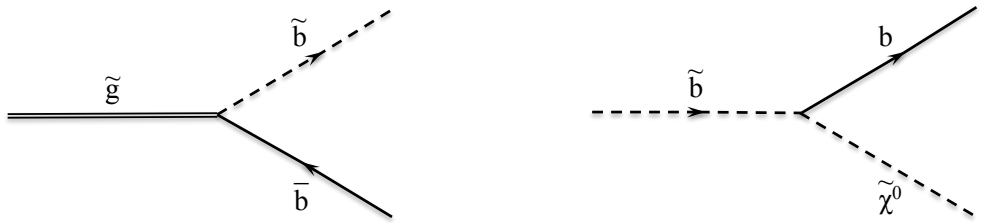

Figure 2.8: A gluino decaying to a *s*bottom and an anti-bottom quark (left) and the *s*bottom subsequently decaying into a bottom quark and the LSP (right).

2.4.2 Gluino Mediated Sbottom Production

The specific supersymmetric process that is the prime focus of this analysis is the gluino mediated *s*bottom production process. This process, illustrated in two stages in figure 2.8, originates from the production of a gluino/anti-gluino pair in the initial proton interaction as outlined in the previous section. The gluino then decays into a *s*bottom and an anti-bottom quark, the *s*bottom subsequently decays into a bottom quark and the LSP. The bottom quarks produce *b*-jets and as stated above the LSP, taken in this analysis to be the neutralino (χ_1^0), contributes to a large missing transverse energy.

Only processes where no leptons are produced at any point in the decay chain are considered in this analysis. This includes leptons originating either

from Standard Model top quark decays, themselves the decay products of *s*top particles, or from SUSY particles pair producing *s*lepton-lepton pairs as shown in figure 2.8 above. Therefore the event topology for this process includes the observation in the final state of multiple jets, with at least one of these being a *b*-jet, in addition to missing transverse energy. No leptons are present, where 'lepton' here refers specifically to either an electron or a muon.

Chapter 3

The LHC and the ATLAS Detector

3.1 The LHC accelerator

The Large Hadron Collider (LHC) is a particle accelerator at the European Organisation for Nuclear Research (CERN) near Geneva, Switzerland [1]. The LHC is the most recent of many accelerators built at CERN, all of them originally designed to probe the ever increasing energy frontier. It is designed to accelerate, and subsequently collide at fixed points on the ring, two proton beams and consists of two anti-parallel beamlines curved to form a ring with a circumference of 27km. The beamline is housed in an underground tunnel, approximately 100m below the surface, that formerly accommodated the Large Electron-Positron Collider (LEP), which was dismantled in order to make way for the construction of the LHC.

The main LHC ring is connected to a network of smaller accelerating structures, which now serve as the feeder accelerators for the LHC [17]. This network, illustrated in figure 3.1, includes the initial Linear Accelerators (LINACS), the Proton Synchrotron Booster (PSB), the Proton Synchrotron (PS) and the Super Proton Synchrotron (SPS). The network also includes the Anti-Proton Decelera-

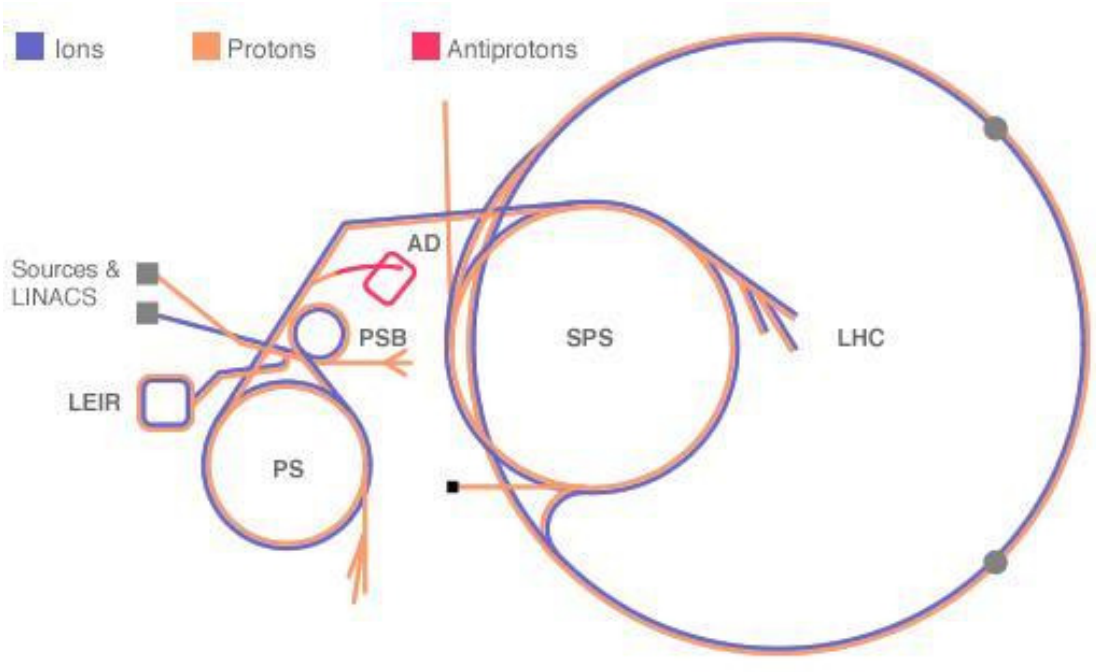

Figure 3.1: The LHC accelerator network [17].

tor (AD) and the Low Energy Ion Ring (LEIR), which are not used in the delivery of protons to the LHC. Emanating from a proton source the beams pass through each of the pre-LHC accelerators one-by-one, being accelerated to higher energies in each, reaching 50 MeV in the LINACS, 1.4 GeV in the PSB, 26 GeV in the PS and when, having reached an energy of 450 GeV in the SPS, they are injected into the main LHC ring. In the LHC each beam will eventually be accelerated up to 7 TeV producing, at collision, a centre of mass energy $\sqrt{s} = 14$ TeV. The centre of mass energy produced during 2011 data taking, and hence seen in the data used in this thesis, is $\sqrt{s} = 7$ TeV, 3.5 TeV per beam[1], a significant improvement on the $\sqrt{s} = 1.96$ TeV of the Tevatron, previously the world's most powerful accelerator [18].

[1]In 2012 the centre of mass energy rises to $\sqrt{s} = 4$ TeV per beam.

3.1.1 The LHC detectors

There are four experimental caverns placed at set points around the LHC tunnel, at each of these four locations the two beams are brought together to induce collisions between the opposing protons. These locations are known as the interaction points and at every one of these interaction points is a detector designed to observe the resultant particles generated by the collisions that occur within them. Two of the detectors at the LHC are designed for very specific purposes. One, LHCb, looks for new physics in interactions involving b-quarks and, in addition, investigates specifically CP violation in these interactions. The other, ALICE, studies a state of matter known as the quark-gluon plasma, produced via the collisions of Lead ions when they replace the protons ordinarily accelerated in the beamlines. The other two detectors, diametrically opposite each other on the LHC ring, are ATLAS and CMS, both general purpose detectors designed to allow for as wide ranging a programme of research as possible.

A proton beam in the LHC is not one continuous stream of particles, but rather separated into many equally spaced bunches of particles. These bunches are separated so that the products from collisions that occur in one bunch can be more easily distinguished by the detectors without interference from the products of collisions in the neighbouring bunches. The bunches are focused into a very small cross-sectional area by three quadrupole magnets in the region immediately before the interaction point to maximise the interaction point luminosity and hence the event rate in the detectors. The luminosity is defined as

$$\mathcal{L} = f\frac{n\ N^2}{A}. \tag{3.1}$$

Here f is the bunch crossing frequency, N is the number of particles in a bunch (N^2 for two identical bunches), n is the total number of bunches in the ring and A is the cross-sectional area of the beam. Therefore it is clear that a

smaller area presented by the beam will result in a higher luminosity and, as the event rate for any given process is given by

$$R = \sigma \mathcal{L}, \tag{3.2}$$

then for a set luminosity the total number of events seen by the detectors in any given period of time depends solely on σ, the 'cross-section' for that particular process. As the energies in the LHC mean these protons travel effectively at the speed of light around the ring, the crossing frequency is dependent only on the total number of bunches. In the LHC the number of bunches in the beamline at collision is 2808 and each bunch contains 1.15×10^{11} protons, this corresponds to a luminosity at ATLAS and CMS of $\mathcal{L} = 10^{34}$ cm^{-2}s^{-1} [19].

3.2 The ATLAS detector

The ATLAS detector[2], measuring 45 m in length, 25 m in diameter and weighing 7000 tonnes, is a general purpose detector designed to have a highly hermetic coverage of the interaction point it surrounds [2]. This means its sensitive regions intercept, over a very wide range of trajectories, any particles emanating from near the interaction point at its centre. Physically it consists of a series of concentric cylinders built around this interaction point, flanked by a series of end-caps of increasing radius.

The detector can be separated into three primary sections, the inner detector, the calorimeters and the muon chambers. Two of these three regions are immersed in magnetic fields provided by two different magnet systems. These are the solenoid field covering the inner detector and the toroid field covering the outer muon chambers.

[2]ATLAS = A Toroidal LHC ApparatuS

The ATLAS Co-ordinate System

The co-ordinate system used to describe the detector region is specifically defined to match the detector's physical geometry, with the z-axis defined along the beamline axis, the x-axis towards the centre of the LHC ring and the y-axis directly upwards [20]. The azimuthal angle ϕ, defined with respect to these axes, measures the radial direction in a plane cut through the detector perpendicular to the beam-axis. The quantity known as pseudo-rapidity, η, is a measure of the degree of inclination in a plane parallel to the beam-axis. The pseudo-rapidity is a useful quantity as particles from the interaction point are produced roughly equally across the range of values it takes on, it is an expression of the polar angle θ defined as

$$\eta = -\ln\left(\tan\frac{\theta}{2}\right) \tag{3.3}$$

The extent of coverage provided by the different detector components across the full pseudo-rapidity range is given in table 3.1. The result of this coverage is that only trajectories deviating from the beam-axis by a very small amount, typically less than 1°, escape the detector as this is too close to the high energy main beam for sensitive detector material to be placed. Being cylindrical in nature all of the ATLAS components have a full 2π azimuthal ϕ coverage.

Any particle trajectory emanating from a particular point on the z-axis is uniquely defined in space by these two properties η and ϕ and quantitatively the angular separation ΔR between two separate particle trajectories is defined as

$$\Delta R = \sqrt{(\Delta\eta)^2 + (\Delta\phi)^2}. \tag{3.4}$$

Two quantities that are often used for describing the properties and behaviour of particles in the detector region are their transverse energy E_{T} and transverse

Detector Component	$\lvert\eta\rvert$ coverage
Inner Detector	2.5
Electromagnetic Calorimeter	3.2
Hadronic Calorimeter	4.9
Muon Spectrometer	2.7

Table 3.1: The pseudo-rapidity coverage provided by the different ATLAS detector components.

momentum p_{T}. These quantities are defined in the $x - y$ plane in the above system of axes and are related to the momentum $\mathbf{p}$ and energy $\mathbf{E}$ possessed by the given particle(s) by

$$p_{\mathrm{T}} = \mathbf{p} \sin\theta, \tag{3.5}$$

$$E_{\mathrm{T}} = \mathbf{E} \sin\theta. \tag{3.6}$$

Each of these quantities will be used throughout this thesis in the identification and subsequent study of the particles that are observed.

Detector Composition

Each of the three main parts of the detector introduced above performs a different task and every one is vital to the overall ability of the detector to locate and identify particles emanating from a collision at its centre. The signatures detected by all of these sub-systems are then used together to reconstruct the interactions that took place in the detector and determine the types of particles subsequently produced, along with their trajectories and momenta. This information then allows the detailed study of these particles and their properties.

The ATLAS detector and the locations of its sub-systems are shown in fig-

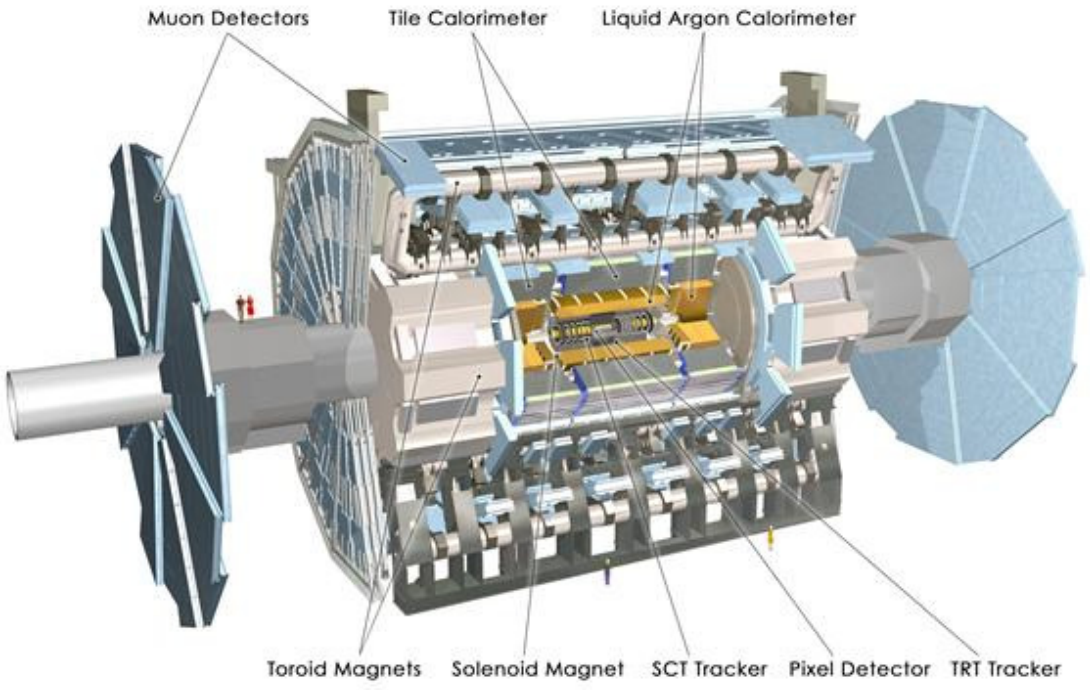

Figure 3.2: The ATLAS Detector

ure 3.2 and each of these individual detector sub-systems is discussed here, in order from the closest to the interaction point outwards.

3.2.1 The Inner Detector

The inner detector lies at the heart of ATLAS and encloses the immediate vicinity around the interaction point [21]. Starting at a radial distance of 50.5 mm from the central axis of the beam it extends out radially to 1062 mm and is 6.2 m in length. It is designed to record the tracks of charged particles as they traverse through its sensitive material.

The full inner detector consists of three separate sub-components, the Pixel detector which lies closest to the beamline, followed by the Semiconductor Tracker (SCT) and lastly the Transition Radiation Tracker (TRT). The cross-sectional layout of the inner detector, showing the regions covered by each of these sub-detectors, can be seen in figure 3.3. All of these sub-detectors are sensitive to the

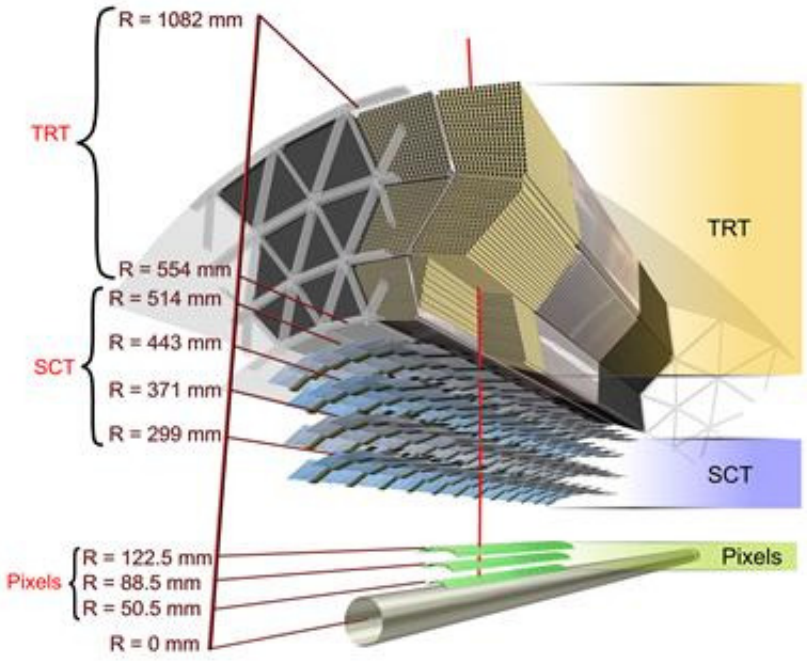

Figure 3.3: A cross-sectional view showing the barrel region components of the inner detector and their radial positions relative to the beam [22].

tracks left by charged particles traversing through them and each one employs a different method of detection.

The Pixel Detector

Lying between 50.5mm and 122.5mm from the beam-axis, the Pixel Detector is the closest component to the ATLAS interaction point [23]. It is formed by a total of 1744 individual silicon pixel sensor modules distributed over three cylindrical layers in the barrel region and six end-caps covering a total surface area of 2.1m^2, in the range up to $|\eta| < 2.5$. Each of these pixel sensor modules is comprised of 46,080 identical pixels measuring 50 μm by 400 μm in size.

The intrinsic resolution provided by these pixels is 10 μm (R-ϕ) and 115 μm (z) in the barrel region and 10 μm (R-ϕ) and 115 μm (R) in the end-caps.

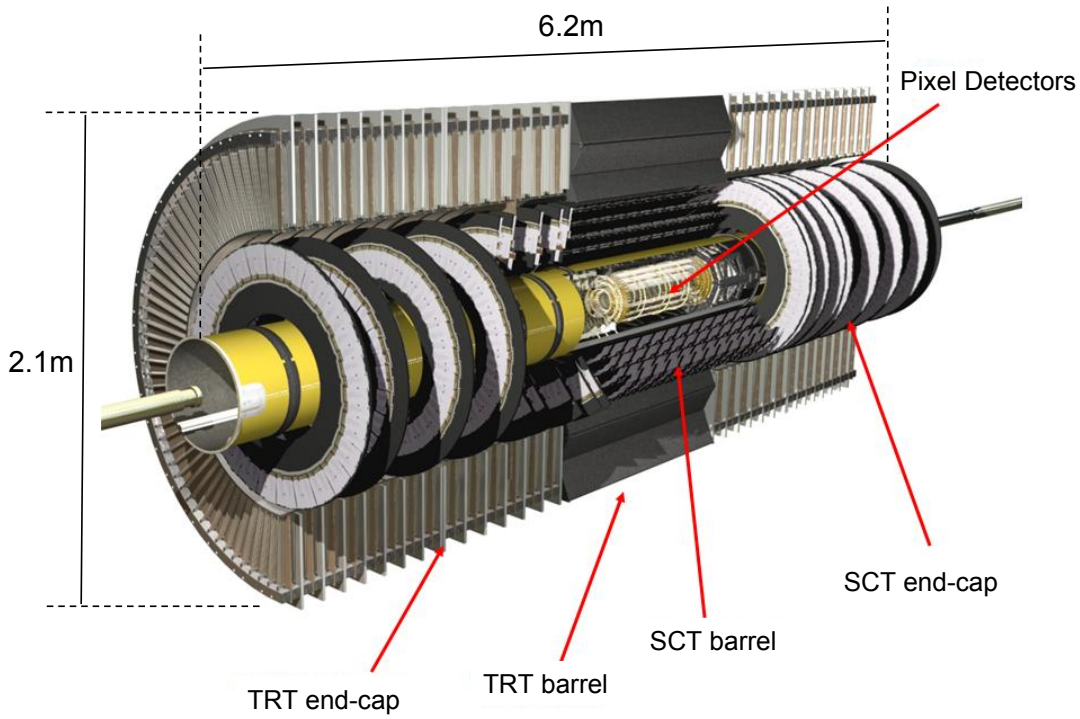

Figure 3.4: A view of the inner detector showing the different sub-components and the relative positions of their barrel and end-cap segments [22].

The Semiconductor Tracker

The Semiconductor Tracker (SCT) consists of a total of 4088 individual silicon micro-strip detectors, which are arranged (figure 3.4) into four concentric layers in the barrel and nine end-cap discs on either side [2]. This provides a minimum of four separate positional measurements on tracks passing through the detector region.

Each silicon detector module in the barrel is identical and measures 128 mm in length, with a strip pitch of 80 μm. The strips on either side of a given module are rotated by ± 20 mrad with respect to one another, with one set of strips aligned parallel to the beamline direction. This physical orientation allows measurements in the R-ϕ plane and the offset allows measurements in the z-direction. An illustration of a barrel module, showing the two sided sensitive silicon sensors with this relative offset, can be seen in figure 3.5. The end-cap

modules vary in size, with modules on the outer discs (furthest from the barrel), measuring 121 mm in length, on the middle discs 118 mm and on the inner discs 61 mm. The set of strips on these modules are aligned radially around the end-cap in order to make measurements in the R co-ordinate.

Together these SCT modules have a total surface area of 61.1 m^2 of sensitive silicon, providing an almost hermetic coverage extending up to $|\eta| < 2.5$. The intrinsic resolution achieved by these modules are, for the barrel modules 17 μm (R-ϕ) and 580 μm (z) and for the end-cap modules 17 μm (R-ϕ) and 580 μm (R).

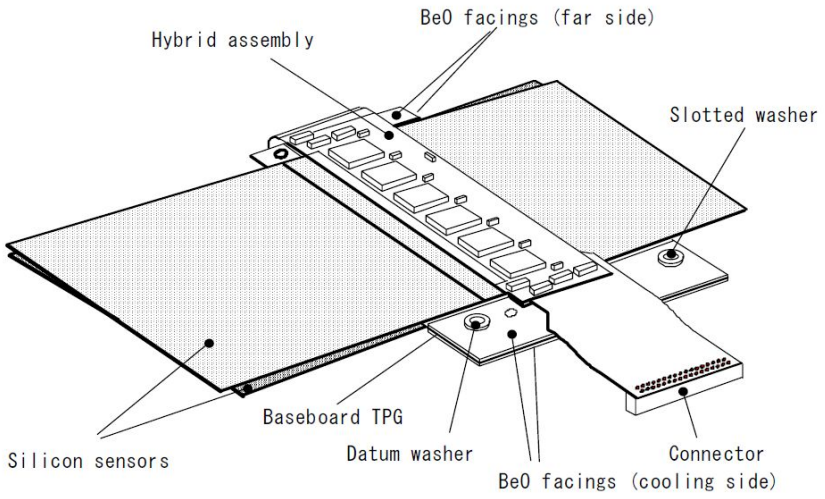

Figure 3.5: Schematic of an individual SCT barrel module with the two silicon sensors offset by a total of 40 mrad (±20 mrad with respect to the module axis).

The Transition Radiation Tracker

The Transition Radiation Tracker is a straw based tracking detector that extends up to a coverage of $|\eta| < 2.5$ [24]. It consists of 83 layers of straw drift tubes in the barrel region and 160 straw planes in the end-cap regions. The straw drift tubes are 4 mm in diameter and up to 144 cm in length, they each have a high voltage tungsten wire 31 μm in diameter, plated with gold 0.5 μm thick, running

through their centre. This wire operates as an anode and the surrounding tube surface, maintained at a potential difference of 1530 V, as a cathode and the straw tubes themselves are filled with a Xenon (70%), Carbon-dioxide (27%) and Oxygen (3%) gas mixture.

As a charged particle traverses through one of the straw tubes it ionises the particles in the gas, which in turn drift towards the central anode and produce a charge on the wire that can be detected. This method allows for ~ 36 measurements per track on average in the TRT region and the tracking resolution in R-ϕ is 130 μm per wire.

The straw tubes are embedded in a structure of 19 μm diameter polypropylene fibres, which serve as transition radiation material, this can induce the emission of a photon from a charged particle passing through this material into the straw tubes which helps in producing a stronger signal in the wires.

The Solenoid Magnet

The solenoid magnet is the first of the two separate magnet systems in ATLAS, it immerses the entire inner detector region in a 2 Tesla magnetic field to assist in the identification of the particles it detects. As an electrically charged particle moves in a curved trajectory when traveling through a magnetic field, it is possible to deduce its momentum by measuring this curvature and the sign of its charge from the curvature direction. The particles transverse momentum can be calculated by

$$p = Bqr, \tag{3.7}$$

where B is the magnetic field strength given above, q is the charge possessed by the particle traversing the region and r is the radius of curvature observed. To good approximation, only particles with $|q| = 1$ successfully traverse the inner

detector region[3], therefore with the absolute value of q assumed, the momentum can be obtained from the measurement of the radius observed.

3.2.2 The Calorimeters

Outside of the inner detector lie the calorimeters. ATLAS has two separate calorimeter systems, whose layout relative to the inner detector region is shown in figure 3.6, these calorimeters are used for measuring the energy of *most* of the particles emanating from the interaction region [25]. They are designed so that a particle traversing through them will lose all of its initial energy through its interaction with the material in the calorimeter, the total amount deposited can then be calculated from the signals recorded in the sensitive material.

The Electromagnetic Calorimeter

The innermost of these two systems is the Electromagnetic or 'Liquid Argon' (LAr) calorimeter [2, 25], primarily used for inducing electromagnetic showers from incident electrons or photons and covers a region up to $|\eta| < 3.2$. It is constructed using an accordion geometry, as can be seen on the profile view in figure 3.7. This particular geometry is employed so as to naturally leave no cracks in the calorimeters coverage in ϕ. In the barrel region these accordion waves are aligned axially around the beamline and run in the ϕ direction.

The LAr calorimeter consists of alternating layers of absorbing and sampling materials, with the former dissipating the energy of an incident particle and the latter providing for the detectable signal. The absorbing material uses lead plates as its energy absorbing material, bolstered with steel sheets 0.2 mm thick in order to provide mechanical strength. The lead plates have a thickness of 1.53 mm in the region $|\eta| < 0.8$ and 1.13 mm for $|\eta| > 0.8$, this decrease in

[3]The rest being either too short lived to make it to the tracking region in the first place or, for higher charged baryons produced in the collisions, much more likely to interact with the non-sensitive material before this point.

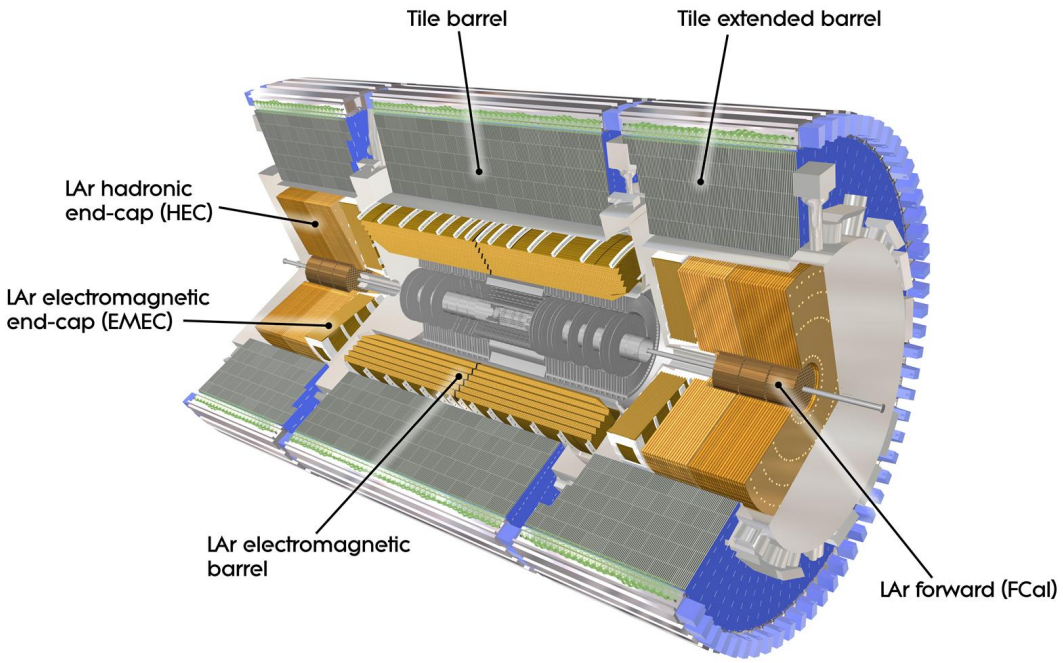

Figure 3.6: The ATLAS calorimeters, including the electromagnetic (LAr) and hadronic (Tile) calorimeters, barrel and end-cap regions. The inner detector can be seen in the centre in grey.

thickness minimises the decrease of the sampling fraction in the higher $|\eta|$ region. The sampling substance is liquid argon, giving the detector its name, providing an energy resolution of approximately $10\%/\sqrt{E}$ GeV$^{1/2}$.

The Hadronic Calorimeter

The outermost of the two calorimeter systems is the Hadronic 'Tile' calorimeter [2, 25], which is designed to sample hadronic processes and covers the region up to $|\eta| < 3.2$. There is also mixed electromagnetic and hadronic detection in the forward calorimeters extending over a range of $3.1 < |\eta| < 4.9$. The tile calorimeter uses a method similar to the LAr calorimeter in that it employs alternating layers of absorbing and sampling material. It, however, uses steel as the absorber and scintillator tiles as the active sampling medium. These scintillator

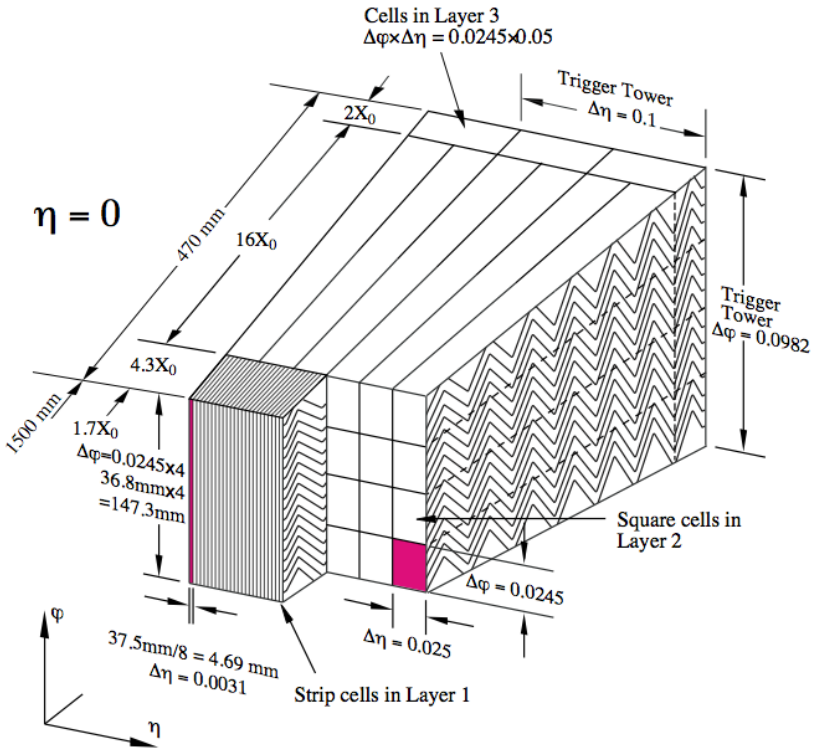

Figure 3.7: An electromagnetic calorimeter barrel module showing the geometrical layout of the absorbing lead plates and the resolution in ϕ and η.

tiles provide an energy resolution of approximately $50\%/\sqrt{E}$ GeV$^{1/2}$.

Although most particles, with a lifetime long enough to reach the calorimeters, generally have their energies completely absorbed, there is one notable exception. These are the muons, for which a further sub-detector external to the calorimeters exists in order to assist in the identification of these particles.

3.2.3 The Muon Spectrometer

As muons have a lifetime of 2.2×10^{-6} seconds [6], they therefore don't decay within the confines of the detector and, given that they are not absorbed by any of the material already in place in the inner detector region or the calorimeters, specially constructed muon chambers are placed in the region external to the rest of the detector in order to positively identify them [26]. As, although the mo-

mentum carried by these particles can be accurately determined with the charged tracks they leave in the inner detector, the matching of one of these tracks with a corresponding signature detected in the muon chambers identifies that particle as a muon.

Spanning from approximately 5 m out to a radius of 11 m this muon spectrometer system defines the full dimensions of the detector. This muon system has a coverage of $|\eta| < 2.7$ and is designed to provide the ability to trigger on muons that are present in events in the range of $|\eta| < 2.4$. The detector material is arranged in separate layers covering a total area of 12,000 m^2 and has 1 million readout channels, the specific role of the toroid magnet system and each of these layers is described in the following sections.

The Toroid Magnet

A system of eight superconducting toroid magnets in the central barrel and eight more in each end-cap provide magnetic bending power in the region covered by the muon spectrometer [27]. The barrel section is 25.3 m in length and extends from a radius 4.7 m to the outer edge of the muon spectrometer. The field strength is 0.5 T in the barrel and 1 T in each of the end-caps. The resultant magnetic field is not as uniform as the field in the inner regions, but this is satisfactory because the resolution required in the muon chambers is lower than that required in the inner detector systems.

This additional magnetic field allows a further determination of the momentum of a given muon, using the same principle employed in the inner detector with the solenoid field described above. This second track-momentum measurement can then be used to assist in the process of matching signals in the muon spectrometer with tracks observed in the inner detector.

Monitored Drift Tubes

The Monitored Drift Tubes (MDT) allow for the precision measurements of tracks in the muon spectrometer in the direction parallel to the magnetic field. The aluminium drift tubes themselves are 29.97 mm in diameter and filled with a gas mixture of 93% Argon and 7% Carbon Dioxide at a pressure of 3 bar. They have a 50 μm diameter tungsten-rhenium alloy wire carrying a voltage of 3080 V running through their centres, with an accuracy of concentricity through the centre of the tube of $\sigma < 10$ μm.

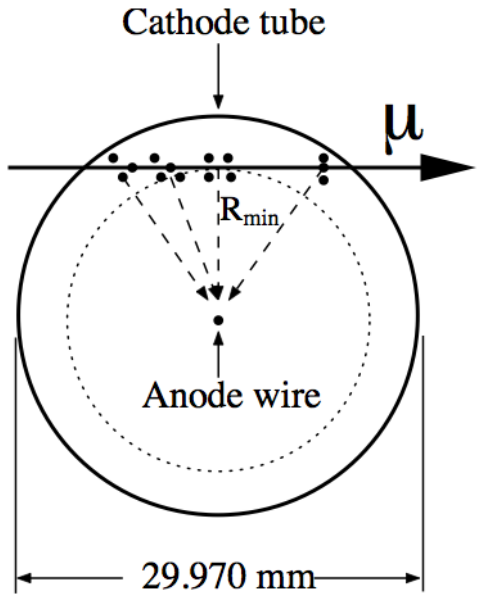

Figure 3.8: A cross-sectional view of a monitored drift tube.

As any charged particle traverses through the tube the gas mixture is ionised and the resulting ions are, as illustrated in figure 3.8, induced to drift towards the central wire by the potential difference between it and the surrounding tube causing a cascade of ionisation which is detected by the wire as electric current. These tubes are arranged in layers with central wires running parallel to the direction of the magnetic field and the measurement of the muon paths is made from the combination of drift times observed in multiple tubes. Each individual wire tube

provides a spatial resolution of approximately 80 μm in this measurement and they are used to provide a coverage up to $|\eta| < 2.7$.

Cathode Strip Chambers

On the inner side of the two end-caps, at an $|\eta| > 2.7$, where the background activity is highest the MDTs are replaced with Cathode Strip Chambers (CSC). The CSCs are multi-wire proportional chambers which perform in essentially the same way as the MDTs, although they can endure the much higher incident flux rates expected in these regions of approximately 200 Hz.cm^{-2}.

Resistive Plate Chambers

The Resistive Plate Chambers (RPC) form the muon trigger system in the barrel region and consist of three concentric layers around the beamline. The outer RPC layer provide a trigger decision to select tracks in the range 9 to 35 GeV, the high p_{T} muon trigger, and the inner two RPC layers provide the low p_{T} trigger in the range between 6 and 9 GeV.

Thin Gap Chambers

The Thin Gap Chambers (TGP) detectors provide muon trigger information in the end-caps in addition to the determination of the second ϕ co-ordinate in order to compliment the measurement of the MDT chamber described above in the radial direction.

Chapter 4

ATLAS Data Taking

The ATLAS detector, as described in the previous chapter, records the individual events that result from the collisions between protons at the interaction point at its centre. These events and the information regarding their content and properties are stored in preparation for analysis and, as a whole, are referred to as the 'data' collected by the detector.

Here the data taking procedure along with the set of data used in this analysis is outlined. Additionally, the process through which the quality level for analysis is determined for different sub-sets of the data is described. A focus is given to the description of this process in the SCT sub-detector and in particular to a method used to assist in the final decision on the data quality in the SCT is discussed.

4.1 Data Collection in 2011

The data used in this analysis were recorded by the ATLAS detector during the LHC's operation in 2011, figure 4.1 shows the rate of accumulation of this data over time in terms of the total integrated luminosity (see section 3.1.1). The centre of mass energy ($\sqrt{s}$) of the collisions occurring throughout this data taking period was $\sqrt{s} = 7$ TeV.

The full dataset recorded by ATLAS in the year 2010 is negligible in comparison and consists of less than 2% of the total data contained in the 2011 dataset. This dataset was also collected utilising a different set of trigger requirements than those the 2011 dataset considered, so for this combination of reasons it was considered not worthwhile to include it in addition here.

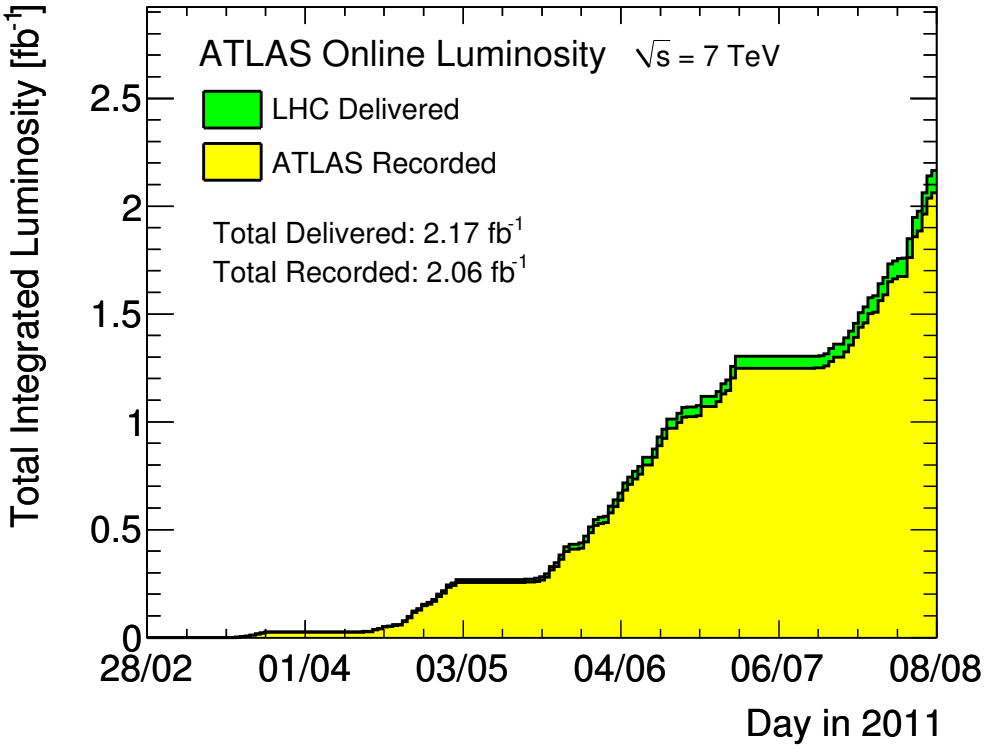

Figure 4.1: The total integrated luminosity recorded over time up to 2.05 fb^{-1}, the delivered luminosity is shown in green and the proportion of this successfully recorded by ATLAS in yellow

A total integrated luminosity of 2.05 fb^{-1} of the 2011 data is used in this analysis, after the application of the standard data quality requirements, as prescribed by the ATLAS collaboration's SUSY working group. The beam and detector parameters changed over the course of this data taking, so the total dataset is split up into separate data periods where these run conditions were stable. These dif-

ferences between run conditions are not detrimental for this analysis and can be accounted for, so for this reason all of the data periods comprising this portion of the data recorded during 2011 are combined and utilised here and each period provides a contribution to the total integrated luminosity given above.

4.2 Data Quality

One essential part of the data taking process at ATLAS is to assess the *quality* of the data that is recorded. This data quality is dependent upon the status and condition of the detector components themselves whilst data is being taken. The quality of a given set of data is something that must be taken into account when a decision is taken on which data to include in any physics analysis and which should be disregarded due to non-optimal running conditions or hardware faults present in different parts of the detector at the time the data in question was recorded.

ATLAS operates by taking data in the form of runs, where one run is one continuous, uninterrupted, period of data taking. These runs involve collisions from the same set of proton bunches that are injected into the LHC before the start of each run and orbit continuously whilst a given run is ongoing. If for any reason the beams are lost, or must be discarded, in the accelerator then the ATLAS run is also aborted. Each of the data runs is split up into segments, referred to as luminosity blocks, where each luminosity block corresponds to approximately one minute of data taking within its parent run, so on average the longer a run the more luminosity blocks it will contain.

It is on the level of these luminosity blocks that the quality of the data is assessed and so the data recorded during one part of a run may be considered of bad quality, but the data recorded in another part of that same run could be ok for use in physics analysis.

4.2.1 The Data Quality Monitoring Framework

The Data Quality Monitoring Framework (DQMF) is the primary software system in place to monitor the physics performance of the ATLAS detector in the context of data quality [28]. It is this system that is used to determine the quality of the data recorded in each of the luminosity blocks in a given run. The DQMF monitoring system provides automatic checks which follow a predefined algorithm and compares relevant quantities against predetermined threshold levels.

This process is carried out twice, both 'online', which refers to the period during which a run is taking place, and 'offline' which refers generally to the period in the 24 hours after it has finished.

The Detector Control System

The Detector Control System (DCS), described in full detail in [29], is an automated system which continually supervises the condition of all of the elements within the detector and monitors parameters such as temperature and component power supply voltage levels. These quantities, if non-optimal, can affect the performance of the different parts of the detector during data taking to the detriment of data quality.

The ATLAS Shifters

In addition to the initial automated checks described above, checks are also made manually by shifters. Two separate shifters are on duty for every ATLAS run and so, as with the DQMF, these checks happen at both the online and offline stages, with the offline shifter providing the last data quality decision before the final combined status is set.

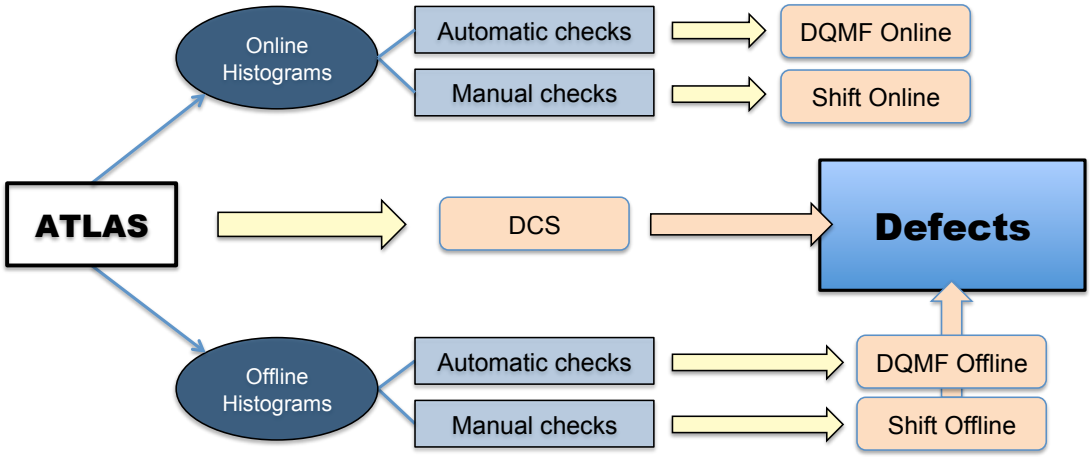

Figure 4.2: A schematic summarising the ATLAS Data Quality Monitoring system with the defects information being used to construct good run lists.

ATLAS DQMF Overview

The different aspects of the ATLAS Data Quality Monitoring system, their relationship to each other and how they are combined are shown schematically in figure 4.2. Two separate sets of histograms are produced for every run recorded, the online and offline histograms. These histograms describe quantities relevant to the data quality performance of separate parts of the ATLAS detector. These two sets of histograms are checked both automatically and manually and the information from the DCS, DQMF offline and shift offline checks are used to inform the defects status, which is the system used to make the final data quality decision and is outlined in the following section.

4.2.2 The Defects Database

The defects database is a system of recording individual, well defined, problems affecting the data quality in the detector [30]. These problems fall into one of four separate categories depending on whether they are applicable to the entire run in question or just a specific set of luminosity blocks and whether they are

tolerable or *intolerable* in nature.

There is a bit set by the shifter corresponding to each one of these individual problems to indicate whether that particular defect was present or not in the whole or part of a given run. This final set of information is collated and a pre-defined logic system is applied to the combination of defects observed in order to decide the quality of each luminosity block of data. Once obtained, this information is used to construct what are known as 'good run lists', which can then subsequently be used in physics analyses.

4.2.3 Good Run Lists

A 'Good Run List' (GRL) is a list that is put together to specify all of the runs in a given time period that possess at least some luminosity blocks with a final status showing no intolerable defects for the whole detector. This list includes the identifying run numbers themselves as well as the corresponding luminosity block numbers within each run that have been assigned a good data quality status. Therefore the runs, and specifically the luminosity blocks within these runs, that appear in a GRL are regarded as of satisfactory quality to be used in the analysis for which that list has been produced. There is the potential for multiple GRL's covering the same set of data, as some specific analyses require the use (and therefore the corresponding quality of) only some parts of the overall detector and so different luminosity block ranges may be acceptable to different analyses.

One specific Good Run List was used in the analysis carried out in this thesis, which was constructed in the manner outlined in the previous section. This list covers the whole data taking period defined in section 4.1 above and its use within the analysis will be described in chapter 7.

4.3 ATLAS Data Quality in the SCT

The sub-detectors, in general, monitor their own performance individually and assign the relevant defects database entries for that sub-detector themselves, as data is being taken. One important sub-detector which performs data quality monitoring in this way is the Semi-Conductor Tracker (SCT) and the procedure of determining the shifter offline data quality status in this sub-detector will be discussed in detail in this section.

The SCT assesses the data quality per luminosity block in each of its three main physical detector regions separately. These are the barrel and each of the two end-cap regions, which are described in section 3.2.1 in the previous chapter. This is done due to the fact that the conditions of these three regions are controlled separately and, due to the geometry of the detector the thresholds for making a decision may vary in the end-caps to the barrel region.

4.4 The SCT Data Quality WebTool

Work was undertaken for this thesis to produce and maintain a means of assisting the SCT data quality offline shifter in their responsibility of assessing the status of the SCT during each run and reporting any observed defects that may affect the quality of the data recorded by it in that run. As an offline part of the data quality procedure this assessment is typically carried out in the 24 hours after a given run has finished and assistance is in the form of providing and assessing all of the relevant information necessary for the shifter to judge and report on each status, in this time period. This was achieved by creating a software framework, accessible to the shifters, known as the SCT Data Quality WebTool [31, 32].

The main page of the Data Quality WebTool is shown in figure 4.3. This page shows an overview of the most recent data runs along with general information about those runs, including their duration and the number of events recorded. The status for one of these runs, as monitored by the DCS, of the different sub-

detector regions is displayed graphically in a colour coded form. The colour of each region corresponds to the DCS status of the majority of the luminosity blocks for that region in the selected run.

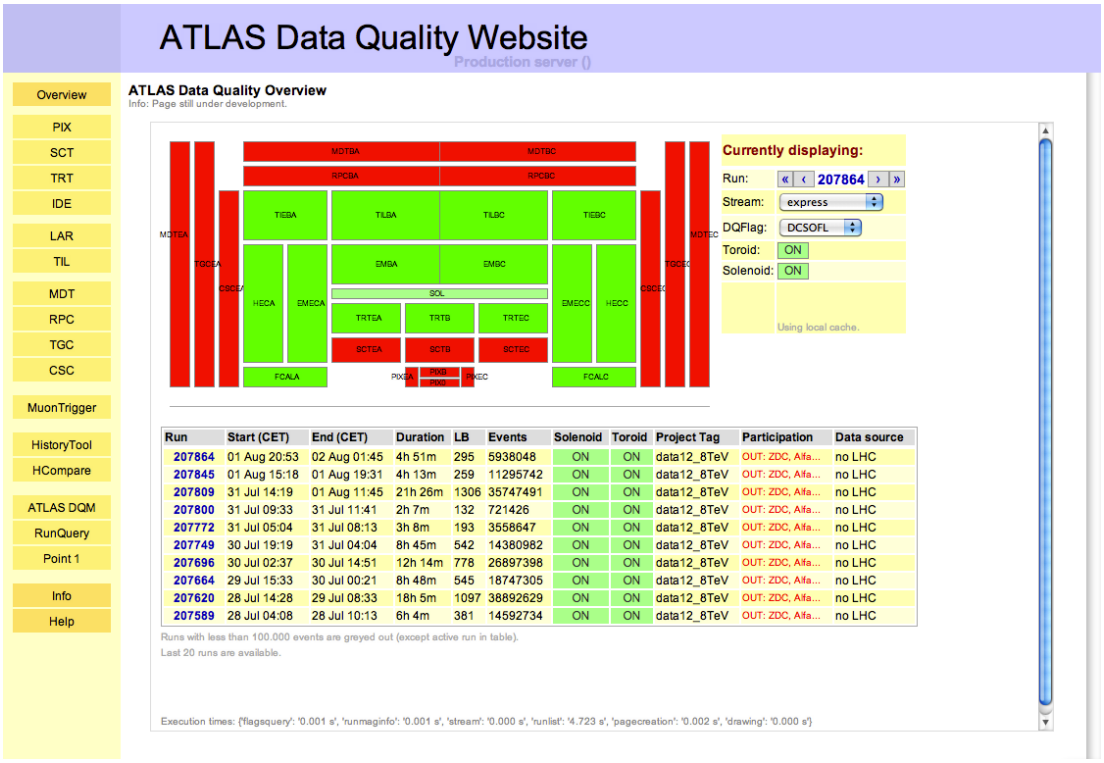

Figure 4.3: The ATLAS Data Quality Website Overview page.

The main page for the SCT Data Quality WebTool is shown in figure 4.4. This display is split into four main sections, each of which starting from the top of the page down shows more detailed information regarding the selected runs.

The main table at the top of the page shows general summarising information for each run. The middle table shows more detailed information on the performance of the SCT during each of the selected runs, it also has two pages which are displayed one at a time and toggled between when viewing all the available information. The pane in the bottom left, by default, alerts shifters to changes in the interface when they happen, but when one of the headings in the middle table

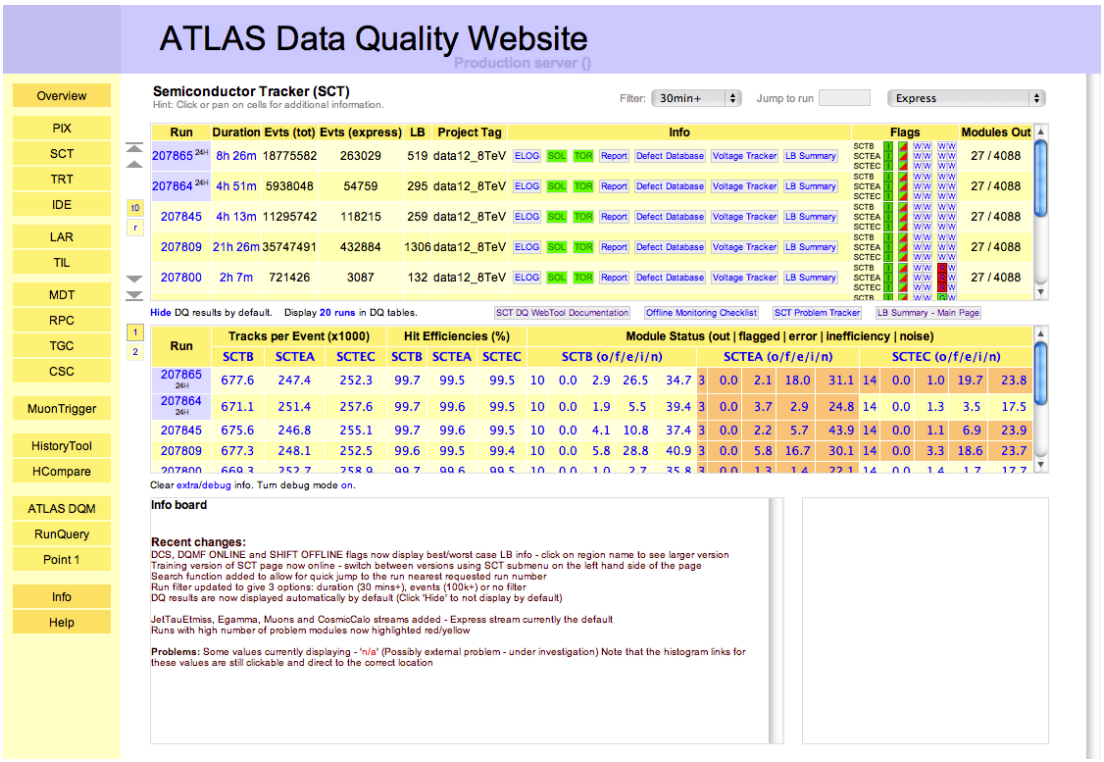

Figure 4.4: The SCT Data Quality WebTool main page.

is selected it shows a history plot for a comparison of all the values in that field for the most recent selected runs. Finally the pane in the bottom right, when one of the values in the middle table is selected, shows the corresponding histogram from which that value was derived. All of these individual parts of the WebTool are described in more detail below.

4.4.1 General Run Information

An example of the upper table displaying general run information is shown in figure 4.5. The information fields in this table are

- **Run Number -** The unique ATLAS identification number for each run. Highlighted in blue with '24H' appended for runs that finished within the last 24 hours.

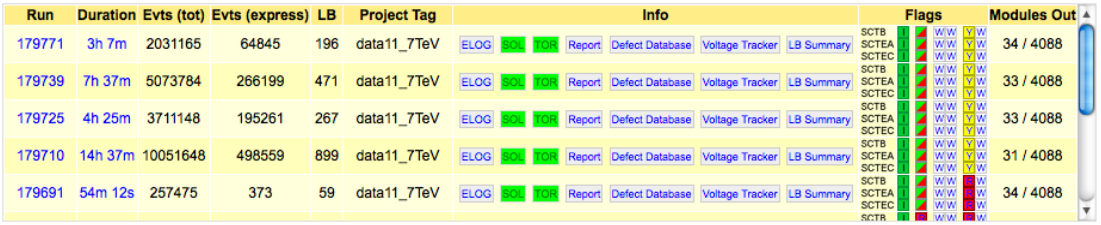

Figure 4.5: The run information table for SCT data quality.

- **Duration -** The time between run control start and stop.
- **Total Events -** The total number of events recorded during each run.
- **Selected Stream Events -** The number of events from the run present in the selected data stream[1].
- **Number of Luminosity Blocks -** The total number of luminosity blocks in each run.
- **Project Tag -** The nature of each run - whether the detector was collecting collision or cosmic data at the time and, if collision data, the period 'data11' and the centre of mass collision energy '7TeV'.
- **e-Log -** The SCT pages from the ATLAS e-Log which displays to shifters the relevant messages relating to SCT performance during the corresponding run.
- **Magnet Information -** The status of the Solenoid and Toroid magnets during each run. Green = ON, Red = OFF and Orange = In-transition during the run.
- **SCT Report -** Interface to generate the SCT report for each run, described in section 4.4.1.3.

[1]A particular data stream stores all the events in a run triggered by a given type of signature, one event may pass more than one set of criteria and be included in multiple data streams

- **Defect Database -** Connects to the interface for the Defects Database for each run to allow the setting of observed defects in the database.
- **Voltage Tracker -** Connects to external web display showing the SCT supply voltage as a function of time for each run.
- **LB Summary -** Interface for obtaining luminosity block level information about each run, described in section 4.4.5.
- **Summary Flags -** A graphical representation of the status for each run per SCT region.
- **Number of Modules Out -** The number of SCT modules out of the configuration during each run, out of a total of 4088 modules.

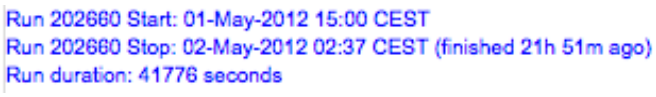

Figure 4.6: The time stamp information for an individual run.

The time stamp information for an individual run is shown in figure 4.6. This display gives confirmation of the date and time the given run was recorded, which is useful to compare the run against any known issues that have been highlighted as having been present in the SCT at that time.

4.4.1.1 Summary Flags

The summary flags shown in figure 4.7 are structured to display graphically five separate flags alongside an indicator showing whether that region of the SCT was in 'I' or out 'O' (disabled) for each run. These flags are purely colour coded summaries giving a general guide, for the run as a whole, as to the status for each

separate DQ check. In the case where there is not one uniform status assigned throughout a run and different luminosity blocks within the run have different statuses assigned to them, the summary flag shows both the best and worst cases present.

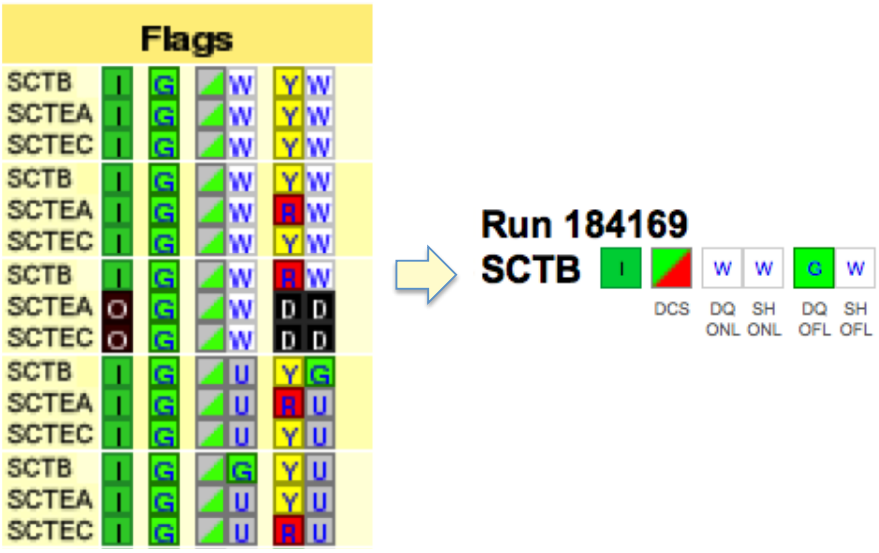

Figure 4.7: The summary flags for each of the three SCT regions per run (left) and the individual order for each of the five checks in one region (right).

For the DCS check the values are either green or red representing either a good or bad status. For the automated checks they represent a comparison against the set of predefined thresholds for each of the quantities described in section 4.4.3, where the values red and yellow show whether any of these thresholds were not surpassed or close to not being surpassed. Grey means there were not enough statistics to establish a value and white means no value is currently set. Black corresponds to a detector region being disabled during a particular run.

A view of the whole luminosity block range and the DCS status assigned per block is shown in figure 4.8, where in this case only the central 76% of the run was considered good quality data across all three SCT regions, representing a lower efficiency than the average observed in the SCT of $\sim$ 99.7% [33].

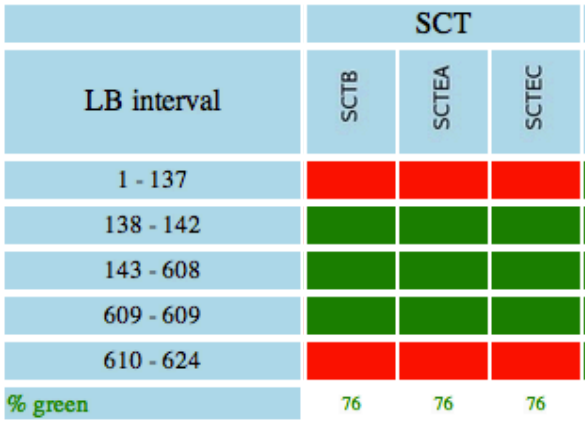

Figure 4.8: The data quality flag per luminosity block break down in the SCT for the shift offline data quality check.

4.4.1.2 Defects Database

This section of the tool, in the run information table shown in figure 4.5, is where the shifter can open the interface to make entries, on a run by run basis, of any observed defects seen during each run. The individual defects per SCT region that may be reported include

- A region showing less than 99.5% hit efficiency (section 4.4.3.2 below)
- A region not at nominal power supply levels
- Observing too few statistics in a region for a viable data quality decision
- Poor quality track reconstruction (section 4.4.3.3 below)
- Non-optimal timing (section 4.4.3.4 below)
- More than 40 SCT modules showing either serious errors or high noise occupancy levels (section 4.4.3.5)

It is this information, when combined with the other online and offline data quality checks that provides the input for producing the good run lists used for

physics analyses introduced in section 4.2.3.

4.4.1.3 SCT Report

When the shifter has completed the assessment of a run a report is generated by the tool summarising the key information regarding the SCT performance for that run, including the following information

- Run number and the date, time and run duration
- Total number of events recorded
- Status and electrical current through the Solenoid and Toroid Magnets
- DQMF status for each region
- Data quality parameters (discussed in section 4.4.3) relating to each region and the SCT as a whole
- The number of modules out of the configuration and the number of modules in the configuration showing problems during the run

A list of the individual SCT modules showing problems during the run is also given, including information on the serial number, coordinates of the location within the SCT and the type and severity of the error experienced.

This report is used to assist in the final data quality decision making and help monitor the behaviour of serially problematic SCT modules over time.

4.4.2 Detailed Run Information

The quantities shown in the detailed information tables are split over two pages for reasons of clarity. On the first page, illustrated in figure 4.9, are the tracks per event, hit efficiency rates and module status for each of the three SCT regions.

On the second page, illustrated in figure 4.10, are the tracks residual distributions, pull distributions and time bin information again for each of the three SCT regions. The details of these quantities and what they describe are outlined fully in section 4.4.3.

Run	Tracks per Event (x1000)			Hit Efficiencies (%)			Module Status (out | flagged | error | inefficiency | noise)													
	SCTB	SCTEA	SCTEC	SCTB	SCTEA	SCTEC	SCTB (o/f/e/i/n)					SCTEA (o/f/e/i/n)					SCTEC (o/f/e/i/n)			
202668 24H	675.8	248.3	252.5	99.7	99.6	99.6	10	0.0	3.8	0.0	1.2	4	0.0	0.7	0.0	2.6	14	0.0	2.0	0.0	2.6
202660 24H	676.9	249.1	251.5	97.5	97.1	96.8	10	0.0	2.8	0.3	0.5	4	0.0	0.0	0.0	1.3	14	0.0	1.4	0.0	2.4
202609	678.5	250.5	250.9	0.0	0.0	0.0	10	0.0	1.3	0.0	0.9	4	0.0	0.1	0.0	1.5	14	0.0	0.2	0.0	2.2
201970	0.0	0.0	0.0	0.0	0.0	0.0	10	0.0	0.0	0.0	0.0	4	0.0	0.0	0.0	0.0	14	0.0	0.0	0.0	0.0
201959	0.0	0.0	0.0	0.0	0.0	0.0	10	0.0	0.0	0.0	0.0	4	0.0	0.0	0.0	0.0	14	0.0	0.0	0.0	0.0

Run	Tracks per Event (x1000)			Hit Efficiencies (%)			Module Status (out | flagged | error | inefficiency | noise)													
	SCTB	SCTEA	SCTEC	SCTB	SCTEA	SCTEC	SCTB (o/f/e/i/n)					SCTEA (o/f/e/i/n)					SCTEC (o/f/e/i/n)			
179771	704.2	236.8	240.8	99.3	99.0	98.9	11	0.0	2.8	113.7	0.0	5	0.0	0.0	38.3	0.0	18	0.0	2.0	68.3	0.0
179739	707.2	237.3	239.8	99.3	99.1	99.0	10	0.0	3.0	104.8	0.0	5	0.0	1.7	37.3	0.0	18	0.0	2.6	65.4	0.0
179725	706.2	238.0	240.3	99.3	99.0	99.0	10	0.0	2.9	104.1	0.0	5	0.0	0.1	36.7	0.0	18	0.0	0.9	66.5	0.0
179710	704.2	239.1	240.2	99.4	99.0	99.0	10	0.0	3.5	99.8	0.0	4	0.0	0.5	37.2	0.0	17	0.0	3.2	67.8	0.0
179691	0.0	0.0	0.0	0.0	0.0	0.0	10	0.0	0.0	0.0	0.0	5	0.0	0.0	0.0	0.0	19	0.0	1.0	0.0	0.0

Figure 4.9: The first detailed run information table for quantities important to SCT data quality (above) and in the case of module status warnings (below).

As the tool is used by data quality shifters to assess the performance of the SCT during each run, it is useful to indicate graphically when one of the values on either of these tables falls below a predetermined threshold for data quality related performance. The thresholds are two-tiered, meaning that a warning level and critical level are defined and if either of these levels is surpassed for any value it is automatically displayed to the shifter in yellow (warning) or red (critical). This is shown in the lower image in figure 4.9.

The values displayed in the information table are, in some cases, modified for clarity, with the detail being saved for the corresponding histograms. The 'Tracks per Event' field is scaled by 1000 so a value of 675.8 in the barrel region equates to an average of 0.6785 tracks per event. The 'Module Status' field displays the average number of modules showing a given problem status over the course of a run. This means that the values are not limited to just being integers. The 'Track Residual' and 'Track Pull' fields show the mean and root mean squared

(RMS) values of the respective distributions. Finally, the 'Time Bin' field shows the ratio of *in time* hits to all recorded hits.

Run	Track Residuals (Mean/RMS) [µm]			Pulls (Mean/RMS)			TimeBin 010/XXX		
	SCTB	SCTEA	SCTEC	SCTB	SCTEA	SCTEC	SCTB	SCTEA	SCTEC
202668 24H	-0.0 / 47.8	0.0 / 48.3	-0.0 / 48.5	-0.0 / 1.05	0.0 / 1.03	-0.0 / 1.03	0.26753	0.23126	0.23422
202660 24H	-0.0 / 47.9	0.0 / 48.3	-0.0 / 48.6	-0.0 / 1.06	0.0 / 1.04	-0.0 / 1.04	0.23596	0.19855	0.19981
202609	-0.1 / 48.3	0.2 / 48.8	0.0 / 48.9	-0.0 / 1.06	0.0 / 1.03	-0.0 / 1.04	0.26712	0.23172	0.23589
201970	0.0 / 0.0	0.0 / 0.0	0.0 / 0.0	0.0 / 0.0	0.0 / 0.0	0.0 / 0.0	N/A	N/A	N/A
201959	0.0 / 0.0	0.0 / 0.0	0.0 / 0.0	0.0 / 0.0	0.0 / 0.0	0.0 / 0.0	N/A	N/A	N/A

Figure 4.10: The second detailed run information table for quantities important to SCT data quality.

The format of displaying the run information in this way also allows a comparison of one quantity, for example the hit efficiencies in the barrel region, over a period of time. A 'history plot', as shown in figure 4.11, displays the values of this selected quantity in the past 100 runs, colour coding the individual data points representing each run to show the DQMF result corresponding to that run. This puts the value in the context of the performance of the SCT over an extended period of time, as well as allow for the identification of trends in the different quantities that may be affected by specific external factors.

4.4.3 The Data Quality Histograms

The values displayed in the detailed information tables described in the previous section show the numerical value related to or summarising each quantity for a given SCT region. Each of these values has an associated histogram, some of which give further information for all individual SCT layers within a region, where the value displayed is the average value across all layers [34].

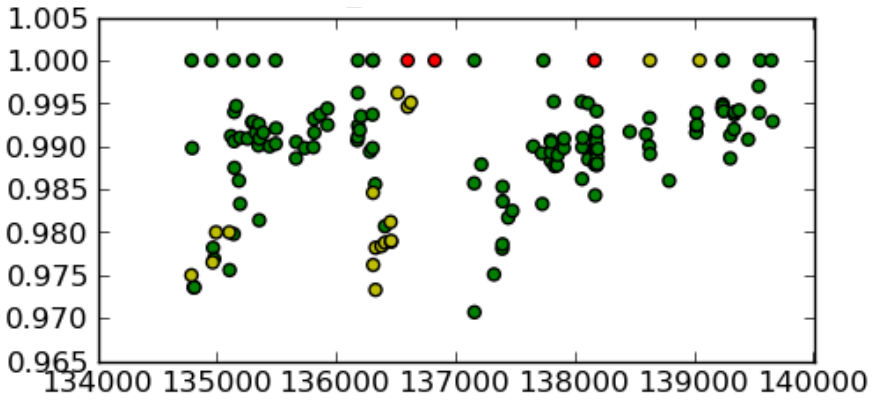

Figure 4.11: The history plot of hit efficiency levels in the SCT barrel region for the most recent 100 runs.

4.4.3.1 The Track Rate

The track rate (or tracks per event) shows the average number of tracks recorded in each of the SCT regions per event during a particular run. Due to the geometry of the detector this rate is expected to be significantly higher in the barrel region than in the two end-caps for collision events and the rate observed in the two end-caps should be approximately symmetrical[2]. In addition the average track rate is required to be above the threshold of 0.2 tracks per event, a run satisfying these criteria is shown on the left in figure 4.12.

If the distribution of the track rates amongst the different SCT regions does not follow the expected pattern or the absolute value of any of the track rates drops below the predefined threshold this is a sign there may be a problem with the run in question.

[2]It must also be noted that an entry is recorded if at least one hit on a track falls within the corresponding region, so one track can contribute to the rate observed in more than one region.

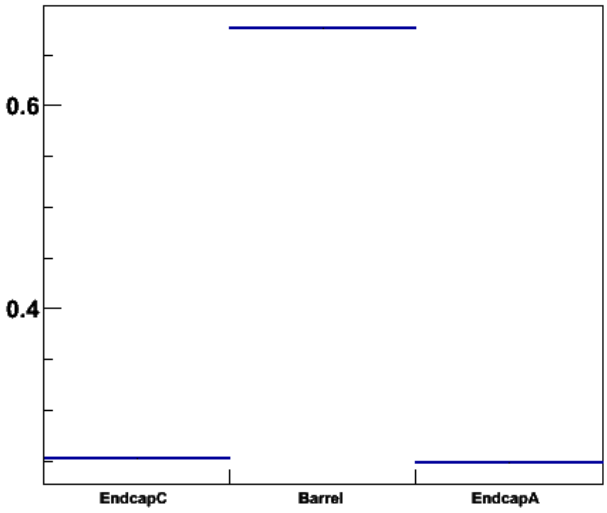

Figure 4.12: The average number of tracks observed per event in the barrel and end-cap regions of the SCT.

4.4.3.2 The Hit Efficiency

The hit efficiency field shows one value representing the average hit efficiency over all the layers in the specified region, the histograms from which this average is calculated show the individual efficiencies measured in each of the layers separately. The efficiency is required to not fall below the threshold of 99.5% in any layer or individual side of a layer for optimal performance, as shown on the left in figure 4.13.

The hit efficiencies of the run in question are also compared to those of a *reference* run. This reference run is chosen purposefully from the same data period to represent the standard in a known 'good quality' run with data taken under the same run conditions. This same reference run is also shown in comparison for each of the quantities described in this section.

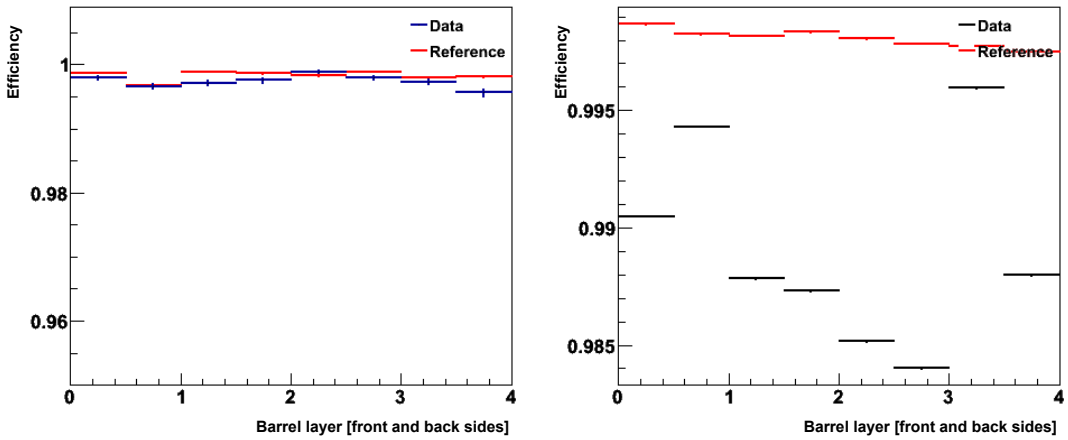

Figure 4.13: The SCT module efficiency per layer (front and back) in the barrel region for a run with high efficiencies (left) and one with lower efficiencies (right).

4.4.3.3 The Track Residuals and Track Pulls

The 'residual' and 'pull' distributions are a measure of how well the individual hits observed form tracks in the SCT and they are therefore a measure of the quality of the tracks themselves, as opposed to the quality of the individual signatures observed to produce the hits. As described in section 3.2.1, tracks in the SCT are constructed from producing a fit to a series of individual hits in the detector.

The residual distributions are produced by measuring the absolute distance of individual hits from the track that is fitted to them. These distances are measured in millimetres (mm), but when summarised in the information table they are scaled by a factor of 1000 and hence given there (figure 4.10 above) in microns (μm). A cleanly observed track should therefore produce a narrow residual distribution with the majority of hits associated with it relatively close to the track itself, as shown in figure 4.14, which shows the overall distribution for the residuals of all tracks observed in the barrel region during one run. This distribution represents the average RMS value for the track residual in a good run of ~ 50 μm, within the SCT tracking resolution given in the previous chapter. If

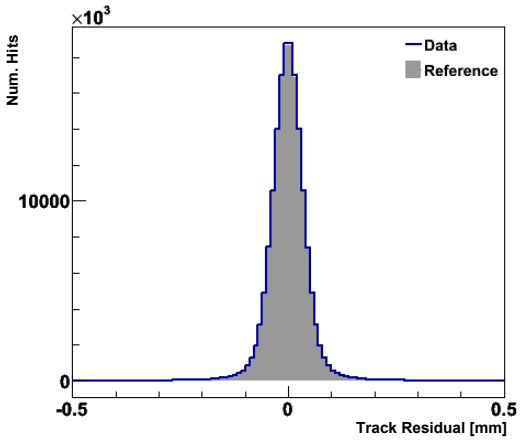

Figure 4.14: The nominal track residual distribution in the SCT barrel region.

this overall distribution becomes wider, then the proportion of poorly fitted tracks in that region during the run is too high, affecting the data quality decision for that run.

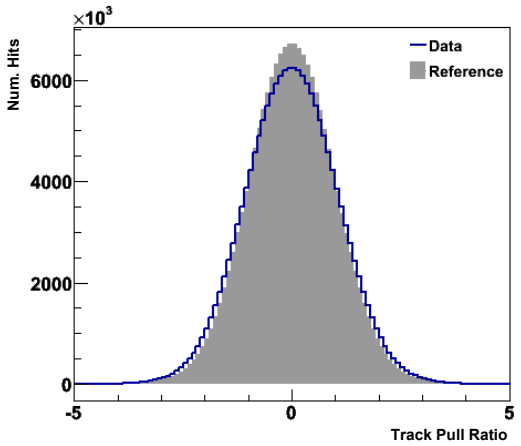

Figure 4.15: The nominal track pull distribution in the SCT barrel region.

The track pull distributions are obtained on a track by track basis by: firstly, measuring the distance from the fitted track to each individual hit that was used to construct it, calculating the total width of the distribution of all of these hits

and then taking the ratio between the two. This is done in order to emphasize the displacements of the mean hit locations relative to a fitted track as a complementary procedure to that of the track residuals. An example of a good quality pull distribution for tracks during a whole run can be seen in figure 4.15. A spike at 0 surrounded by a relatively low background can occur when the width of the hits distribution is much larger than during optimal running, suggesting bad alignment and poor data quality as a result. By definition, the RMS value of the track pull distribution should be unity.

4.4.3.4 The Time Bin Information

The SCT records activity in three separate time bins per event, each with a duration of 25 nanoseconds. Any hit recorded and subsequently used for track reconstruction is ultimately due to some form of activity being seen in a particular module across these three time periods. The particular combination observed is referred to numerically as the 'hit pattern'. The hit pattern is a three-digit binary representation of the combination of activity seen in these time bins in one module, with a one representing activity seen and a zero no activity. The different values it can take are summarised in table 4.1.

The time bins field in the tool displays a ratio which is calculated from the number of hits recorded at the expected time, with binary representation 010, compared to the total number of hits recorded with any (non-zero) hit pattern. The timing of the hits in an event is dependent on the accuracy of the trigger. For example if the trigger is firing $\sim$12 nanoseconds late, approximately half way between the second and third time bins, then the number of entries in the 010, 011 and 001 bins should be roughly equal. Conversely 010, 110 and 100 should be approximately equal if the trigger is firing early. Whereas if the trigger is arriving on time then there should be entries in 010, 110 and 011, as can be seen in figure 4.16. In all cases, the overall distribution should be dominated by real hits either skewed slightly earlier than 010 or slightly later, as opposed to the

#	Binary Hit Pattern	Description
0	000	Error - no hit recorded
1	001	The hit was recorded late or the trigger occurred early
2	010	The hit was recorded at the expected time (optimum)
3	011	An intermediate late recorded hit
4	100	The hit was recorded early or the trigger occurred late
5	101	Background noise
6	110	An intermediate early recorded hit
7	111	Problem in module

Table 4.1: Summary of the binary hit patterns assigned to different module timing combinations.

noise (101) and problematic module signals (111).

4.4.3.5 The Module Summary

The Module Status field shows the average number of modules during a run suffering from some form of problem. There are five different status fields, representing different types of problem, recorded per SCT region for each run. The first of these, 'out' shows the number of modules excluded from the configuration during a given run. All modules are only included/excluded between runs so this number represents an absolute count of the number of individual modules out of that run and unlike the other four status fields therefore always provides an integer.

The remaining four statuses are flagged on a per event basis and so their average value is expected to be non-integer. The first is 'masked' which shows the number of modules masked, 'error' shows the number of modules with an error rate greater that 70% per event, 'inefficiency' shows the number of modules with an efficiency less than 90% and 'noise' shows the average number of noisy modules with a noise occupancy ratio greater than 0.0015. The average number

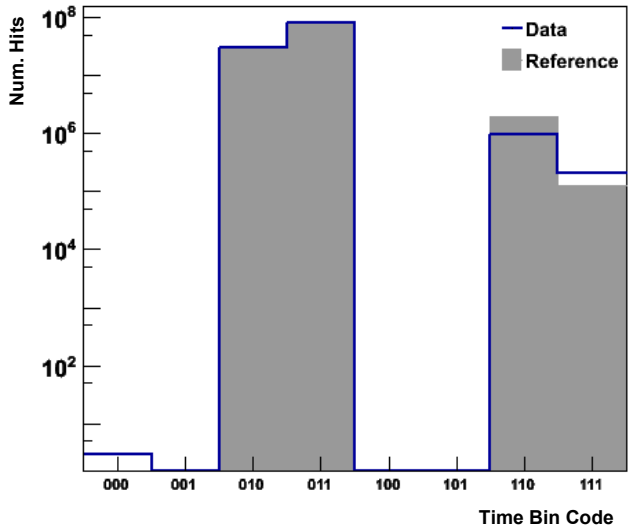

Figure 4.16: The time bins distribution for the barrel section, representing a scenario where the trigger is arriving on time.

of modules showing any one of these problem statuses during a run is required to remain below 40 in each SCT region. A summary of these module statuses is given in figure 4.17.

4.4.4 Shifter Training

In addition to assisting current shifters in their role of assessing the impact of SCT performance on the quality of data collected, the Data Quality WebTool also performs the function of training new SCT Data Quality Offline shifters. Unlike the primary version of the tool, which is automatically provided with the newest runs once they finish reprocessing, the 'training' version of the tool is already loaded with a fixed set of specifically chosen runs. These runs are selected so as to provide a mix of 'good' runs in addition to runs with various different particular problems as a means of instructing the new shifters how, and where, to look for anomalies which could mean a problem for the quality of the data recorded in those runs.

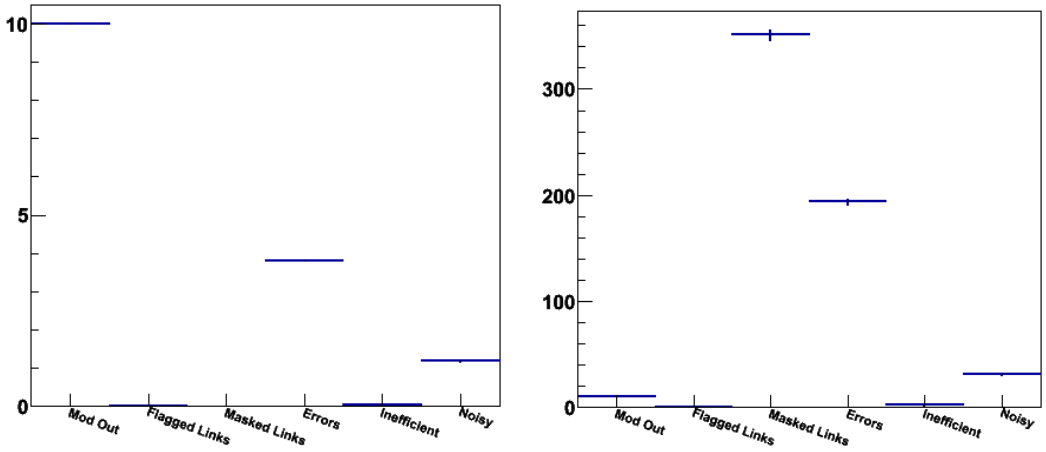

Figure 4.17: The number of modules in the barrel region suffering specified problems at some point during a run, low rates (left) and higher rates (right).

4.4.5 Luminosity Block Histograms

The information that the Data Quality WebTool provides on relevant quantities for DQ decision making is taken from measurements made across the entirety of a run. As the data quality decisions are made on a luminosity block level, an additional and complimentary tool was created to provide information on some of these quantities within each run on a per luminosity block level. Detailed information can in this way be identified with individual luminosity block groups within a run and not just to the run itself, in addition the behaviour of these quantities can then be studied over time during each run and any anomalies or patterns highlighted.

The quantities detailed on a per luminosity block level in this tool are the number of hits recorded, number of 'space-points', module error rates and the track rates. The number of hits recorded in each of the four barrel layers over the first 10 luminosity blocks of a run are shown in figure 4.18.

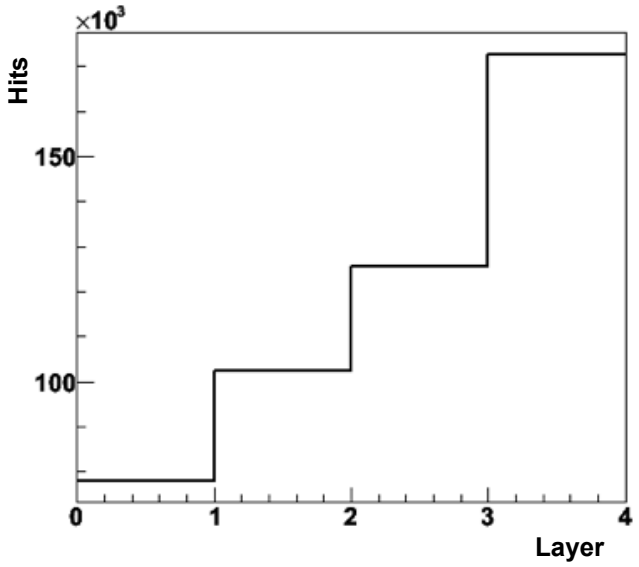

Figure 4.18: The number of hits in the four separate layers of the SCT barrel region during run 153407 in the luminosity block range 1-10.

Chapter 5

Object Reconstruction and Identification

The ATLAS detector, through its various sub-detector systems, described individually in section 3.2, does not detect and identify elementary particles directly, but instead it records various signatures independently in whichever parts of the detector show activity. These signatures include firstly the presence and trajectory of tracks left by electrically charged particles as they pass through the inner detector, secondly the deposition of energy in one or both of the calorimeter regions and finally the activity seen in the outer muon chambers. From this information 'objects' in the detector in any given event must be inferred from the full combination and interpretation of all the recorded quantities that are observed in every region of the detector in that event, followed by the subsequent reconstruction of their properties and their paths through the detector.

An example display of an event recorded in the ATLAS detector is shown in figure 5.1. The cross-sectional view (left) and side view (top right) are both depicted in the 'fish-eye' style, meaning that the central region representing the inner detector and calorimeters are accentuated in size relative to the outer regions of the detector, which are correspondingly shrunk. This is done to allow

reconstructed tracks in the inner detector to be more easily distinguished[1]. The event shown contains various reconstructed objects which include an electron (shown in blue), a muon (red) and two jets (green), this event also has a missing transverse energy associated with it (light blue) which is not observed directly, but calculated indirectly as described in section 5.3.1.

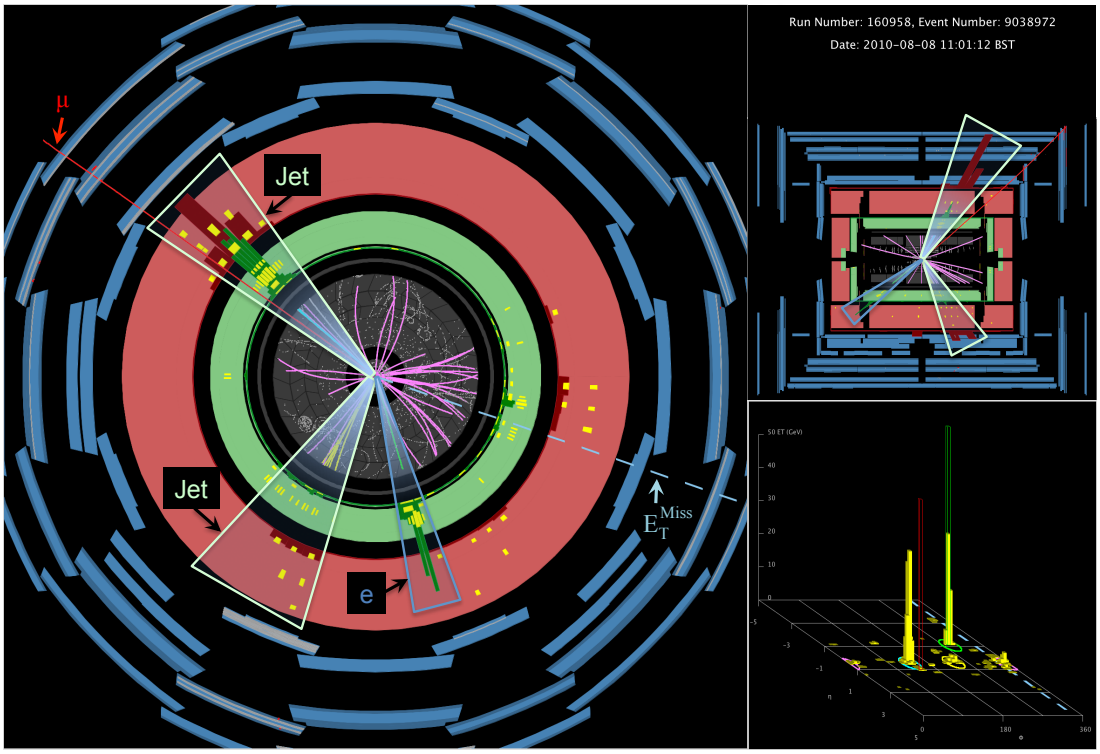

Figure 5.1: An event in the ATLAS detector showing reconstructed objects in an event, including an electron (blue), a muon (red), two jets (green) and an inferred missing energy (light blue).

The region comprising the inner detector is shown as the central region shaded grey in figure 5.1, this whole region is immersed in a magnetic field produced by the solenoid magnet that surrounds it, which is described in section 3.2.1. Keeping this magnetic field constant throughout the recording of collisions is what allows for the determination of the momentum and sign of electric charge of a particle

[1]See figure 3.2 for an accurate detector scale.

passing through this region.

The two calorimeter regions, the Liquid Argon (LAr) calorimeter and the Hadronic Tile calorimeter (shown in green and red respectively in figure 5.1), are described in section 3.2.2. The primary purpose of these calorimeters is to measure the magnitude of the energy an object that impinges upon it carries. External to the calorimeters is the Muon Spectrometer region (shown in blue in figure 5.1) whose job is solely to identify muons.

There are three main types of observable objects seen in events that are relevant to this analysis. The first two of these are the lightest two of the three charged standard model leptons, namely electrons and muons. The heaviest of the charged leptons, the tau lepton, has a lifetime too short to traverse the distance from the interaction point to the first sensitive material of the inner detector, thus wherever they may be produced in the detector they will decay to other lighter leptons and/or hadrons before being directly observed. The third category of event object considered here is what are referred to as 'jets'.

The fourth quantity considered in this analysis is that of the missing transverse energy in an event, which, unlike the other objects explained above, is not directly observable in the detector and must be inferred from the prior reconstruction of all other objects in an event and the summation of their combined transverse momenta.

5.1 Reconstructed Objects

In the following sections the methods used to reconstruct the main objects applicable to this analysis, specifically the electrons, muons and jets, will be detailed.

5.1.1 Electrons

Electrons are electrically charged and therefore leave tracks in the various components of the inner detector and eventually deposit their energy in the Liquid

Argon calorimeter through the process of an electromagnetic shower, shown in figure 5.2. An object in an event is regarded as an 'electron candidate' by the matching of a cluster of active cells in the calorimeter to a corresponding charged track in the inner detector. Valid electron candidates must lie in the region $|\eta|$ < 2.47 to be considered for reconstruction.

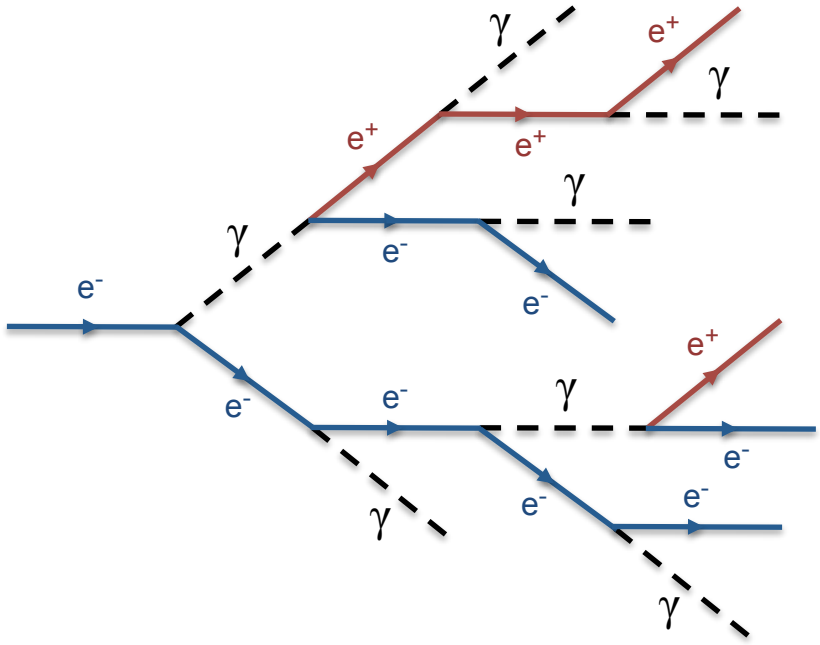

Figure 5.2: An electron inducing an electromagnetic shower in the Liquid Argon calorimeter involving cascade decays of photons (γ) and pair produced electrons (e^-) and positrons (e^+).

A set of requirement cuts are applied independently to the various properties of electron candidates to facilitate their identification, different 'reference' categories consisting of groups of these cuts are defined and electrons candidates are required to pass the *medium* category definitions, where the full definition of this group of cuts and the optimisation of their values is described in [35].

Properties relating to both the tracks and the energy deposits in the calorimeters are constrained with these cuts. They include conditions that are applied to ensure that the tracks associated with candidate electrons are of sufficient quality

for the reconstruction by requiring a minimum number of 'hits' in the inner detector silicon regions - a total of 9 hits in the pixel and SCT detectors combined, with at least 1 of those hits in the pixel detector. In addition the transverse impact parameter of the tracks relative to the primary vertex is required to be less than 1 mm. In the calorimeters the level of acceptance of the hadronic leakage is constrained by the ratio of transverse energy deposited in the first layer of the hadronic calorimeter to the transverse energy associated with the cluster observed in the electromagnetic calorimeter.

5.1.2 Muons

Muons are electrically charged and therefore, like electrons, leave tracks in the various components of the inner detector. They only deposit, however, negligible amounts of energy in the calorimeter systems so matching the tracks they leave to the energy depositions in the calorimeters is not a viable method of reconstructing their paths in the detector as in the case of electrons. Muons do however have a very long lifetime relative to other unstable elementary particles of $\tau = 2.2 \times 10^{-6}$ seconds [6], this is long enough for it to escape the confines of the inner detector and calorimeter regions before it decays. All other particles are either stopped by the calorimeters, depositing all of their energy in the process, or decay before that point into particles which are themselves subsequently stopped in the calorimeters. Therefore any signature present in the muon spectrometer that matches with a track in the inner detector region is taken as a muon candidate using the STACO combined algorithm described in [35].

Valid muon candidates must have a $p_{\mathrm{T}} > 10$ GeV and fall within the range $|\eta| < 2.4$. Muon quality requirements are also made in order to distinguish between muons originating from a collision event and those coming from cosmic rays and pass through the detector whilst a collision event is being recorded.

5.1.3 Jets

Jets are streams of particles formed from the sequential hadronization of strongly interacting particles, quarks and gluons. These particles cannot exist in isolation and combine with quarks that are spontaneously produced in the vacuum forming hadrons. This process continues until no new hadrons can be kinematically produced. The cascade process forms in the shape of a narrow 'jet' due to the high relativistic momentum of the initially produced particle meaning all subsequent decay products will in turn be produced in approximately the same direction.

Jets are reconstructed first from locating appropriate energy deposits in the calorimeters, these energy 'clusters' are identified using the topological (Topo) cluster algorithm. The clusters identified in this manner are then used as the starting point to the full jet reconstruction using the 'Anti-k_t' algorithm [36] by creating a cone of radius, $\Delta R = 0.4$ around the original cluster location, where ΔR was defined in equation 3.4 as a distance in the $\eta - \phi$ plane.

b-jets

As explained in section 2.4.2, the analysis in this work focuses heavily on the production and subsequent identification of *b*-jets in events. This particular type of jet is the same in nature as any ordinary jet as described above, except that they are jets that were produced originally from a *b*-quark rather than a lighter flavoured quark. A *b*-jet can be identified through a variety of different methods, which exploit the distinguishable characteristics of the *b*-quarks that created them, in order to separate them from the jets produced by other quarks.

The method used to identify the *b*-jets in this analysis was one of exploiting the known lifetime of hadrons containing *b*-quarks and hence of measuring the distance they travel in the detector before decay. This method is introduced and described in detail in chapter 6.

5.2 Removal of Overlapping Objects

Therefore once all electrons, muons and jets in an event have been reconstructed, their angular positions in the detector are compared with one another to check for any potential spatial overlaps between the different reconstructed objects. This overlap removal is carried out due to the possible ambiguity of one object in the detector passing the requirements of more than one of the reconstruction processes described above.

This is a very real possibility given the similar signatures the leptons and jets can leave in the inner detector and calorimeter. For this reason an order of precedence is defined between different types of reconstructed object as outlined in the following procedure. In this procedure only jets reconstructed with a $p_{\mathrm{T}} > 20$ GeV and $|\eta| < 2.5$ are considered, jets with p_{T} and $|\eta|$ outside of these ranges will then subsequently be discarded from an event so any potential overlaps in these cases are safely ignored.

In carrying out overlap removal, firstly any jets that are aligned within $\Delta\mathrm{R} < 0.2$ of an electron is removed from the event and the electron in question is taken. After the consideration of all selected jets in an event a further comparison is made requiring all leptons to be separated from all remaining jets with a $\Delta\mathrm{R} > 0.4$, the radius of the jet reconstruction algorithm cone. Any leptons within this distance of a surviving jet are removed, $\Delta\mathrm{R} < 0.4$ for muons and, given the first removal step, $\Delta\mathrm{R}$ between 0.2 and 0.4 for electrons. A summary of this process is shown in table 5.1 in sequential order starting from comparing all jets followed by electrons followed by muons.

Once this procedure has been carried out for a given event all surviving jets and leptons are accepted and fully considered as their respective reconstructed objects for the purposes of the subsequent event selections that will be applied to distinguish between different events.

Cycle over reconstructed objects	Condition	Action
Jets ($p_{\mathrm{T}} > 20$ GeV, $\lvert\eta\rvert < 2.5$)	If **electron** within $\mathbf{\Delta R < 0.2}$	Remove **jet** from event
Electrons	If **jet** within $\mathbf{0.2 \leq \Delta R < 0.4}$	Remove **electron** from event
Muons	If **jet** within $\mathbf{\Delta R < 0.4}$	Remove **muon** from event

Table 5.1: A summary of the overlap removal procedure.

5.3 Other Quantities in Events

Along with the physical observable objects which appear in the detector, there are other properties possessed by an event which can be used to discriminate between different events. The quantities of missing transverse energy and effective mass which are described in the following sections are particularly useful to this analysis.

5.3.1 Missing Transverse Energy

As the colliding protons have no component of their momentum that is transverse to the beamline at the point of collision no final *net* momentum should be expected in the transverse plain either. The detector allows the individual transverse energies emanating from the interaction point to be deduced through a combination of measurements. Firstly, in order from the interaction point outwards, that of the degree of curvature of tracks left by charged particles in the inner detector, secondly the amount of energy deposited in the one or both of the electromagnetic and hadronic calorimeters and lastly, in the case of muons only, signatures left in the muon spectrometer system.

This therefore means that any neutral particle, which will naturally leave no track in the inner detector or signal in the electromagnetic calorimeter, that also deposits none of its energy in the hadronic calorimeter, will escape the detector unseen if it possesses a lifetime that allows it to traverse the entire detector region without decaying into subsequently detectable particles. The result of this undetected product from a collision event escaping the detector is a net

discrepancy in the balance of the total amount of transverse energy observed in any given event after corrections are made to account for known sources of energy measurement discrepancy such as inactive material in the calorimeters.

Neutrinos constitute the standard model explanation for the entirety of the observed missing transverse energy in events, as the only currently known particle to fulfil all of the above conditions and hence to leave no signature of any kind in the detector. In physics beyond the standard model, as yet undiscovered particles could also escape detection and therefore contribute to this net imbalance represented by the total missing energy alongside neutrinos. In the context of supersymmetry the particle which also fulfils these conditions is the lightest super-symmetric particle (LSP) which, in the model considered in this analysis, is the lightest neutralino (see section 2.3.1). The neutralino, also being predicted to be stable, will be able to escape the detector region, whereas all other super-symmetric particles will eventually decay whilst still in the confines of the detector, as described in section 2.4.

5.3.2 Effective Mass

Also used in this analysis is the value of Effective Mass, which is not an object in itself, but a composite quantity calculated from the energies of multiple objects in an event. The effective mass in an event is defined as the sum of the transverse momenta, p_{T}, of the first three jets ordered in p_{T} and the sum of the p_{T} of all the leptons in that event together with the missing transverse energy, $E_{\mathrm{T}}^{\mathrm{miss}}$, in the event. This quantity is defined in equation 5.1. A term involving the total p_{T} of all the leptons in an event ($\Sigma p_{\mathrm{T}}^{\mathrm{lep}}$) is also included in the general expression of the effective mass[2], but as no leptons are present in the events that this calculation is applied to in this analysis, the term is not relevant here.

$$M_{eff} = \Sigma p_{\mathrm{T}}^{\mathrm{jet}} + E_T^{miss}. \tag{5.1}$$

[2]The general definition is then $M_{eff} = \Sigma p_{\mathrm{T}}^{\mathrm{jet}} + \Sigma p_{\mathrm{T}}^{\mathrm{lep}} + E_T^{miss}$

Along with the number of jets tagged as b-jets the amount of effective mass measured in an event, using this definition, will be used in the following analysis to define the separate specific signal regions where the process being searched for is attempted to be distinguished from the background.

5.4 Required Event Information

As explained in section 2.4.2, the final state of the process this search is focussed on will include jets, b-jets in particular, and missing transverse energy. Therefore the successful identification of these constituents of an event, along with the accurate calculation of the effective mass as a combination of these constituents, is extremely important to the analysis as a whole. Once identified the properties of these constituents can be studied in detail.

The successful identification of both electrons and muons is also just as important as these entities must *not* be present in any event regarded as a candidate in the search and the stipulation that there are none must be accurate.

Chapter 6

b-tagging in Supersymmetry Searches

In this chapter a study on the performance of two methods of b-tagging is presented. The process of identifying (tagging) which jets observed in the detector originate from b-quarks as opposed to lighter flavour quarks is of pivotal importance to any physics analysis that focuses on searching for events that contain jets of this kind in the final state.

Here the different b-tagging methods used are described, followed by a discussion of the efficiency of these algorithms, then a procedure which accounts for the different efficiencies seen in data and Monte Carlo simulation is introduced and finally the observed performance of these algorithms in the context of supersymmetry searches is detailed.

6.1 Introduction to the b-tagging Algorithms

The identification of b-jets, as distinguished from lighter flavour jets, in ATLAS is known as b-tagging. The process of b-tagging involves following a particular algorithm and there are many different algorithms designed to tag b-jets, which use a variety of different methods. The algorithms employed in this study are the

'SV0' and 'JetFitter' algorithms and these two different methods are described in the following sections.

6.1.1 The SV0 Algorithm

The Secondary Vertex (SV0) algorithm is a process based primarily upon the lifetime of the b-quark and its performance in early 7 TeV data is discussed in reference [37]. The algorithm reconstructs secondary vertices within jets and can, because of the relatively long lifetime of hadrons containing b-quarks of approximately $\sim 1.5 \times \ 10^{-12}$ seconds [8], attempt to distinguish between b-jets and other quark flavour jets[1] due to the different distance in the detector these lifetimes will allow them to traverse.

The SV0 algorithm does this by calculating what is known as the 'decay length significance' (S) of each of the reconstructed secondary vertices on a per jet basis. The decay length, L, is equal to the distance between the secondary vertex in the jet and the primary vertex in the parent event and the significance is defined as the ratio between this measurement and its uncertainty

$$S = L/\sigma\left(L\right). \tag{6.1}$$

An illustration of a secondary vertex in a jet, with the decay length indicated, is shown in figure 6.1. The calculation of the significance of this decay length is the final step in the procedure, which is only possible once a secondary vertex has been successfully reconstructed in a jet by the algorithm, from a sub-set of the tracks which that jet contains.

The input fed into the SV0 algorithm was the location of the primary vertex in an event and a list of tracks associated with each jet in that event, within a

[1]In comparison charm flavour hadrons typically have a lifetime $\sim 4 \times 10^{-15}$ seconds and lighter flavour (u, d, s) hadrons shorter still

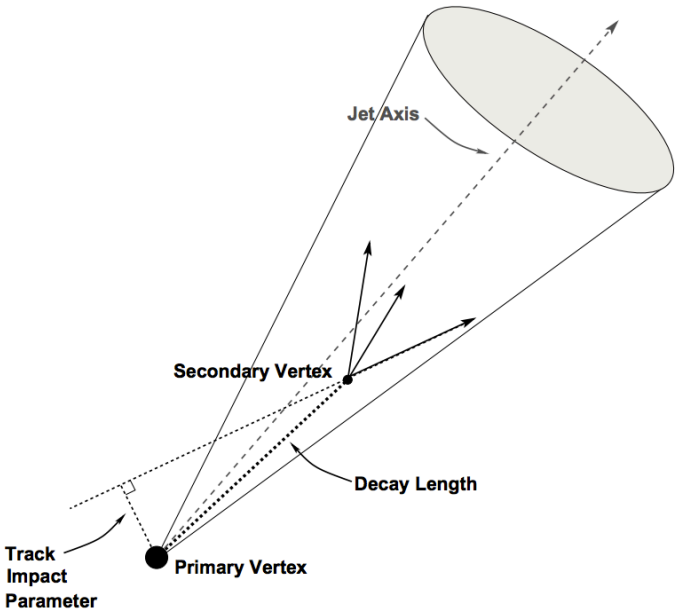

Figure 6.1: A secondary vertex reconstructed in a jet with the SV0 Algorithm. The secondary vertex is reconstructed from tracks that have a high impact parameter significance with respect to the primary vertex.

$\Delta R < 0.4$ of the jet axis. A set of cuts are applied to the properties of these tracks in order to ensure that only those which converge in a distinctly different location to the primary vertex are used to construct any secondary vertex. The most important of these properties is the 'impact parameter' of the track, shown in the image above, this parameter is a measure of the point of closest approach a particular track has to a certain location, in this case the primary vertex. There are two separate quantities representing the impact parameter, one for closest approach in the transverse (d_0^{PV}) and the other in the longitudinal direction (z_0^{PV}).

Only tracks passing the thresholds listed in table 6.1 are used to reconstruct the secondary vertices. The quantities shown here in addition to the impact parameters themselves are, the uncertainty of the measurements of those impact

parameters ($\sigma(d_0^{PV})$, $\sigma(z_0^{PV})$, the chi-squared per number of degrees of freedom (χ^2 / ndof) of the fit to the tracks and the number of hits in both the Pixel and SCT regions of the inner detector. The application of these cuts ensures both that the tracks did not originate in the primary vertex and that they are reconstructed with a good quality in the detector.

Track Property	Threshold
Track p_{T}	> 0.5 GeV
Impact parameter d_0^{PV}	< 2 mm
Impact parameter $z_0^{PV} \sin\theta$	< 2 mm
Resolution $\sigma(d_0^{PV})$	< 1 mm
Resolution $\sigma(z_0^{PV})$	< 5 mm
χ^2 / ndof	< 3
Number of Pixel hits	≥ 2
Number of SCT hits	≥ 4
Number of Pixel + SCT hits	≥ 7

Table 6.1: Selection criteria applied to jet tracks by the SV0 algorithm.

Initially two track vertices are formed separately using this process, then one single inclusive vertex is created from the merger of each of these proto-vertices together and in an iterative process the worst single track is removed, one at a time, until the largest χ^2 contribution of any one track is less than 7 and the overall vertex mass is less than 6 GeV.

The decay length significance of each jet can then be calculated from the final secondary vertex formed in this manner, with the tracks that pass the prior requirements. For each jet in an event the SV0 algorithm returns one value for this significance reflecting this final reconstructed vertex. A high value for this final significance is taken to indicate the presence of a long lived particle in the jet and here a jet is considered to be *tagged* as a *b*-jet specifically, if the decay length significance for that jet is greater than 5.85. This value is known as the

'operating point' of the algorithm and, with the value taken here, corresponds to a b-tagging efficiency of 50% for this algorithm. Sometimes a lighter flavour jet may pass this threshold and also be tagged as a b-jet erroneously, referred to as mistagging, the mistag efficiency of the SV0 algorithm at this same operating point is approximately 1% and a light jet rejection rate of $\sim$200 [38].

6.1.2 The JetFitter Algorithm

The JetFitter algorithm works in principle in the same way as the SV0 algorithm, utilising the lifetime of the hadrons containing b-quarks and reconstructing secondary vertices from impact parameter displaced tracks [39].

The primary difference between the two approaches is that the JetFitter method takes into account the fact that sometimes hadrons containing charm quarks (D-hadrons) are subsequently produced in the decay of the B-hadrons, the tracks emanating from which the SV0 procedure treats inclusively to produce one overall reconstructed vertex. This vertex will be displaced from its true B-hadron location and be a compromise in position between the two true sub-vertices, inadvertently increasing the decay length of the B-hadron vertex in question.

The JetFitter algorithms treatment in this scenario differs and figure 6.2 illustrates this difference in the case where a D-hadron is produced. Displayed in this image on the left is the SV0 algorithm reconstructing a single inclusive vertex from the tracks associated with both the B and the D-hadron using the procedure described above.

The JetFitter method on the right makes the assumption that both the B and D-hadron vertices lie on the flight path of the B-hadron from the primary vertex, which is a good approximation to within the average resolution of the inner detector tracking which measures them. This assumption allows for invoking the criteria that every track used to construct the two vertices will intersect this flight path at some point, decreasing the total number of degrees of freedom for the χ^2

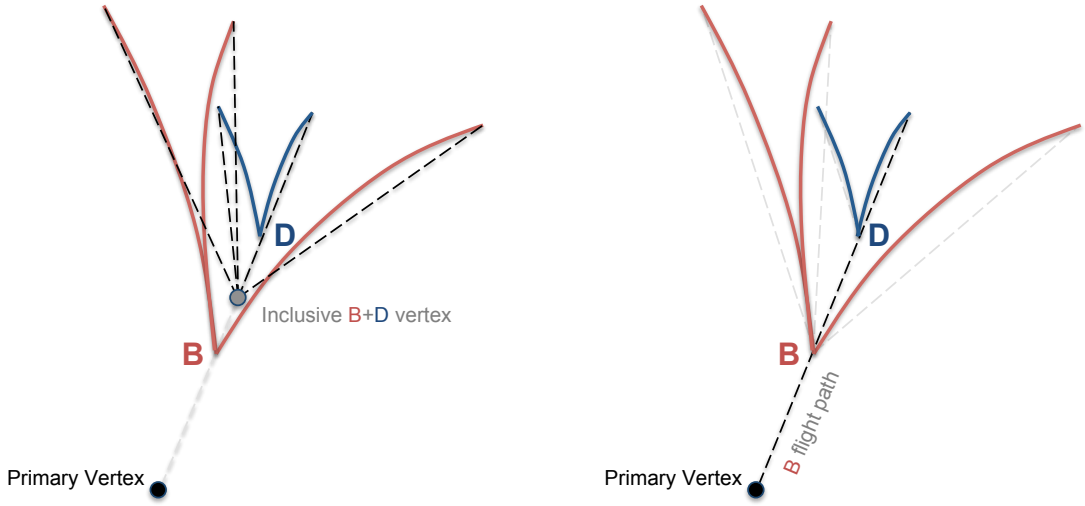

Figure 6.2: The SV0 method reconstructing an inclusive B+D hadron vertex (left) and the JetFitter method performing a multi-vertex fit using the B flight path as a constraint.

iterative fit procedure and hence increasing the probability that the two vertices will be separable. In addition this fit evaluates how compatible a particular track topology is with that expected from a B $\longrightarrow$ D-hadron decay, increasing the discriminating power of this method against lighter flavour jets.

Analogously to the SV0 algorithm, the JetFitter algorithm produces a 'flight length significance' (d_{SV} / $\sigma(d_{SV})$ for each of the vertices reconstructed along the B-hadron flight path. Here a jet is considered to be tagged as a b-jet if this significance is greater than 2.0, corresponding to a b-tagging efficiency of 60% and a mistag efficiency of approximately 1% and a light jet rejection rate of $\sim$200 [38].

6.2 b-tagging Efficiency Calibration

This process of tagging or not tagging a jet in an event is of course not always successful in determining the true nature of origin of the jet in every case. The tagging algorithm therefore has an efficiency associated with it, which is depen-

dent upon the operating point used in any given situation.

The efficiency of the b-tagging in data is observed to be different to that seen in Monte Carlo simulation, so in order to provide a meaningful comparison between the two, this difference is reconciled by calibrating the efficiency in Monte Carlo to match that observed in the data. This calibration procedure is known as the $p_{\mathrm{T}}^{\mathrm{rel}}$ method [40]. As illustrated diagrammatically in figure 6.3, this method, using jets containing muons, involves the extraction of the p_{T} component of those muons that is perpendicular relative to the jet axis, a quantity known as $p_{\mathrm{T}}^{\mathrm{rel}}$. The relative transverse momenta of these muons are then used to produce template shapes for both b-jets and non b-jets in the simulation and for all jets in data.

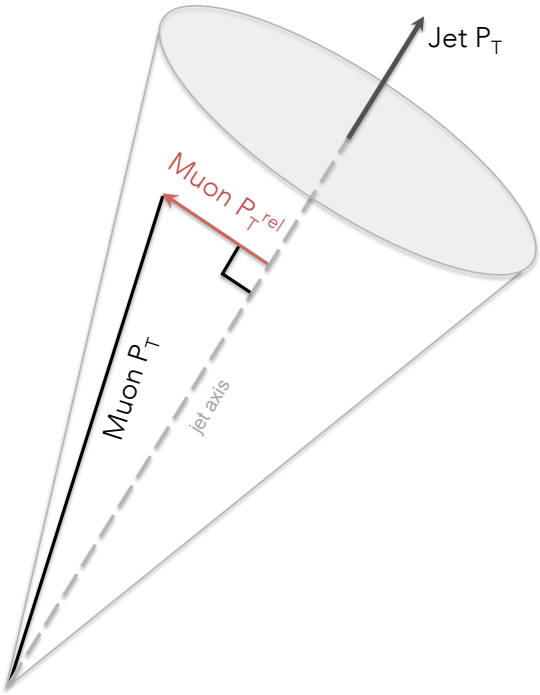

Figure 6.3: The p_{T} component of a muon relative to the axis of its parent jet used in the construction of $p_{\mathrm{T}}^{\mathrm{rel}}$ templates.

The templates of these relative p_{T} spectra for each type of jet, are produced both before and after the b-tagging procedure described in the previous sections

has been carried out. Figure 6.4 shows these templates, before and after b-tagging from 2.9 pb^{-1} of early 7 TeV data. Given that muons stemming from b-quark decays are more boosted relativistically than those stemming from lighter quark decays, then the resulting difference between the fit to data of these two p_{T} spectra can be used to measure the fractional contribution of each. A comparison of these templates, both before and after b-tagging, to the $p_{\mathrm{T}}^{\mathrm{rel}}$ spectra of muons stemming from jets in data provides a value for the fraction of b-jets at both stages. The fraction of b-jets obtained after applying the b-tagging cut should be given by the b-tagging efficiency of the algorithm used, but this is not observed to be the case and so a scale factor is introduced to correct the value in the Monte Carlo simulation.

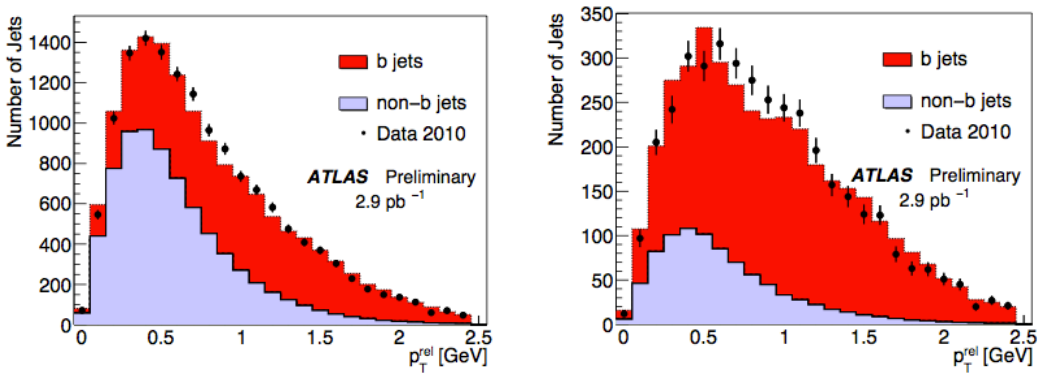

Figure 6.4: The muon $p_{\mathrm{T}}^{\mathrm{rel}}$ template for both b-jets and lighter flavour jets, before (left) and after (right) the b-tagging procedure [40].

This scale factor (SF) is therefore defined using the ratio obtained from the efficiency (ϵ) observed in data and the efficiency in the Monte Carlo simulation. Separate scale factors are formed in the case of b-jets and of lighter flavour jets, and they are defined as

$$SF_b = \epsilon_b^{data}/\epsilon_b^{MC} \tag{6.2}$$

$$SF_l = \epsilon_l^{data}/\epsilon_l^{MC} \tag{6.3}$$

The systematic uncertainties on the efficiencies and therefore also on the scale factors affect the distribution shape of the $p_{\mathrm{T}}^{\mathrm{rel}}$ templates and are therefore determined by repeating the fitting procedure of the templates to data using these modified templates.

The performance of the b-tagging algorithm depends upon the p_{T} of the jets and so the $p_{\mathrm{T}}^{\mathrm{rel}}$ fits are performed in set ranges or 'bins' of jet p_{T}, the scale factors are therefore also given in these same p_{T} bin ranges, which are

- 20 GeV $\leq p_{\mathrm{T}} \leq$ 30 GeV
- 30 GeV $\leq p_{\mathrm{T}} \leq$ 60 GeV
- 60 GeV $\leq p_{\mathrm{T}} \leq$ 90 GeV
- 90 GeV $\leq p_{\mathrm{T}} \leq$ 140 GeV

The $p_{\mathrm{T}}^{\mathrm{rel}}$ of the muons is too difficult to distinguish in jets with low p_{T}, which sets the lower p_{T} limit for the application of this procedure. Above 140 GeV the scale factor value for the last bin is used, with twice the systematic uncertainty associated to the value estimated for this bin. The values for c-tagging scale factors are taken to be equivalent to those of the b-tagging scale factors here, but to account for the fact that this is only an assumption and no substantial evidence for this equality is available, the systematic uncertainty in this case is increased by a factor of two also.

The value of these scale factors, for b flavour jets, taken in the current analysis are shown in the five p_{T} bins in figure 6.5 for both the SV0 and JetFitter b-tagging algorithms. The optimum jet p_{T} for agreement on the b-tagging efficiency between

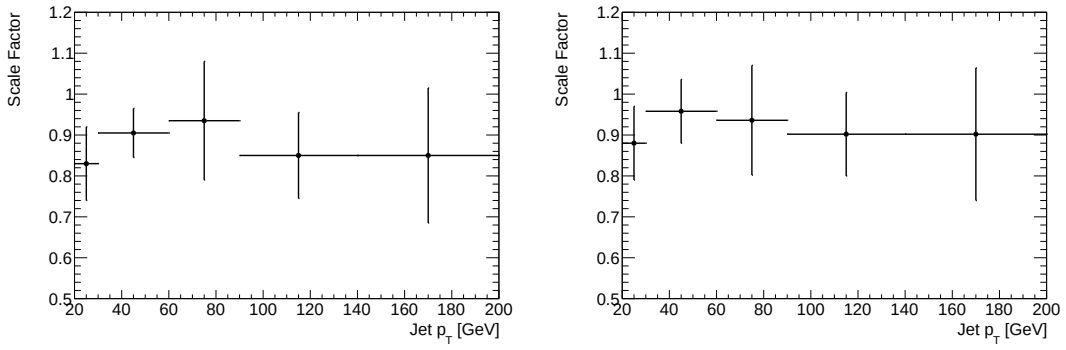

Figure 6.5: The jet p_{T} dependent efficiency scale factors, with associated systematic uncertainties, for b-flavour jets for the SV0 (left) and JetFitter (right) b-tagging algorithms.

data and Monte Carlo for SV0 is between 60 and 90 GeV and for JetFitter it is between 30 and 60 GeV. Above a jet p_{T} of 30 GeV the JetFitter algorithm is more closely matched in the simulation.

Also shown in figure 6.5 are the systematic uncertainties applied to the scale factors in each p_{T} bin, estimated from the repeated fitting of the $p_{\mathrm{T}}^{\mathrm{rel}}$ templates described above. The magnitude of these uncertainties is greater for the JetFitter algorithm between 30 and 60 GeV and greater for SV0 between 60 and 90 GeV, the two sets of uncertainties are equal above 90 GeV.

6.2.1 Implementing the b-tagging Efficiency Calibration

A method was developed in order to integrate this data to Monte Carlo calibration procedure into general supersymmetry analyses, with the goal of providing the appropriate contribution to overall systematic uncertainty in these analyses from the b-tagging procedure.

In this method the calculated scale factors are used to determine a weight value to apply to each jet in an event with $p_{\mathrm{T}} \geq 20$ GeV and $|\eta| \leq 2.5$ and subsequently

a weight for the event as a whole. These weights correct the tagging rate in Monte Carlo to that observed in the data. They are obtained for the individual jets in two distinct ways, firstly in the case where the jet is tagged as a b-jet, the weight is given directly by the scale factor

$$w_{jet} = SF_{Flavour}, \tag{6.4}$$

where the subscript $Flavour$ refers to the quark flavour of the jet in question, b or non-b, and determines which of the scale factors in equations 6.2 and 6.3 is to be used. In the case where the jet in question is not tagged as a b-jet, the quantity $1 - \epsilon$ must be used in place of the efficiency (ϵ) itself. The weight is therefore given by

$$w_{jet} = \frac{1 - \epsilon^{data}_{Flavour}}{1 - \epsilon^{MC}_{Flavour}} = \frac{1 - SF_{Flavour}\epsilon^{MC}_{Flavour}}{1 - \epsilon^{MC}_{Flavour}}. \tag{6.5}$$

The weight applied to the event as a whole is then obtained by the product of all the weights of the individual jets in that event,

$$w_{event} = \prod_{jet} w_{jet}. \tag{6.6}$$

The event weight w_{event} and the individual jet weights w_{jet} are then subsequently used in order to obtain all Monte Carlo estimations of event and jet yields in the analysis respectively.

The contribution to the overall systematic uncertainty in an analysis from the b-tagging efficiency is therefore calculated by propagating the estimated uncertainties on the original scale factors, shown in figures 6.5 and **??**, to the individual jet and whole event weights. The analysis can then be run separately with the

event weights shifted up and down by the 1σ uncertainty bounds, providing the uncertainty on the expected Monte Carlo event yields.

6.3 Performance of the b-tagging Algorithms

As explained the b-tagging calibration procedure assigns event (and individual jet) weights based on p_{T} and quark flavour dependent scale factors, which correct the b-tagging efficiency in Monte Carlo to that observed in the data [41]. It is therefore important to know whether the systematic uncertainties on the scale factors used are adequate to account for the differences between data and Monte Carlo when applying the b-tagging requirement in this analysis. In this section, the comparison of these differences pre and post b-tagging, the b-jet fraction, the degree to which the b-jet fraction has a run period dependence and the effect of the missing energy requirement on these factors are studied.

Selection	Threshold
Pre-selections cuts[2]	
Number of vertices	≥ 1 primary vertex with ≥ 5 tracks
Lepton vetoes	No-lepton with $p_{\mathrm{T}} \geq 20$ GeV
Jet Requirements	Jet $p_{\mathrm{T}} \geq 120$, 50, 50 GeV, $\lvert\eta\rvert \geq 2.5$
Missing Energy	$\mathbf{E}_T \geq$ **50 GeV**
Jet / missing E_T separation	$\Delta\phi_{min} \geq 0.4$ rad

Table 6.2: Summary of the event selections for the QCD dominated sample region under study. The $E_{\mathrm{T}}^{\mathrm{miss}}$ modification to the analysis QCD control region is highlighted.

The QCD Enriched Region

This study was carried out in a modified version of the control region used to estimate the QCD background in the analysis, which will be described in detail in section 7.4.1. This region was chosen so as to allow the study to be carried out on a well defined set of events. The event selection criteria used here are shown in table 6.2. The primary difference with the QCD background estimation region is that here a value for the missing energy in an event of $E_{\mathrm{T}}^{\mathrm{miss}} \geq 50$ GeV was required in order to increase the available statistics for the study, due to the lower amount of missing energy present in typical QCD events. In the study region considered, whilst the QCD contribution dominates, the top and boson contributions are negligible.

The Tagging Algorithm Performance Study

As is the case for any candidate jet considered for b-tagging in this analysis, only jets with $p_{\mathrm{T}} \geq 25$ GeV are considered in this study. Additionally, again as is the case in the primary analysis requirements, all individual jets studied must be separated from the missing energy in the event by $\Delta\phi \geq 0.4$. This is despite the $\Delta\phi_{min} \geq 0.4$ event-level requirement which, as explained above, was applied to ensure the QCD dominated event sample. This way the jets studied here are the ones relevant to the analysis search presented in the next chapters.

The transverse momenta of these jets in data and Monte Carlo, is shown in figure 6.6 before the b-tagging procedure. The same distribution after the b-tagging procedure is shown in figure 6.7 for both the SV0 and JetFitter algorithms, in these distributions, the b-tagging calibration procedure, introduced in the previous section, has been applied to the Monte Carlo. In these distributions, as well as the ones to follow, the higher p_{T} regions have been collated in order to maximise the statistics available in each p_{T} bin.

[2]The pre-selections cuts include the data quality requirement, trigger requirements, the rejection of misidentified jets and electron fiduciality requirements.

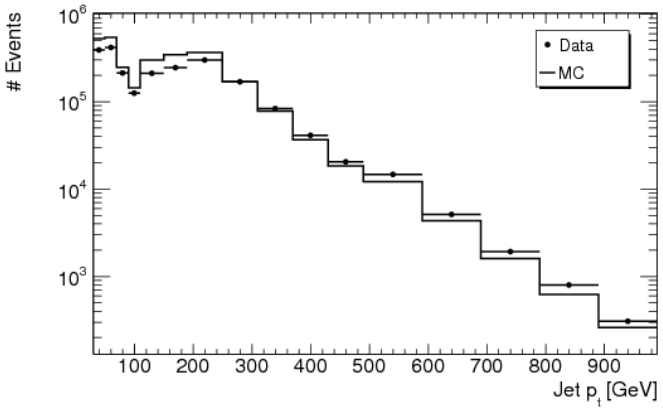

Figure 6.6: The jet p_{T} distribution for data and Monte Carlo before the b-tagging procedure.

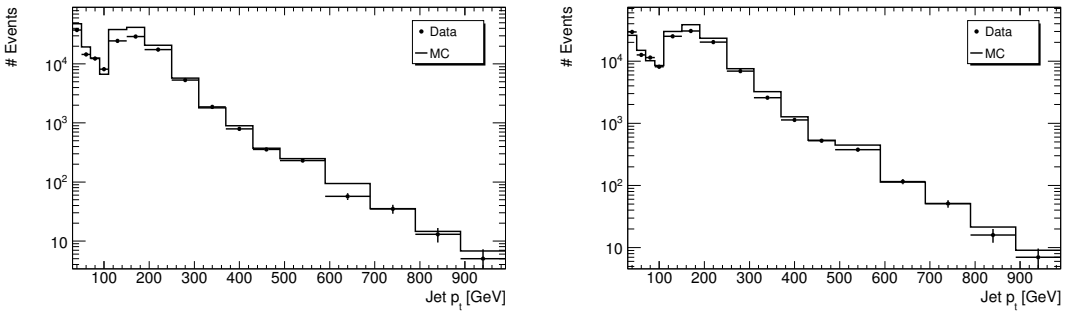

Figure 6.7: The jet p_{T} distribution for data and Monte Carlo after the b-tagging procedure, using the SV0 (left) and JetFitter (right) algorithms.

The reduction, followed by a subsequent rise, in the number of jets seen at relatively low p_{T} in these distributions is a result of the different p_{T}-spectra of the leading jet and non-leading jet contributions. The number of non-leading jets in events that possess relatively high p_{T} is significantly less than the number of leading jets with these momenta in the same events. As the leading jet requirement is set at 130 GeV it is only the non-leading jet contribution that populates the low p_{T} region whilst the leading jet contribution dominates in the higher region.

The ratios between the data and Monte Carlo across the p_{T} range are taken, both before and after b-tagging. Then, to ascertain whether there is any possible bias introduced during the b-tagging procedure, the double ratio (R_D) of these initial ratios, defined in equation 6.7, is used to study the change in the discrepancy between data and Monte Carlo before b-tagging and the discrepancy afterwards.

$$R_D = \frac{\mathrm{Data}_{before}/\mathrm{MC}_{before}}{\mathrm{Data}_{after}/\mathrm{MC}_{after}}. \tag{6.7}$$

These double ratios are shown in figure 6.8 for both the SV0 and JetFitter algorithms. The systematic uncertainty on the b-tagging calibration scale factors is propagated through to the Monte Carlo predictions by increasing/decreasing the scale factor values by their systematic uncertainties, as described above.

The fraction of the total number of jets present that are tagged as b-jets by each algorithm is shown in figure 6.9. A possible run period dependence of the b-tagging efficiency, for each of the tagging algorithms used, can also be studied in this case. For this the data shown in figure 6.9 is displayed in groups of data periods organised in chronological order ('B' being the earliest and 'K' being the latest) in terms of the time the data were recorded.

The fraction of jets tagged as b-jets in both data and Monte Carlo rises in value in the region below approximately 100 GeV, falls between 100 and 300 GeV before levelling off above 300 GeV, the b-tag fraction is seen to remain consistent

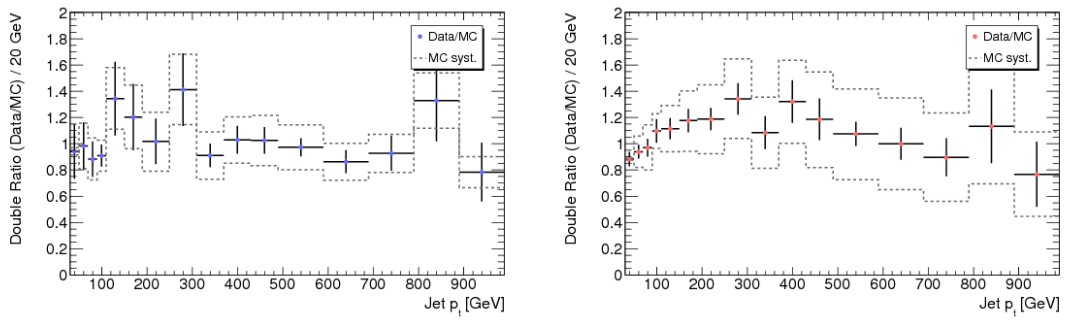

Figure 6.8: The Double Ratio of data to MC before and after the b-tagging compared to systematic uncertainty band from the b-tagging efficiency in the Monte Carlo, for SV0 (left) and JetFitter (right).

above the low p_{T} region in each of the separate analysis channels. The behaviour of each period of data is consistent across the entire p_{T} region in each channel and so no significant run period dependence is observed and the b-jet fraction in Monte Carlo is also in good agreement within the propagated systematic uncertainty.

To observe the dependence on the missing energy in an event of both the double ratio and the b-tag fraction, these quantities are compared in the case of different minimum required values of missing energy[3]. This comparison is carried out at intervals with 10 GeV steps between 50 GeV and the nominal threshold requirement in the analysis of 130 GeV. The weighted-average value of each quantity over the full p_{T} region is taken at each missing energy interval and shown for the case of each tagging algorithm in figure 6.10 as a function of the missing energy threshold in each case. The same procedure is carried out for the weighted average of the fraction of b-jets tagged and the results shown in figure 6.10.

The average value of the Double Ratio, representing the change in the level of agreement between data and Monte Carlo due to the b-tagging procedure, remains consistent across the missing energy threshold range and the systematic uncer-

[3]That is, increasing the missing energy requirement given originally in table 6.2.

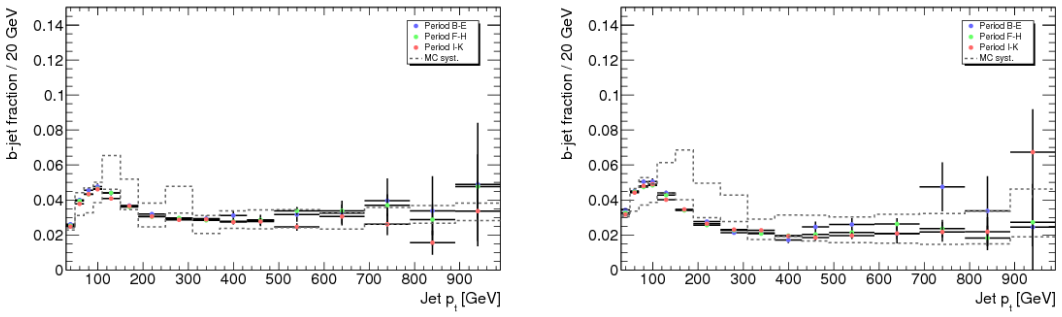

Figure 6.9: The fraction of all jets tagged as b-jets by the SV0 (left) and JetFitter (right) algorithms compared to the systematic uncertainty band in Monte Carlo on the same measurement.

tainty propagated to the analysis using the procedure described in section 6.2 remains consisted with unity for all thresholds applied. The average b-jet fraction remains approximately constant across the same range in the data. The Monte Carlo predicts an increase from 3% to approximately 4% for both tagging algorithms, which is the source of the observed bias in the double ratio in this channel and is likely due to limited Monte Carlo statistics.

Both the SV0 and JetFitter algorithms can be used in supersymmetry searches and they are understood here at the level of the systematic uncertainties assigned. The JetFitter algorithm is chosen for this analysis as this level of performance is seen with a b-tagging efficiency of 60% in comparison to an efficiency of 50% for SV0, with a comparable light jet rejection.

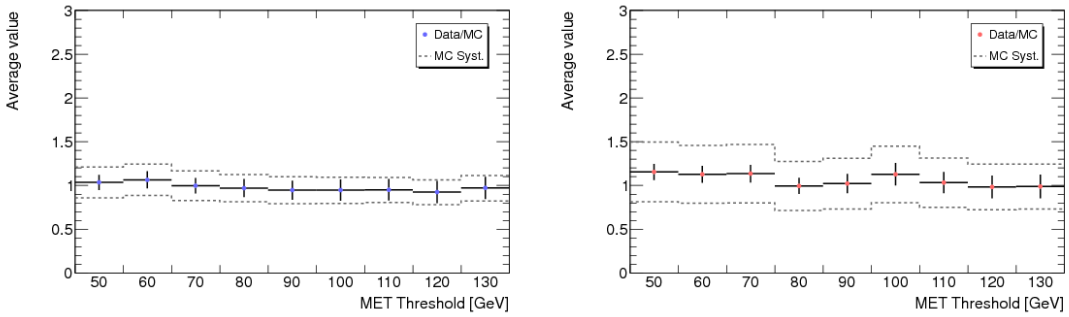

Figure 6.10: The weighted-average value of the Double Ratio for SV0 (left) and JetFitter (right), shown for nine values of the $E_{\mathrm{T}}^{\mathrm{miss}}$ cut threshold between 50 and 130 GeV.

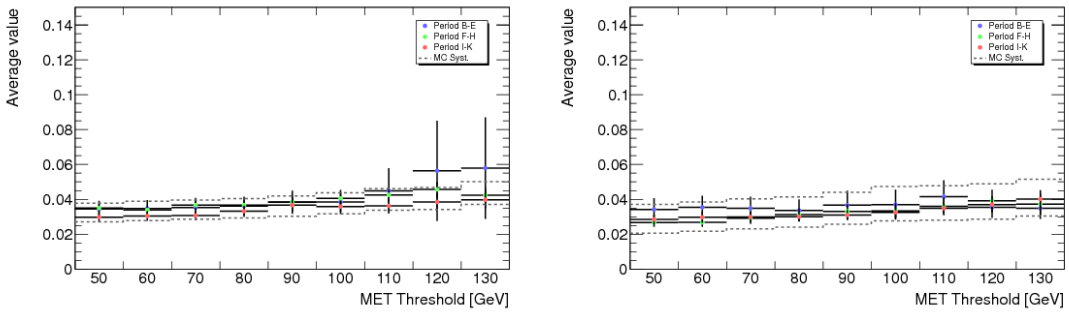

Figure 6.11: The weighted-average value of the b-tag fraction from using SV0 (left) and JetFitter (right), shown for nine values of the $E_{\mathrm{T}}^{\mathrm{miss}}$ cut threshold between 50 and 130 GeV.

Chapter 7

Gluino Mediated Sbottom Production

In this chapter a general search for the gluino mediated production of supersymmetric $s$bottom quarks in 2.05 fb^{-1} of $\sqrt{s} = 7$ TeV ATLAS data is described. The Standard Model backgrounds simulated with Monte Carlo and the SUSY signal processes that are simulated for different gluino and $s$bottom mass points are explained.

The process involved in filtering promising events that show properties that those of the signal process would be expected to have is described. The methods of estimating an accurate contribution from the different Standard Model processes are also described and the simulation is compared to the data in order to distinguish any potential signs of the signal process taking place.

7.1 Introduction

As outlined previously in section 2.4.2, the specific channel considered here is one involving the production of a pair of gluinos in the initial interaction, with at least one of the gluinos decaying to a $s$bottom quark and an ordinary bottom quark, shown in equation 7.1, followed subsequently by the $s$bottom quark decaying

to a bottom quark and, given the R-parity conserving model considered in this analysis, the lightest super-symmetric particle (LSP), shown in equation 7.2.

$$\widetilde{g} \rightarrow \widetilde{b} + b, \tag{7.1}$$

$$\widetilde{b} \rightarrow b + \chi_1^0. \tag{7.2}$$

The process of the gluinos decaying to the LSP accompanied by multiple other standard model particles may occur in this way or via a route involving a greater number of intermediate steps depending upon which decay modes are followed. This means that, through the decay of the second gluino, multiple high p_{T} jets, originating from each subsequent particle decay, may be produced by this original process.

In this analysis the LSP is assumed to be the lightest neutralino (χ_1^0), with a mass $\mathrm{m}_{\chi_1^0} = 60$ GeV. Previous results have excluded masses lighter than this if the LSP is the lightest neutralino [42]. The bottom quarks created from these processes will be observed in the detector in the form of their resultant b-jets and the neutralino will escape direct detection and manifest itself in the detector as missing energy ($E_{\mathrm{T}}^{\mathrm{miss}}$).

The result is that this process will be characterised by final states in the detector with at least one high transverse momentum b-jet, multiple high p_{T} secondary jets, large $E_{\mathrm{T}}^{\mathrm{miss}}$ and no leptons present. This analysis channel is thus referred to as the *zero lepton* channel, to distinguish itself from the case where either of the initial gluino decays produces a stop quark in place of one of the sbottom quarks and hence subsequently produces a lepton in the final state from the resultant top quark decay, referred to as the *one lepton* channel. No leptons are allowed to be present in potential signal events considered in this analysis to ensure consideration of potential sbottom quark production processes only.

7.2 Monte Carlo Simulation

In this section the Monte Carlo simulation samples that are used in this analysis are described. These Monte Carlo samples are produced using the ATLAS MC10b parameters [43] and utilised the full ATLAS Geant4 software [44]. The Monte Carlo simulated events are reconstructed using the same procedure and software framework as the real data.

The Monte Carlo simulations used in this analysis fall into two primary categories. The first are the simulations of the known Standard Model processes expected to occur in the data collectively referred to as the *background* to the search. The second are the various simulations, using different input parameters, of the predicted supersymmetric process, described previously, which is the focus of this search. These two categories of Monte Carlo simulation are described in the following sections.

7.2.1 Standard Model Processes

The purpose of analysing Monte Carlo simulations of the known Standard Model processes, in parallel to the data, is in order to allow a comparison of all the results observed in that data with those that the Standard Model predicts should be observed if there are no other unknown processes contributing to what is being seen.

Table 7.1 shows the different Standard Model background processes considered along with the cross-section times the branching ratio and the generator used. Whether the cross-section is calculated to Leading Order (LO), Next-to-Leading Order (NLO) or Next-to-Next-to-Leading Order (NNLO) is also shown. The tables in Appendix A.2 additionally show all of the individual Monte Carlo samples used in this analysis. There are four main categories of Standard Model background considered: QCD, W/Z Boson + jets, top (both single top and pair produced) and Di-Boson backgrounds.

Production Process	Cross-section [nb] × BR	Generator
QCD (Di-jet)	10.47×10^6 (LO)	Pythia, Alpgen
W $\rightarrow \ell^+\nu$ + jets	31.40 (NNLO)	Alpgen, Herwig + Jimmy
Z $\rightarrow \ell^+\ell^-$ + jets	3.20 (NNLO)	Alpgen, Herwig + Jimmy
Z $\rightarrow \nu\overline{\nu}$ + jets	5.82 (NNLO)	Alpgen, Herwig + Jimmy
Di-Boson (WW, ZZ, WZ)	0.104 (NLO)	Herwig
$t\bar{t}$	0.164 (NLO + NLL)	MC@NLO, Herwig + Jimmy
$t\bar{t}$+$b\bar{b}$	0.9×10^{-3} (LO)	Alpgen, Herwig + Jimmy
$t\bar{t}$+W / Z	0.4×10^{-3} (LO)	Madgraph + Pythia
Single Top	0.037 (NLO + NLL)	MC@NLO, Herwig + Jimmy

Table 7.1: A list of the Monte Carlo simulated Standard Model background processes used in this analysis, their respective SUSY signal cross-sections multiplied by the branching ratio (BR) and the generators used to produce each of the samples. The ℓ represents all three lepton flavours (e, μ, τ).

The QCD di-jet events were generated using Pythia [45] and the cross-section used throughout is at Leading Order. In total 9 separate samples were used to represent the QCD processes (J0-J8), ordered by constituent di-jet p_{T}, the J0 sample containing the lowest and the J8 sample containing the highest p_{T} jets.

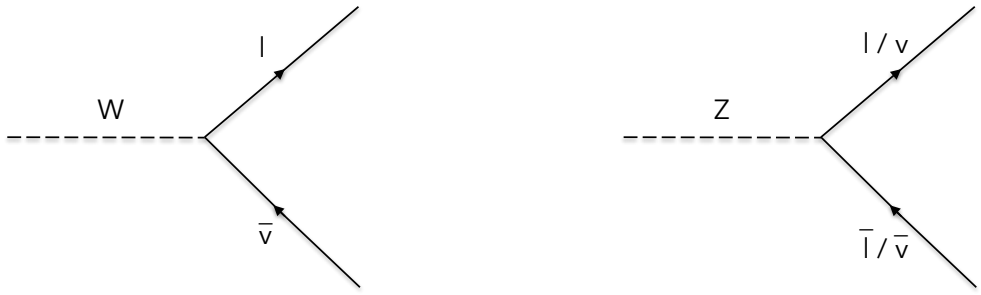

Figure 7.1: A W boson decaying into a charged lepton and a neutrino (left) and a Z boson decaying into a lepton/anti-lepton pair (right).

The W/Z + jets events, weak boson decay processes shown in figure 7.1, were generated using Alpgen interfaced to Jimmy [46], the cross-sections used are at the NNLO level. The W/Z contribution to the background also includes contributions from W$b\bar{b}$, W$c\bar{c}$ and Z$b\bar{b}$ also generated by Alpgen.

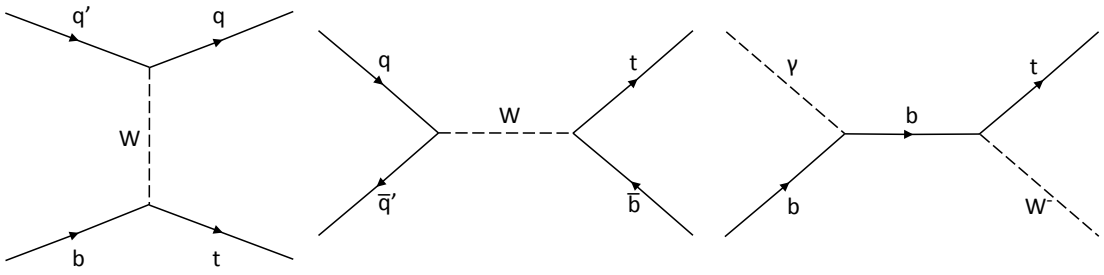

Figure 7.2: The Single Top background, t-channel (left), s-channel (centre) and Wt (right) production processes.

The top quark events were generated with the MC@NLO software [47], the cross-sections used are at the NLO level and a top quark mass of 172.5 GeV is assumed. The top background contribution includes both top pair production and single top production processes and these were represented with separate samples.

The three distinct single top processes simulated are shown in figure 7.2. The t-channel process on the left illustrates a light flavour quark and a b-quark interacting via the exchange of a W boson producing a different light flavour quark and a top quark. The s-channel process in the centre shows a quark-antiquark pair annihilating to produce a W boson producing a top quark and a b-quark. The 'Wt' process on the right shows a b-quark absorbing a photon and subsequently radiating a W boson and producing a top quark.

The top quark produced in all of these scenarios subsequently decays exclusively through the process in figure 7.3, by radiating a W boson and transforming into a b-quark, where the W boson decays either to a charged lepton and a neu-

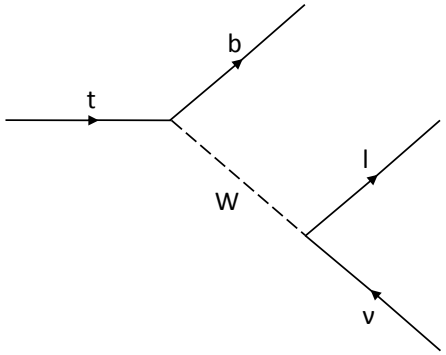

Figure 7.3: Top quark decay into a W boson and a b-quark, the W boson subsequently decaying into a charged lepton and a neutrino.

trino or to hadrons. In the former case, the charged lepton, missing energy from the neutrino and the jet produced by the b-quark are then observed. In the latter case the same missing energy and jet from the b-quark are observed along with two additional hadronic jets.

7.2.2 The SUSY Signal Process

Whereas the Standard Model Monte Carlo is used to represent the background to this search, the simulations of the predicted supersymmetric process form a view of the potential signal. The repeated simulation of this signal process using different parameters, such as the masses of the supersymmetric particles involved, allows a view of how the signal might look in the data in each of these scenarios.

The Monte Carlo samples that were used to model the different predicted signal processes in this analysis are presented in a grid format where each individual sample is equivalent to one point on the grid with axes of the sbottom ($m_{\tilde{b}}$) and gluino ($m_{\tilde{g}}$) masses on the x- and y-axes respectively, therefore each sample represents processes occurring with different theoretical gluino-sbottom

SUSY Model	Generator	Main Parameters	Main Processes	No. Samples
Pheno MSSM 1	Herwig, SUSYHIT	$m_{\tilde{g}}$, $m_{\tilde{b}}$ $m_{\widetilde{\chi}_1^0} = 60$ GeV	$\tilde{g} \rightarrow \tilde{b} + b$ $\tilde{b} \rightarrow b + \widetilde{\chi}_1^0$	38
Pheno MSSM 1H	Herwig, SUSYHIT	$m_{\tilde{g}}$, $m_{\tilde{b}}$ $m_{\widetilde{\chi}_1^0} = 60$ GeV	$\tilde{g} \rightarrow \tilde{b} + b$ $\tilde{b} \rightarrow b + \widetilde{\chi}_1^0$	49

Table 7.2: A summary of the simulated SUSY samples and processes used in this analysis, the generators used to produce each of the samples, the main processes represented and the total number of samples of each kind.

mass combinations. The table in 7.2 shows the different signal processes considered for each grid of points, along with the generator used, the values of the main parameters and the total number of samples in the grid. The tables in Appendix A.1 additionally show all of the individual signal Monte Carlo samples used in this analysis.

All the samples were generated using Herwig++ [48] and the branching ratios were calculated per gluino-sbottom mass combination using the SUSYHIT tool [49]. The theoretically predicted cross-sections used were calculated using PROSPINO [50] and are accurate to the Next-to-Leading Order (NLO) level.

The two sets of grid points in table 7.2 are complementary to each other as they share the same characteristics, the second set purely serves to extend the reach of the first set in the gluino-sbottom mass plane, with this set having samples simulated with higher masses. This grid is configured to allow a comparison with previous results obtained from the Tevatron and to extend them in the gluino-sbottom mass plane. A total of 87 points were used to form this grid (38 in the first set and 49 in the second set) and they represent a gluino mass ranging from 360 GeV to 1 TeV and a sbottom mass ranging from 240 GeV to 880 GeV. The Tevatron excludes a sbottom quark mass below 250 GeV [51]. The other parameters set for all mass points in the simulation of this grid are listed below.

- The mass range of the first and the second generation of *s*quarks is set to

be equal to $m_{squarks} = 5$ TeV.

- The slepton mass range is set to be greater than $m_{slepton} > 1$ TeV.
- The mass of the stop is assumed to be much greater than the mass of the gluino, $m_{stop} >> m_{gluino}$.
- The chargino mass is $m_{chargino} = 700$ GeV.
- The lightest supersymmetric particle mass is $m_{\chi_1^0} = 60$ GeV.

7.3 The Event Selection

The total set of events present in each MC sample and each dataset are passed through a series of selection requirements. These requirements are applied to each event on the properties of the objects and defined quantities described in chapter 5. This is done firstly to filter out unusable and bad quality events, where the criteria are designed to reduce the background stemming from detector noise and processes originating from non-collision sources. After which, with samples optimised to contain only good quality collision induced events, further selection requirements are applied in order to attempt to reduce the number of events stemming from possible Standard Model background (non-signal) processes, whilst retaining as many of the events as possible that may have come from the signal process.

This set of distinct requirements are applied in a sequential order, at which point the surviving events are tested against the criteria of six separate signal regions defined in section 7.5. Only events that fail to pass *any* of these criteria are discarded. These last six selections are the six separate signal regions of this analysis and the events which separately pass any of these selections are the candidate events for the signal process.

The full list along with a description of each of the selections in the order they are applied in this analysis is shown bellow:

- **Data Quality -** Events are initially selected by requiring that they must be from a run, and a luminosity block within this run, that is specified as being *good* in the 2011 data "Good Run List" prescribed by the ATLAS SUSY Working Group. This list rejects the *bad* data that were taken during a period when there was a known problem with one or more parts of the detector. (Only applicable for Data. All MC events automatically pass this requirement).

- **Trigger -** The event must pass the trigger selection, here using a combined jet + Missing E_{T} trigger with jet $p_{\mathrm{T}} > 75$ GeV and Missing $E_{\mathrm{T}} > 45$ GeV thresholds at the event filter level.

- **LAr Error -** For approximately 40% of the total data sample one region of the Liquid Argon (LAr) Calorimeter was not functioning correctly. The (previously) generated MC does not take this problematic region into account and so any events with at least one jet with a p_{T} above 50 GeV in this η/ϕ region of the detector are discarded.

- **Overlap Removal -** The removal of overlapping objects (jets, electrons and muons) from within an event is performed following the procedure described in section 5.2, but no events themselves are removed at this stage.

- **Bad Jet cleaning -** Events are removed that contain one or more fake or poorly measured jets.

- **Primary Vertex Requirement -** There must be at least one primary vertex having a minimum of 5 tracks associated with it in the event.

- **Electron Veto -** Events containing at least one Electron with a $p_{\mathrm{T}} > 20$ GeV are rejected.

- **Muon Veto -** Events containing at least one Muon with a $p_{\mathrm{T}} > 10$ GeV are rejected.

- **Leading Jet -** The leading jet in the event must have a $p_{\mathrm{T}} > 130$ GeV.
- **Additional jets -** The event must, in addition, contain at least two further jets with $p_{\mathrm{T}} > 50$ GeV.
- **Missing Energy -** The Missing E_{T}, defined in section 5.3.1, in the event is required to be greater than 130 GeV.
- **Missing Energy / Effective Mass Ratio -** The ratio of the Missing E_{T} to the Effective Mass (defined in section 5.3.2) in the event is required to be greater than 0.25.
- ***b*-jets-** At least one of the jets with a $p_{\mathrm{T}} > 50$ GeV must be a b-tagged jet (the procedure for which is explained in section 5.1.3).
- **Jet / Missing E_{T} Separation -** The first three leading jets in the event must be separated from the Missing E_{T} by $\Delta\phi > 0.4$ radians.
- **Effective Mass / Number of *b*-tags (Signal Regions) -** Six different requirements are made in parallel. The Effective Mass, defined in section 5.3.2, is required to be greater than 500 GeV, 700 GeV, 900 GeV for events that have at least one b-tag (Signal Regions 1, 2 & 3 respectively) and similarly required to be greater than 500 GeV, 700 GeV, 900 GeV for events that have at least two b-tags (Signal Regions 4, 5 & 6 respectively).

The initial requirement placed on all data events is one of ensuring that they were recorded at a time when the ATLAS detector was operating in optimum condition. This means that all events utilised for the analysis from this point forward are deemed to be of good quality and the process through which the final judgement on this quality is made was described in detail in chapter 4. This requirement is not applicable to the Monte Carlo simulated events as their reconstruction is independent of real detector performance.

Not all of the events seen by the detector can be recorded and subsequently stored and only some of those that are stored have signatures relevant to this analysis. For this reason a trigger is applied to the full data sample which, as there are no leptons required in this search, acts on the p_{T} of jets and the missing energy in events. This trigger is seeded by requiring a jet $p_{\mathrm{T}} \geq 55$ GeV and missing energy of 20 GeV from the level 1 trigger information and further requiring jet $p_{\mathrm{T}} \geq 70$ GeV from level 2 trigger information. At the event filter level, this trigger requires that at least one jet in the event has a p_{T} of at least 75 GeV and that there is a missing energy of at least 45 GeV. This reduces the number of events to be considered for the rest of the selection process to only those which satisfy these specific criteria.

The selection criteria are largely driven by the trigger requirements as the plateau of the trigger efficiency turn on curve for the particular trigger used starts at a leading jet p_{T} of 130 GeV. This value is used as the threshold in the analysis selection in order to avoid a systematic uncertainty coming from the trigger efficiency off the plateau being poorly matched in the Monte Carlo simulation. The efficiency of the trigger used also rises with the $E_{\mathrm{T}}^{\mathrm{miss}}$ threshold applied with an optimum value of 130 GeV. The p_{T} thresholds of the lepton vetoes are set at 20 GeV for electrons and 10 GeV for muons as these are the thresholds required for successfully and accurately reconstructing these leptons in the detector.

An illustration of the separation between the three leading jets and the missing transverse energy in an event is shown in figure 7.4. The angular separation between the closest of these jets and the missing energy, $\Delta\phi_{min}$, is used as a discriminating factor to reduce the QCD contribution to the background. A value of 0.4 radians for this separation between the missing transverse energy and the nearest of the leading 3 jets is motivated by the threshold at which the Standard Model QCD process ceases to dominate the results as is illustrated on the left in figure 7.5 in the following section.

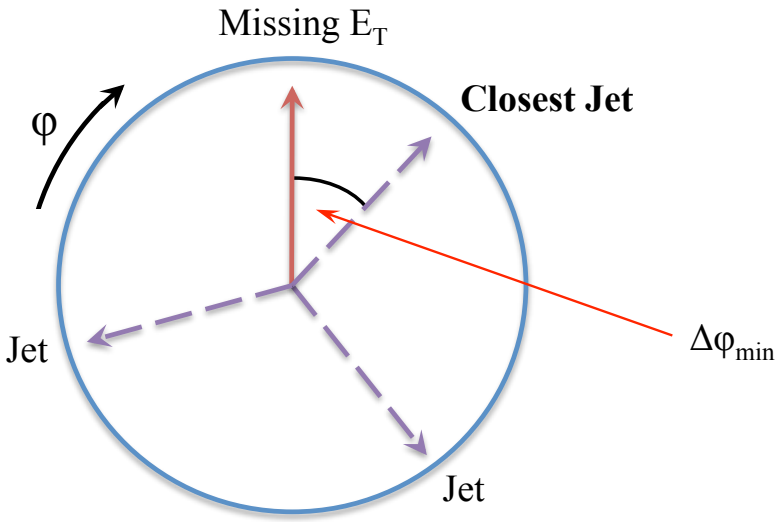

Figure 7.4: Schematic of the separation between the three leading jets and the missing transverse energy in an event and the quantity $\Delta\phi_{min}$.

7.4 Background Estimation

After the definition of the signal search regions and the propagation of events through to them it is seen from Monte Carlo simulation predictions that Standard Model processes are still expected to be present in the data which survives into these regions. The primary processes contributing to this background are QCD, W/Z boson + jets and top (both single and pair production). The Di-Boson, W/Z with associated quark production and non-collision processes contributions are found to be negligible. From the remaining contributions, the largest by far is from top pair production, so extra care must be taken when calculating this background, the estimation procedure for which is described in section 7.4.2.

Given the overall number of events initially present in the QCD MC samples and that the probability of these events passing the hard $E_{\mathrm{T}}^{\mathrm{miss}}$ and $\Delta\phi_{min}$ requirements is extremely small, only relatively few raw events from the samples survive into the signal region before they are normalised to the total integrated

luminosity. This fact, combined with the relatively large cross-section of these processes, makes the estimation of their contribution at this stage of the analysis more difficult and so a procedure to account for this is described in the following section.

7.4.1 QCD Background Estimation

As so few of the QCD events survive as a proportion of the overall total number of simulated events, then to obtain statistically significant results from purely taking the number of events that survive the cuts would require impractically large MC samples. In place of this the jet response smearing method, described in detail in [52], is used to estimate this contribution.

This is a data driven method, where a QCD enriched control region is constructed and selected data events with minimal missing energy, which make it into this control region, are modified by smearing the p_{T} of the jets in these events to produce simulated missing energy. These events are then taken, as a sample of QCD MC pseudo-events, and propagated to the signal regions using the same selection criteria as the ordinary data. The proportion of these pseudo-events that survive into each signal region are then normalised to the standard control region QCD sample to give an estimate of the contribution that this QCD sample will produce in the signal region.

The control region is defined by retaining all the selection criteria up until the $\Delta\phi_{min}$ requirement, whose primary function is to *reduce* the QCD contribution, and then reverse it. So in place of a requirement that all events have a minimum separation between the missing energy and the nearest jet to it in the transverse plane of greater than 0.4 radians, the control region contains all those events at this stage of the selection that have a jet *less* than 0.4 radians from the missing energy in that event in the transverse plane. As shown in figure 7.5, the minimum

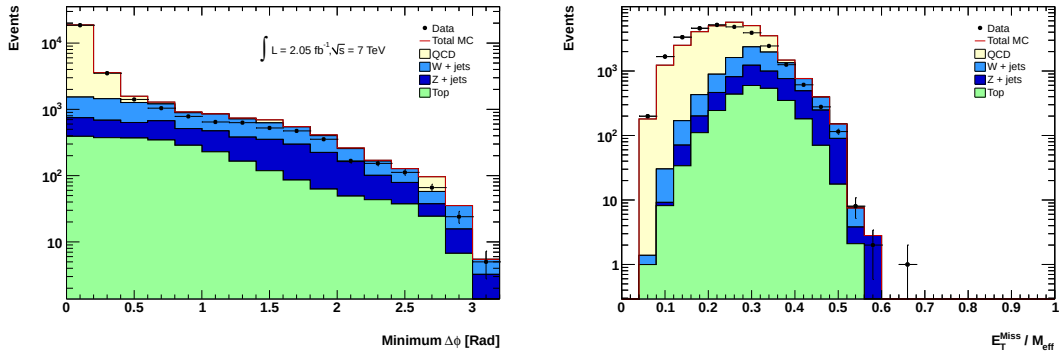

Figure 7.5: The $\Delta\phi_{min}$ (left) and $E_{\mathrm{T}}^{\mathrm{miss}}/M_{eff}$ (right) for events with leading jet p_{T} $>$ 130 GeV, at least 3 jets in total with p_{T} $>$ 50 GeV and $E_{\mathrm{T}}^{\mathrm{miss}}$$>$ 130 GeV.

separation between the missing energy and the closest jet and the ratio of this missing energy to effective mass are the best discriminators between QCD and non-QCD Standard Model backgrounds when an appropriate cut threshold is applied. Placing this threshold on the $\Delta\phi_{min}$ quantity ensures that a sample of events dominated by the QCD contribution can be utilised for the purpose of applying the method outlined above.

7.4.2 Non-QCD Background Estimation

For the remainder of the Standard Model background, the W and Z Boson contributions are both taken directly from the MC prediction, but the top involves a further step.

The single top and top pair production processes if taken directly from the MC simulation have relatively large systematic uncertainties. In order to reduce these systematic uncertainties a separate one-lepton control region is defined, in this case retaining the same selection requirements described above and reversing the lepton vetoes to require one electron or muon in an event and requiring at least one b-tagged jet. The top processes' contribution to the signal region composition is estimated from the the MC prediction in this top dominated control region by

the following

$$N_{SR} = T_f \cdot N_{CR}^{Data}, \tag{7.3}$$

where N_{SR} is the number of top events calculated for the signal region, N_{CR}^{Data} is the number of events observed in the top control region. This value is corrected for the MC prediction of the non-top (primarily W and Z boson) presence in this region to give the predicted, purely top, value. T_f is known as the Transfer Function and is defined as

$$T_f = \frac{N_{SR}^{MC}}{N_{CR}^{MC}}, \tag{7.4}$$

where N_{SR}^{MC} is the number of events in the signal region predicted by the MC simulation and N_{CR}^{MC} the number predicted in the control region. The result of calculating the top contribution in this way is that the contributions to the systematic uncertainty that are correlated in both the observed and simulated processes effectively cancel out.

7.5 The Signal Regions

After all selection criteria have been applied the surviving events are categorised into six different signal regions. These separate signal regions are set up due to the fact that, as illustrated in figure 7.6, there is some evidence of a dependence of the effective mass spectrum on the mass difference between the gluinos produced in the initial interaction and the neutralino which eventually results. The result of this possibility is that each signal region, based on a different threshold value for the effective mass observed in events, is sensitive to a different region of the gluino-sbottom mass plane.

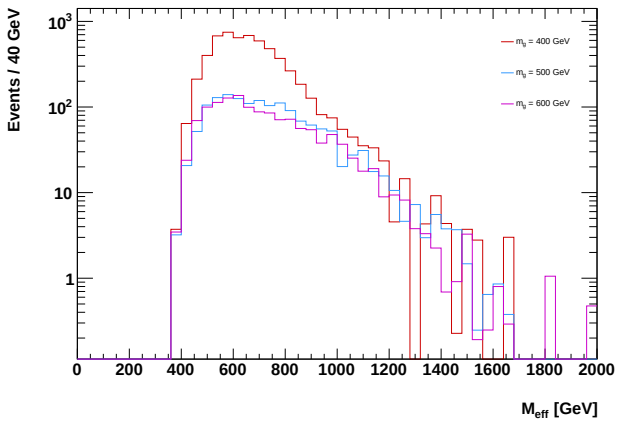

Figure 7.6: Effective mass in the signal process for various gluino-neutralino mass differences, with a neutralino mass of $m_{\chi_1^0} = 60$ GeV.

The six signal regions defined for this purpose, as introduced in section 7.3, are

- **Region 1a -** At least 1 b-jet and an Effective mass of $M_{eff} \geq 500$ GeV.
- **Region 1b -** At least 1 b-jet and an Effective mass of $M_{eff} \geq 700$ GeV.
- **Region 1c -** At least 1 b-jet and an Effective mass of $M_{eff} \geq 900$ GeV.
- **Region 2a -** At least 2 b-jets and an Effective mass of $M_{eff} \geq 500$ GeV.
- **Region 2b -** At least 2 b-jets and an Effective mass of $M_{eff} \geq 700$ GeV.
- **Region 2c -** At least 2 b-jets and an Effective mass of $M_{eff} \geq 900$ GeV.

These signal regions are therefore complementary and the search can be carried out in parallel in each of them.

7.6 Systematic Uncertainties on the Background

There is an inherent uncertainty associated with the predicted event yields provided by the simulation of the standard model background processes. The various contributions to this uncertainty on the background that are shared in common between all the background processes considered are described below. The contributions to the systematic uncertainty from other sources including the trigger efficiency and lepton identification are negligible and are not included here.

7.6.1 Jet Energy Scale (JES)

The Jet Energy Scale (JES) uncertainty is dependent on four factors, the p_{T} and $|\eta|$ of a given jet, the ΔR between a given jet and its closest neighbouring jet and the average quark-gluon composition of the jet. This uncertainty is propagated to the analysis through a provision described in [53]. The total transverse energy of the jet is then scaled up and down by the 1σ uncertainty obtained with this method and the $E_{\mathrm{T}}^{\mathrm{miss}}$ is re-computed using this new energy scale,

$$\mathbf{E}_{\mathrm{T}}^{\mathrm{miss(up,down)}} = \mathbf{E}_{\mathrm{T}}^{\mathrm{miss}} + \sum_{\mathrm{j}} \mathbf{p}_{\mathrm{T}j} + \sum_{\mathrm{j}} \mathbf{p}_{\mathrm{T}j}^{\mathrm{(up,down)}}, \tag{7.5}$$

where (up,down) signifies the 1σ shift up and shift down re-scaled jet momenta and resultant $E_{\mathrm{T}}^{\mathrm{miss}}$ calculation.

7.6.2 b-tagging Efficiency

The systematic uncertainties on the efficiency of the b-tagging algorithms manifest themselves in altering the shape of the simulated $p_{\mathrm{T}}^{\mathrm{rel}}$ templates that are used to fit the relative p_{T} of muons originating from heavy flavour decay in b-jets to data. These uncertainties are therefore determined by repeating the procedure of fitting to the data with modified versions of the templates.

This same uncertainty also affects the scale factors that are used to determine the weighting given to each MC event and individual jet within an event in the analysis as these scale factors are defined as the ratio of the efficiency observed in MC to that in data. The final contribution of the b-tagging procedure to the total systematic uncertainty is estimated by carrying out the analysis on the MC whilst applying a $\pm 1\sigma$ variation on the applied scale factors.

The b-tagging procedure in this analysis and in particular the treatment of the systematic uncertainty on the b-tagging procedure is described in greater detail in chapter 6.

7.6.3 Luminosity

The method of calibrating the ATLAS luminosity scale is based on using dedicated *van der Meer* scans (also called *luminosity* scans) of the condition of the proton beams [54]. The luminosity of a proton-proton collider consisting of bunches of protons in its beams can be expressed as

$$\mathcal{L} = \frac{\mu n_b f_r}{\sigma_{inel}}, \tag{7.6}$$

where μ is the average number of interactions per bunch crossing, n_b is the number of bunches, f_r is cyclical frequency of the beams and σ_{inel} is the inelastic cross-section of proton-proton interaction. ATLAS monitors the luminosity delivered by the LHC beams by carrying out a measurement on the observed number of interactions per bunch crossing μ_{obs} independently using different dedicated detectors and algorithms. The total luminosity can then be expressed as

$$\mathcal{L} = \frac{\mu_{obs} n_b f_r}{\sigma_{obs}}, \tag{7.7}$$

where $\sigma_{obs} = \epsilon\sigma_{inel}$ is the total inelastic cross-section multiplied by the efficiency ϵ of a particular detector and algorithm.

$$\mathcal{L} = \frac{n_b f_r n_1 n_2}{2\pi\Sigma_x\Sigma_y}. \tag{7.8}$$

The dominant contribution to the luminosity uncertainty comes from three separate sources. Firstly from the van der Meer scan calibration, and to this the determination of the bunch charge product contribution (number of protons measured by total electric charge in a bunch) is the dominant contributor. Secondly the long term consistency of the measurement by a given luminosity detector of the average σ_{obs} over time. And lastly the dependence of the algorithm used to the average number of interactions observed in a bunch crossing. From these three primary sources the contribution from the van der Meer scan uncertainty is the dominant one. Combining all sub-contributions an uncertainty of 3.7% is ascribed to the value of the total integrated luminosity used, as described in detail in [55].

7.6.4 Pileup

The MC events in the samples used in this analysis were simulated with an average number of interactions per bunch crossing, $\langle\mu\rangle_{MC}$, of 8. Whereas throughout the data taking period considered the average number of interactions increased in accordance with the rising instantaneous luminosity provided by the LHC over that same period. To account for this the MC events were re-weighted to match the observed behaviour in the data.

The Jet Energy Scale and b-tagging efficiency systematic uncertainties are the dominant contributions for all processes in each of the signal regions. The uncertainty relating to the b-tagging efficiency is of much greater significance in the signal regions requiring at least 2 b-jets than in those requiring at least 1 b-jet.

7.7 Comparison with Data

With these considerations made, the predictions for the background of the Monte Carlo simulations are compared to the observed results in data. The comparisons are made using 2.05 fb^{-1} of data and the results are shown in figures 7.7 to 7.13. The data-MC results are compared additionally across all six signal regions.

S.R	Top	QCD	W + jets	Z + jets	Total MC	Data
1a	705.4 ± 112.6	19.8 ± 9.5	218.9 ± 49.1	78.6 ± 19.3	**1022.8 ± 124.7**	**951**
1b	119.7 ± 26.7	8.4 ± 5.8	41.2 ± 13.4	16.0 ± 6.9	**185.4 ± 31.2**	**168**
1c	22.0 ± 8.2	0.01 ± 0.01	11.5 ± 8.7	2.0 ± 2.0	**35.5 ± 12.1**	**28**
2a	205.9 ± 52.3	11.8 ± 8.6	26.1 ± 10.1	3.4 ± 3.4	**247.1 ± 54.1**	**252**
2b	35.5 ± 13.8	8.3 ± 6.2	0.08 ± 0.08	3.3 ± 3.3	**47.3 ± 15.5**	**36**
2c	6.3 ± 3.9	0.0	0.0	0.9 ± 0.9	**7.2 ± 4.0**	**6**

Table 7.3: A summary of the event yield for all six signal regions showing the total events observed in data, the total predicted by the Monte Carlo and the break down of each standard model contribution. The total uncertainties associated with each prediction are also shown.

The summary of the event yield in each of the six individual signal regions is shown in table 7.3. Both the total number of events observed in the data and the Standard Model MC prediction are given and for the MC prediction the separate contributions from each of the background processes, along with their associated total uncertainties, are also given. The uncertainties on the Monte Carlo prediction are the total of both the combined systematic, discussed in the previous section, and statistical uncertainties.

Although an under-fluctuation of the data is observed in five of the six signal regions, the comparison with the Standard Model prediction is in good agreement to within the combined uncertainty across all regions. It can also be seen, that

with the 2.05 fb^{-1} of data studied, the total statistics obtained in the 1c and 2c ($M_{eff} > 900$ GeV) signal regions are extremely low, so in these regions the reach of this analysis is at its limit. This low level of statistics is visible in the figures that follow.

The top (combined single top and pair production) processes are the dominant Standard Model contribution across all six signal regions. This is to be expected due to the prominent top decay effectively guaranteeing the presence of high p_{T} b-quarks in these events. The W/Z boson + jets background are the next largest contributor and together these three sources of background make up over 95% of the Standard Model background observed.

Of the other backgrounds the Di-boson contribution is negligible and therefore omitted from the table in 7.3. The QCD processes are a very minor contribution to the overall Standard Model background across all signal regions, after being the primary source of background prior to the application of the main event selections of section 7.3. This is primarily due to the success of the cut threshold set on the $\Delta\phi$ gap between missing transverse energy and leading jets explained in section 7.4.1, along with the ratio of missing to visible transverse energy relative to other backgrounds, both of these distinguishing features are illustrated in figure 7.5 in section 7.4.1.

Signal Region Event Kinematics

Here the event kinematics are shown for those events that make it into at least on of the six signal regions. Figure 7.7 shows the number of jets above the threshold of $p_{\mathrm{T}} > 50$ GeV and the p_{T} of the leading jet in each event in signal region 1a. Figure 7.7 shows the same distributions for b-tagged jets in these events. It is observed that the top processes are the dominant contribution to the background and the W/Z boson + jets processes make a substantially smaller contribution, whilst the QCD processes are negligible. The data is in agreement with the total Standard Model MC background.

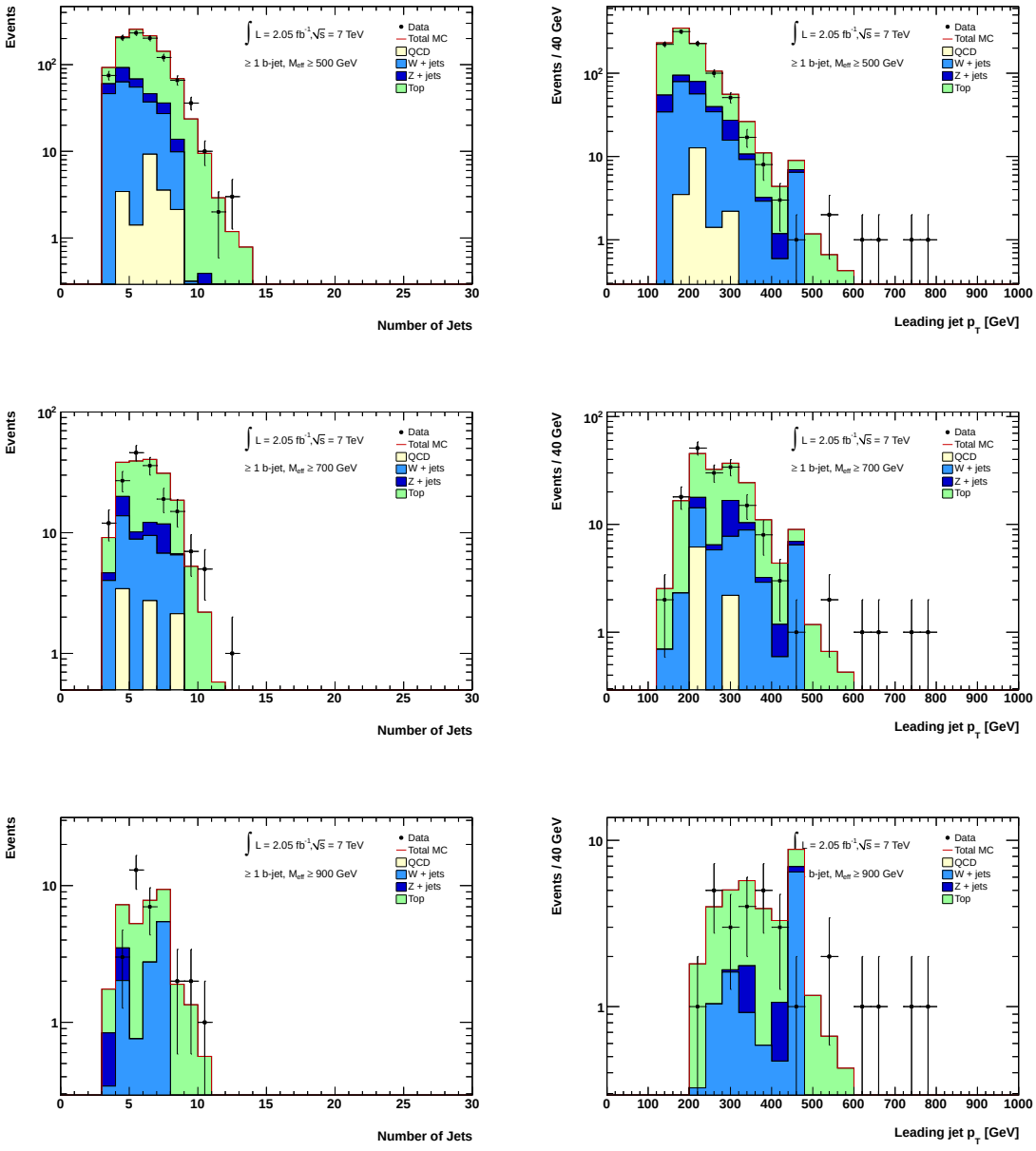

Figure 7.7: The number of jets per event with a $p_{\mathrm{T}} \geq 50$ GeV (left) and the p_{T} of the leading jet in each event (right) in the signal regions requiring at least 1 b-jet and $M_{eff} \geq 500$ GeV (top), 700 GeV (middle) and 900 GeV (bottom).

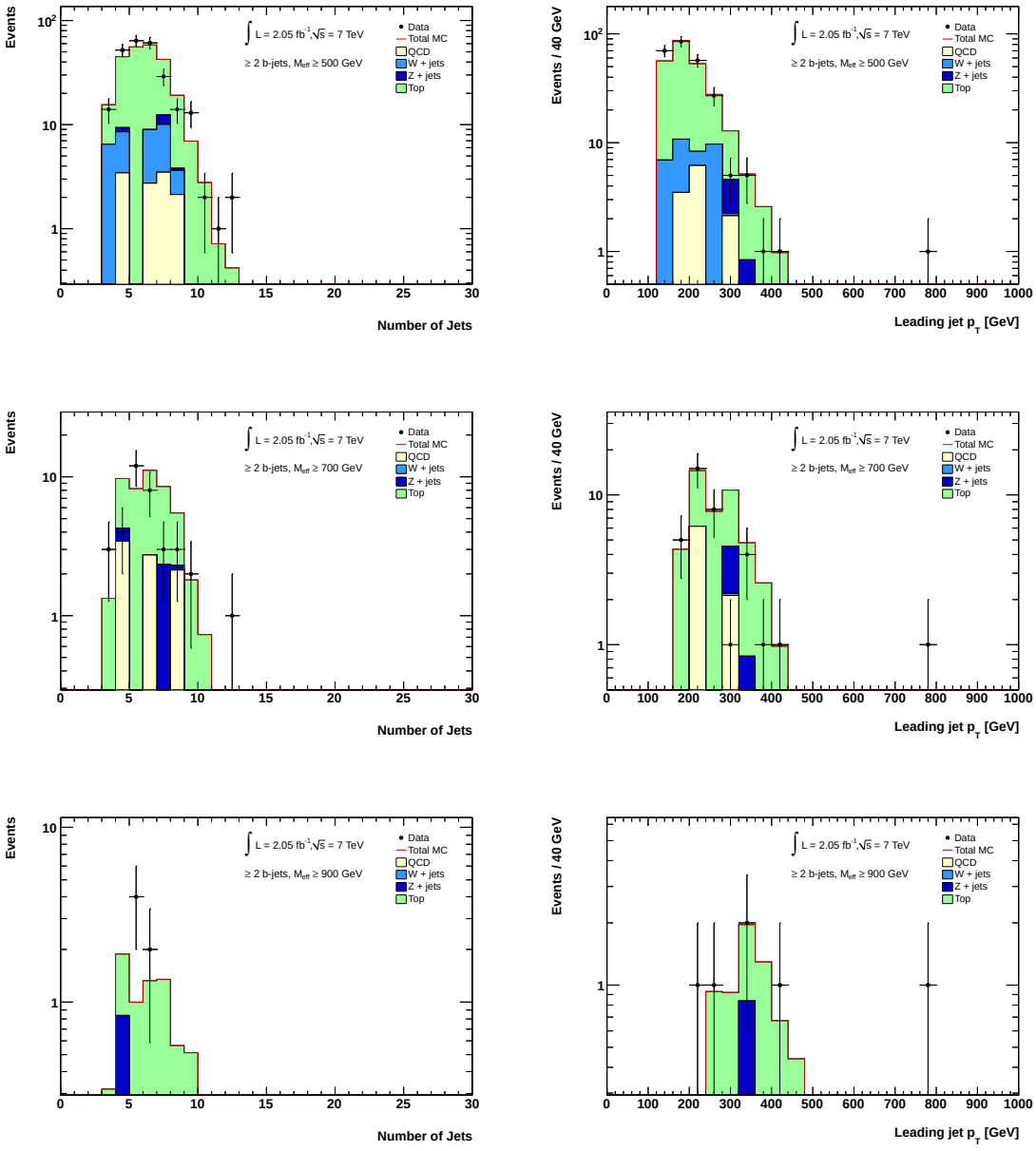

Figure 7.8: The number of jets per event with a $p_{\mathrm{T}} \geq 50$ GeV (left) and the p_{T} of the leading jet in each event (right) in the signal regions requiring at least 2 b-jets and $M_{eff} \geq 500$ GeV (top), 700 GeV (middle) and 900 GeV (bottom).

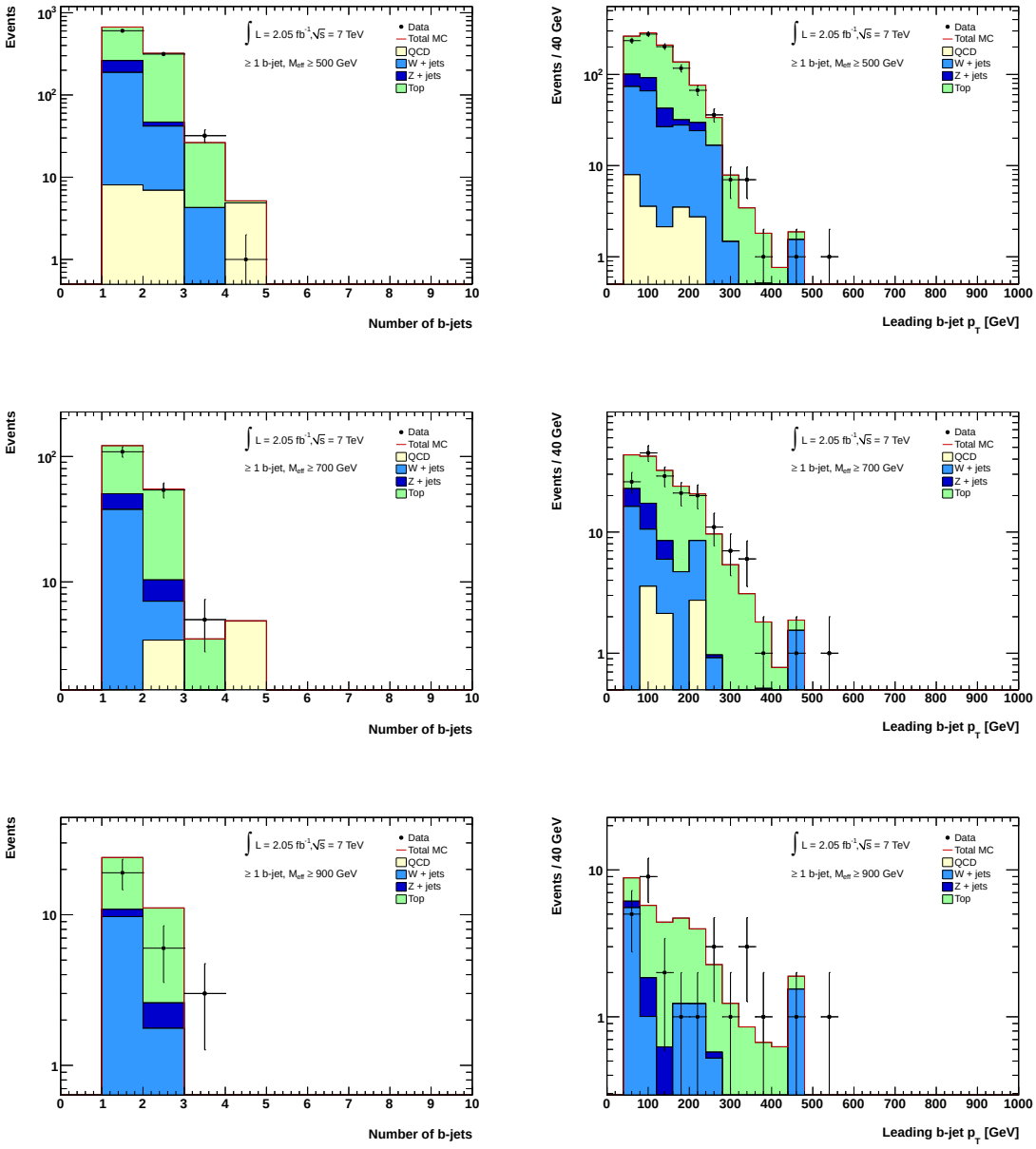

Figure 7.9: The number of b-jets per event with a $p_{\mathrm{T}} \geq 50$ GeV (left) and the p_{T} of the leading b-jet in each event (right) in the signal regions requiring at least 1 b-jet and $M_{eff} \geq 500$ GeV (top), 700 GeV (middle) and 900 GeV (bottom).

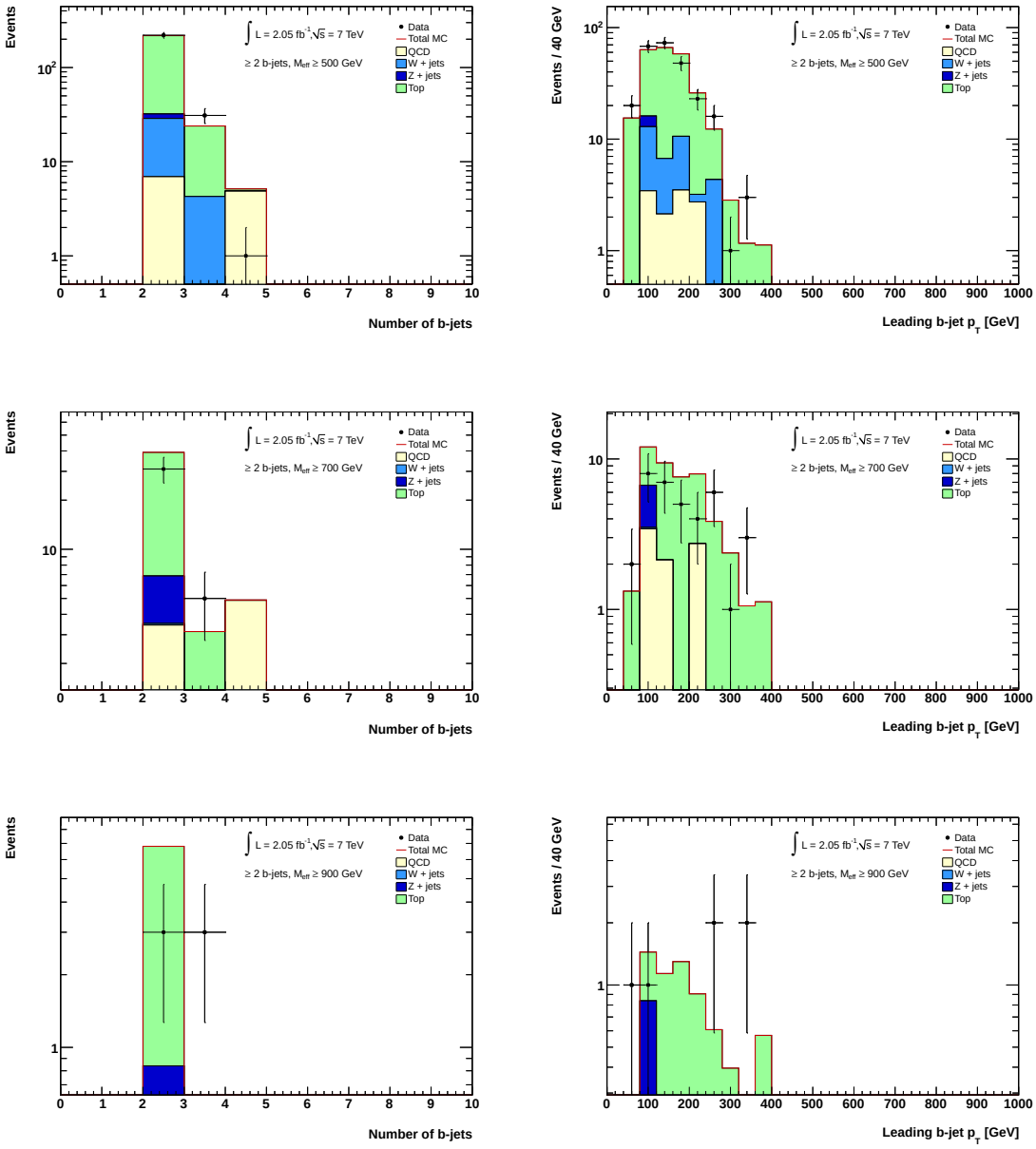

Figure 7.10: The number of b-jets per event with a $p_{\mathrm{T}} \geq 50$ GeV (left) and the p_{T} of the leading b-jet in each event (right) in the signal regions requiring at least 2 b-jets and $M_{eff} \geq 500$ GeV (top), 700 GeV (middle) and 900 GeV (bottom).

Signal Region Missing Energy

As significant amounts of missing transverse energy are expected in the final state of the signal process representing the non-detection of the neutralino, comparisons of this quantity between the MC prediction and that observed in data are of particular importance. The total missing energy observed in data events compared with that predicted in the MC can be seen in figure 7.11. No significant excess above that produced by the Standard Model processes is observed in any of the signal regions across the main p_{T} range.

Two events are seen in data with missing transverse energies between 560 GeV and 640 GeV, these events also contain exactly one b-jet and possess an effective mass of at least 900 GeV. They are hence seen in all three of the $\geq$1 b-jet signal regions and can be seen in the images on the left in figure 7.11. Two additional events are seen with missing transverse energies between 440 GeV and 520 GeV, which contain at least two b-jets and an effective mass of at least 900 GeV. These events are therefore seen in all three $\geq$2 b-jets signal regions and can be seen in the images on the right in figure 7.11. There is no, or very little, background prediction in these missing energy ranges and so only further studies on a larger data set can provide illumination on the nature of these events.

Signal Region Effective Mass

As explained in section 7.5 the amount of effective mass in events influences where on the gluino-$s$bottom mass plane the greater sensitivity lies. So a potential excess observed in this quantity would be a useful analysis tool in order to determine the properties of the signal process. As can be seen in figure 7.12, no such excess is seen in this dataset as the background, primarily the Standard Model top process, is observed to account for the total transverse energy present in the signal regions. There is a fluctuation of events with an effective mass of between 880 GeVand 920 GeV in the $\geq$2 b-jets signal regions, which is due to the lack of statistics seen

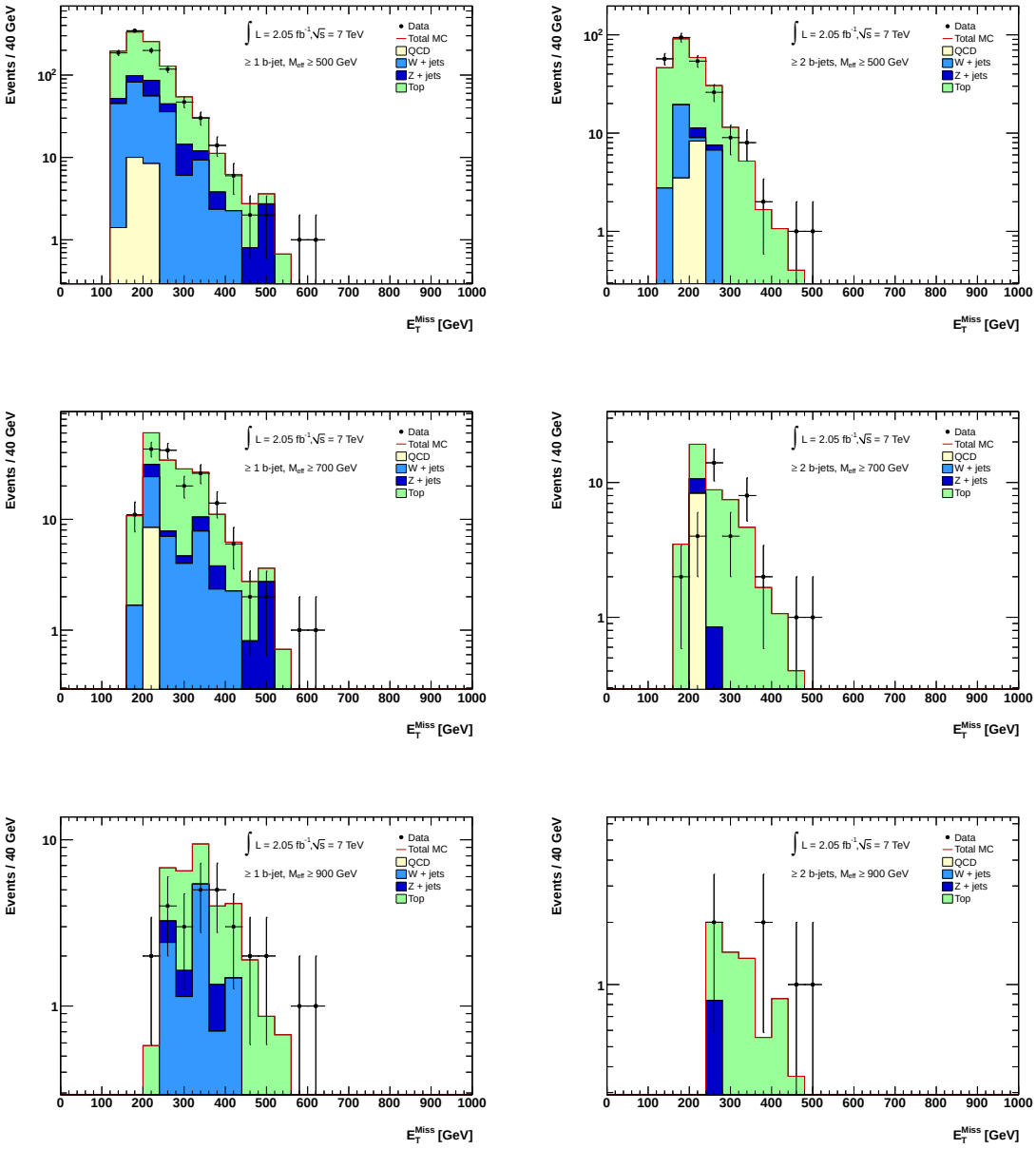

Figure 7.11: The missing transverse energy $E_{\mathrm{T}}^{\mathrm{miss}}$ in each event after the final selection criteria in signal regions requiring 1 b-jet (left) and 2 b-jets (right) and an effective mass of at least 500 GeV(top), 700 GeV(middle) and 900 GeV(bottom).

in those regions and this fluctuation is not seen in the $\geq$1 b-jet regions.

There are three events observed with an effective mass greater than 1400 GeV, two of these contain exactly one b-jet whereas the other contains at least two. These are identified as the same three events mentioned in the previous section above.

Signal Region Proportional Missing Energy

In figure 7.13 the ratio of missing transverse energy and effective mass in each of the signal regions is shown. This quantity is sensitive to the fraction of the momentum carried away by unobserved particles compared to the total detected in the final state, which would be expected to be large in the case of a neutralino. There is no significant excess of missing energy as a proportion of the total momentum observed in the data above the threshold value set in the selection requirements.

As no excess above the Standard Model predictions is observed in the data in any of the separate signal regions, exclusion limits are therefore established to account for the degree of confidence with which the lack of observation is held for different gluino and $s$bottom masses. The limits and the methods used to derive them are discussed in the following chapter.

Comparison with Signal Prediction

In figure 7.14 the distributions predicted for the Standard Model and those observed in the data are compared with the prediction for one example signal process mass point. The mass of the gluino at this mass point is 500 GeV, that of the $s$bottom 280 GeV and the comparison is carried out in signal regions requiring at least 1 b-jet (on the left) and at least 2 b-jets (on the right), with an effective mass in events of at least 500 GeV. As can be seen, although there is good agreement with the Standard Model prediction, no distinctive excess in the high p_{T} regions is observed in any of the important signal region quantities.

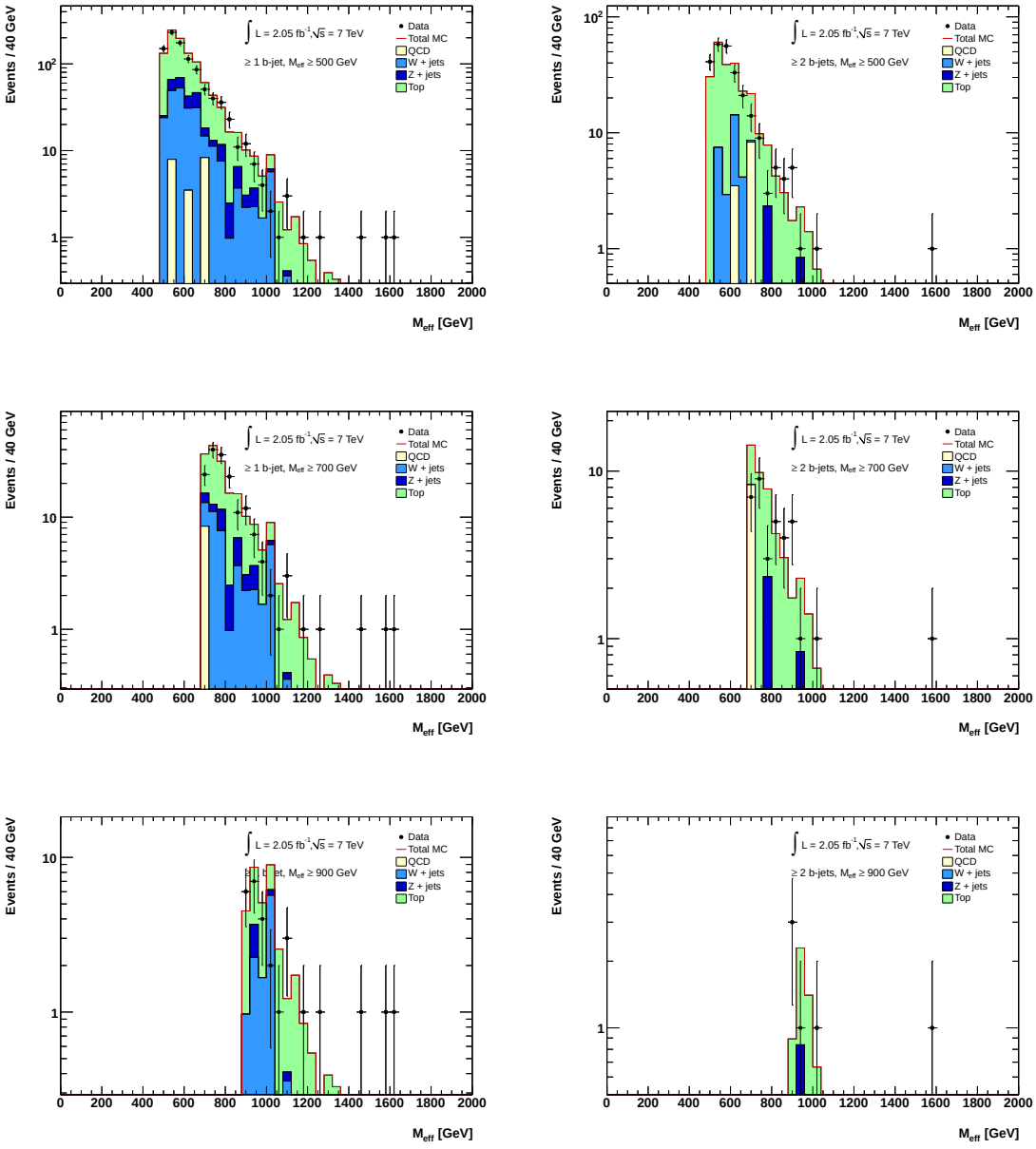

Figure 7.12: The total effective mass M_{eff} in each event after the final selection criteria in signal regions requiring 1 b-jet (left) and 2 b-jets (right) and an effective mass of at least 500 GeV(top), 700 GeV(middle) and 900 GeV(bottom).

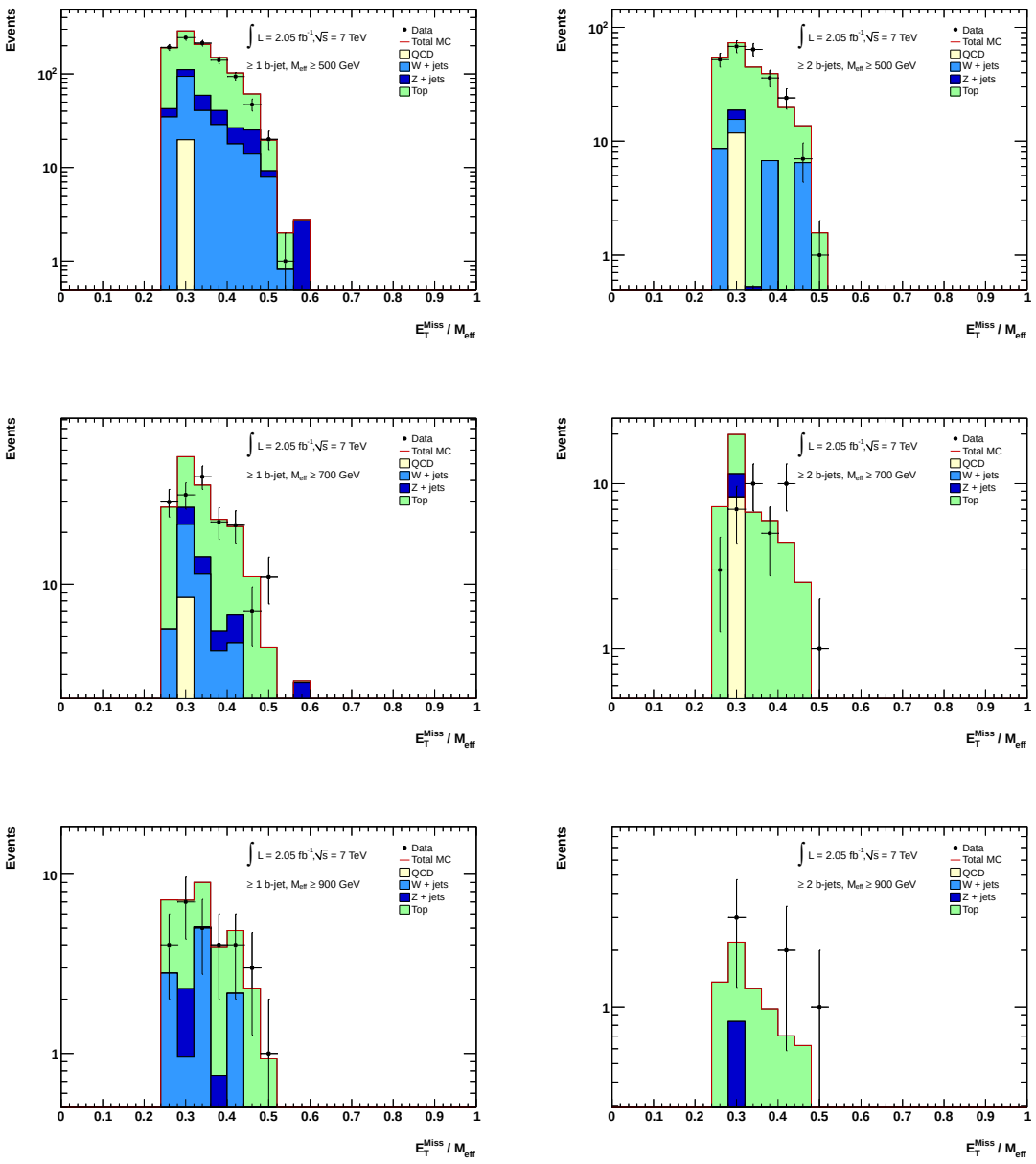

Figure 7.13: The Ratio of the missing transverse energy $E_{\mathrm{T}}^{\mathrm{miss}}$ to the effective mass M_{eff} after the final selection criteria in signal regions requiring 1 b-jet (left) and 2 b-jets (right) and an effective mass of at least 500 GeV(top), 700 GeV(middle) and 900 GeV(bottom).

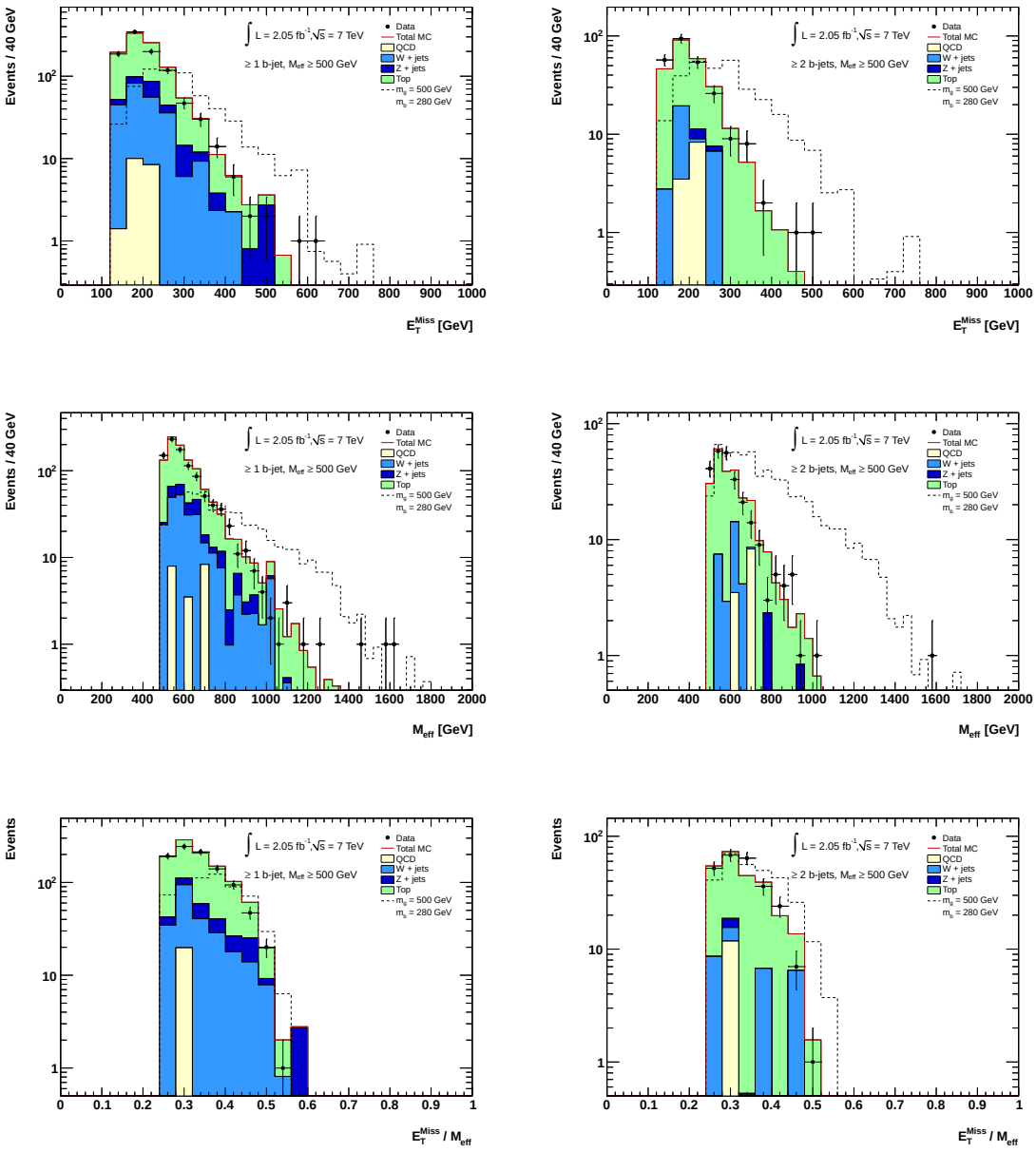

Figure 7.14: Standard Model background and observed data compared with the distributions expected from an example signal mass point for the $E_{\mathrm{T}}^{\mathrm{miss}}$ (top), M_{eff} (middle) and the ratio between the two (bottom). The comparisons are carried out after the final selection criteria in signal regions requiring 1 b-jet (left) and 2 b-jets (right) and an effective mass of at least 500 GeV.

Chapter 8

Interpretation of Results

In chapter 7 a search for $s$bottom quarks produced from the decay of gluinos has been presented. None of the signal regions in this search channel have been shown to exhibit a significant excess of this process being observed above the predicted Standard Model backgrounds. To quantify which SUSY points can be excluded with the current dataset and which cannot, a statistical treatment must be applied to the results that have been presented and from this an exclusion limit then calculated.

For each SUSY point included in the search, a confidence level is calculated quantifying how statistically likely it is that the total number of events observed can be explained purely by the background, given the predicted number of events to be observed for that point. From this set of confidence levels an exclusion limit is defined as the region excluding all the points for which the confidence level of a background only observation is at least 95%.

These exclusion limits are calculated statistically and the alternative limits presented here are constructed using the same data, but fundamentally different statistical approaches, with the motivation of comparing the final results produced by each approach.

8.1 Statistical Introduction

There is more than one basic approach to the subject of statistics, primarily depending on the different interpretation of the concept of *probability* that is followed. These separate approaches are sometimes complementary to one another and sometimes in disagreement, each can have its own relative strengths in certain scenarios and weaknesses in others. They each originate from the same starting point, the basic rules of probability. For a mutually exclusive set of possibilities, that is in the case where one and only one of the given possibilities can be true, these rules of probability can be stated as

$$\mathbf{P}(x) \geq 0 \tag{8.1}$$

$$\mathbf{P}(x_1 \; or \; x_2) = \mathbf{P}(x_1) + \mathbf{P}(x_2), \tag{8.2}$$

$$\sum_i \mathbf{P}(x_i) = 1, \tag{8.3}$$

where, in general, $\mathbf{P}(x)$ is the probability associated with x. Although both the Frequentist and Bayesian approaches described here build upon these basic rules of probability, the philosophy of how to treat these probabilities that is followed in each case is fundamentally different.

8.1.1 Frequentist Statistics

In the Frequentist approach to probability theory the frequency with which some event occurs is compared to the total number of observations made in which it could have occurred [56]. So if an experiment is carried out N number of times and a particular result is observed in R of these cases, then as N tends to infinity, $\mathrm{N} \longrightarrow \infty$, the ratio obtained $(\frac{R}{N})$ tends to a particular limit. In this approach to statistics, this limit, defined in equation 8.4, is interpreted as the probability of R occurring, $\mathbf{P}(\mathrm{R})$.

$$\mathbf{P}(R) = \lim_{N \to \infty} \frac{R}{N}. \tag{8.4}$$

8.1.2 Bayesian Statistics

The Bayesian approach differs from the Frequentist approach in that it is based upon *conditional* probability. This is the probability that one thing is true given that some other thing is already taken to be true. In Bayesian statistics this is carried out by utilising what is known as Bayes' theorem, which can be derived from the basic rules of probability [57] and, in the case of testing whether a proposed hypothesis is correct given a set of observed data, can be stated as

$$\mathbf{P}(hypothesis \mid data) = \frac{\mathbf{P}(data \mid hypothesis)\ \mathbf{P}(hypothesis)}{\mathbf{P}(data)}, \tag{8.5}$$

where, as before, $\mathbf{P}(x)$ is the probability of x being true. The conditional probability $\mathbf{P}$(hypothesis | data) is taken as the probability of the hypothesis being true given the observed data and $\mathbf{P}$(data | hypothesis) is the probability of the given data being observed if the hypothesis is true. The probability of the proposed hypothesis being true, $\mathbf{P}$(hypothesis), is referred to as the *prior* probability and is taken as the degree of certainty of the hypothesis being true prior to the experiment taking place given the already existing evidence, for example the results of previous experiments.

8.2 Confidence Levels

Confidence levels, as applied to experimental results, are used to quantify the degree to which the result of a given observation agrees with a particular hypothesis. In the context of this analysis the confidence level for a hypothesis that the

observed number of events is explained only by the Standard Model background, CL_b, is defined as

$$CL_b = P_b(X \leq X_{obs}) = \int_0^{X_{obs}} \frac{dP_b}{dX} dX, \tag{8.6}$$

where X is the parameter which attempts to distinguish signal like data from background like data and X_{obs} is the value actually observed for this parameter. P_b is the probability of the observed value being greater than the predicted value for this hypothesis. Here $\frac{dP_b}{dX}$ is the Probability Distribution Function (PDF) of the parameter X. The integration of this probability distribution up to observed value, X_{obs}, gives the confidence level for the background only hypothesis being true.

8.2.1 The CL_{s+b} Method

Given that, in the search scenario in this analysis, the potential presence of the SUSY signal would show up in addition to the already present Standard Model background it is preferable to calculate the confidence level in this case for the *signal + background* hypothesis. The confidence level here is defined as

$$CL_{s+b} = P_{s+b}(X \leq X_{obs}) = \int_0^{X_{obs}} \frac{dP_{s+b}}{dX} dX, \tag{8.7}$$

where the variables are defined as before and $\frac{dP_{s+b}}{dX}$ is the PDF, the integration of which up to the observed value X_{obs} produces the confidence level.

8.2.2 The CL_s Method

The common method of setting exclusion limits in ATLAS is known as the CL_s method [58, 59]. This alternate method is used as there is an inherent problem possible within the CL_{s+b} method in that an overestimate of the background,

combined with no signal, could lead to an erroneous exclusion. To avoid this an extra step can be taken, defining the new quantity, CL_s

$$CL_s = \frac{CL_{s+b}}{CL_b}, \tag{8.8}$$

where the confidence level for the signal + background hypothesis is normalised to the the confidence level for the background only. In this case CL_s is in reality a ratio of two confidence levels rather than an actual confidence level itself.

To test for the potential presence of a signal in the data the value $1 - CL_b$ can be used to distinguish between a null hypothesis and a signal hypothesis. Its value may be used in order to measure the degree of significance of any excess observed. Comparatively with using only CL_{s+b} for constructing an exclusion limit, the quantity $1 - CL_b$ assumes a perfectly accurate prediction for signal and background. As in the case where the background has been underestimated, so too the signal could be overestimated resulting in a potentially premature announcement of a discovery. Using the same approach as before it is useful to introduce

$$\frac{1 - CL_b}{1 - CL_{s+b}}, \tag{8.9}$$

where the quantity $1 - CL_b$ has been normalised to the total signal + background distribution. Using this approach leads to a far more robust estimation of the degree of signal significance observed.

All of the CL_x based methods described here use the frequentist statistical approach described in section 8.1.1. The primary original motivation for using the CL_s method on ATLAS results was to enable direct comparisons with previous Tevatron results.

8.2.3 The Bayesian Method

Using the Bayesian approach to probabilities described in section 8.1.2 an alternative procedure is also carried out to obtain a set of confidence levels with a fundamentally different probabilistic philosophy and to expand the scope of the statistical interpretation of the analysis results.

In all the different methods described above these confidence levels can be calculated separately for the signal predicted by each SUSY point and a confidence level grid can be obtained. From this grid the exclusion limits can be set.

8.3 Limits for Different Statistical Approaches

Exclusion limits are produced on the gluino-$s$bottom mass plane to determine the extent of the exclusion of the signal process from this analysis. These limits are constructed independently using each of the statistical approaches described in the previous section, including individual limits representing the CL_s and CL_{s+b} methods of the Frequentist approach and one limit representing the Bayesian approach. The limits are produced separately for each signal region and the limit in the region with the greatest reach taken.

The results of these limits are then used to determine which individual mass points have been excluded and which have insufficient evidence in the data to support their exclusion. The final results from each signal region are additionally compared for CL_s and the Bayesian method in order to ascertain the differences and similarities between each statistical approach.

8.3.1 Event Yields

The number of events coming from the analysis presented in chapter 7 which pass all selection criteria and make it into at least one of the signal regions is shown in table 8.1. These yields are shown for both the data and total combined Monte

Carlo prediction. As seen in the previous chapter there is no excess observed in the data over these Monte Carlo predictions and so the procedure described here is optimised to set exclusion limits on the data as opposed to quantifying the significance of any excess.

Signal Region	Definition	Total MC	Data
1a	≥ 1 b-jet, ≥ 500 GeV M_{eff}	1022.8	951
1b	≥ 1 b-jet, ≥ 700 GeV M_{eff}	185.4	168
1c	≥ 1 b-jet, ≥ 900 GeV M_{eff}	35.5	28
2a	≥ 2 b-jet, ≥ 500 GeV M_{eff}	247.1	252
2b	≥ 2 b-jet, ≥ 700 GeV M_{eff}	47.3	36
2c	≥ 2 b-jet, ≥ 900 GeV M_{eff}	7.2	6

Table 8.1: Summary of the event yield for all six signal regions showing the total events observed in data and correspondingly the total observed in Monte Carlo.

To create the exclusion limits the total number of events observed in the data and the total number predicted in the Monte Carlo in each signal region are compared to the number of events seen for each of the individual mass points of the signal process. The efficiency of the selection criteria described in chapter 7 is taken from each of these separate event yields by calculating what proportion of the overall number of events survived these cuts. These efficiencies, along with the theoretical cross-sections relating to the signal processes for each of the mass points, are then used to construct the exclusion limits.

8.3.2 Cross-sections

The theoretically predicted cross-sections for the gluino mediated $s$bottom production processes considered here are assumed to only be dependent on the mass of the initial gluino pair produced and not those of the subsequent $s$bottom quarks or the final state lightest supersymmetric particle. The table in 8.2 shows the

values used in this analysis for these cross-sections for gluino masses between 360 GeV and 1000 GeV.

gluino mass [GeV]	Cross-section [pb]	gluino mass [GeV]	Cross-section [pb]
360	20.0	700	0.194
400	10.4	750	0.109
450	4.78	800	0.0633
500	2.35	850	0.0428
550	1.19	900	0.0223
600	0.638	950	0.01526
650	0.342	1000	0.00822

Table 8.2: The cross-sections for the different gluino mass signal processes.

8.3.3 Interpolation Procedure

An interpolation procedure is carried out in order to produce distributions across the gluino-$s$bottom mass plane with a finer resolution than that of the signal grid used. This original grid has mass points separated by 50 GeV in gluino mass and 40 GeV in $s$bottom mass, the interpolation procedure increases this resolution to 1 GeV increments in both axes. This procedure creates a new effective signal grid comprising of 486,400 individual points between in the mass plane, in the region $360 \leq m_{\tilde{g}} \leq 1000$ and $240 \leq m_{\tilde{b}} \leq 1000$. This interpolation procedure is carried out for both the signal efficiencies and cross-sections in order to provide corresponding values for each new mass point.

The effect of this procedure for the interpolation of the cross-sections is shown, for region 2b, in figure 8.1 and for the efficiencies in figure 8.2, for each individual mass point in both cases. These values are then compared, one mass point at a time, alongside those for the total background Monte Carlo and the equivalent efficiency observed in data utilising the processes described in section 8.2.

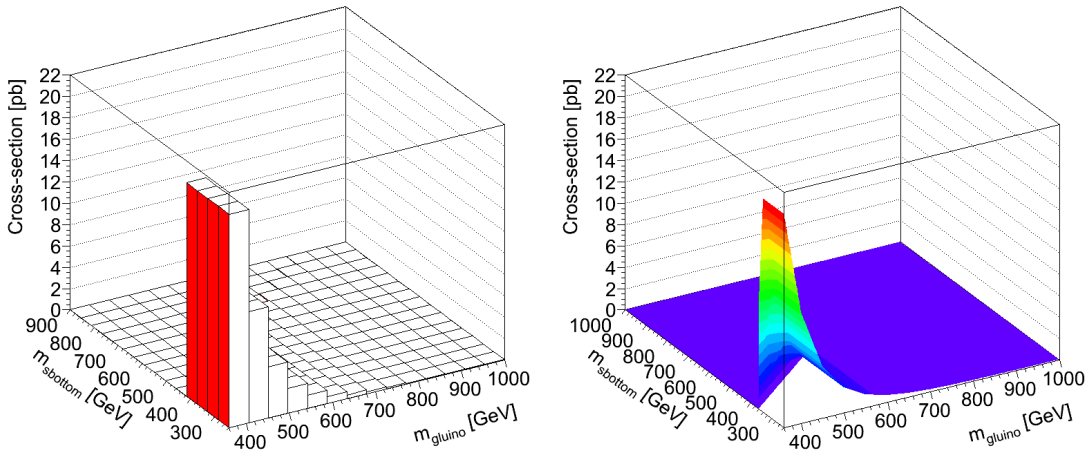

Figure 8.1: The cross-section for each SUSY mass point on the sbottom-gluino mass plane both before (left) and after (right) the interpolation procedure in signal region 2b.

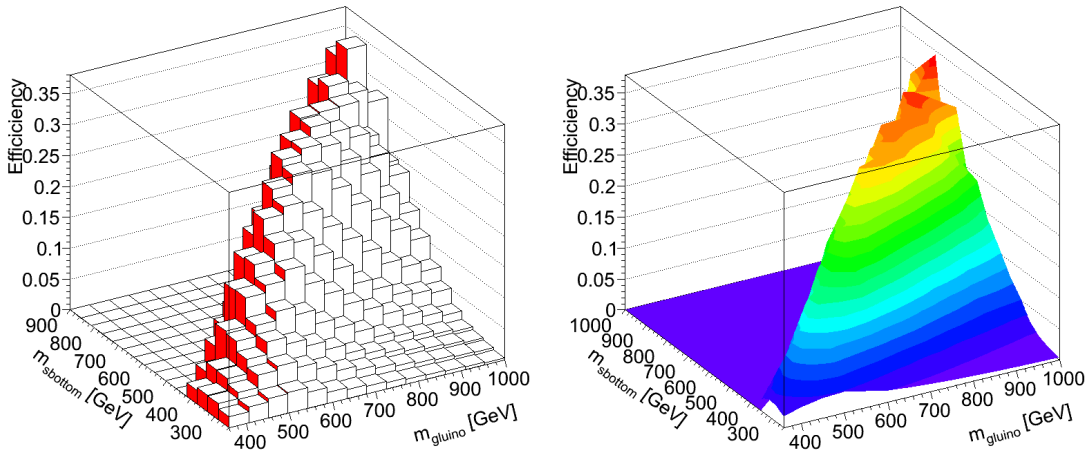

Figure 8.2: The signal efficiency for each SUSY mass point on the sbottom-gluino mass plane both before (left) and after (right) the interpolation procedure in signal region 2b.

The final 1 GeV mass resolution exclusion limits in each signal region can then be constructed from the information obtained through this procedure and these limits are presented in the final section.

8.3.4 Exclusion Limits

In figure 8.3 the observed exclusion limits at 95% confidence level are shown in each signal region using the CL_{s+b} method. Building upon this method, figure 8.4 shows the observed and expected exclusion limits at 95% confidence level in each signal region using the CL_s method. As expected this method yields different limits than those obtained purely from the CL_{s+b} method, but the difference here is minimal in terms of excluded gluino and *s*bottom masses. The limits shown in red in figure 8.4 represent the value of the 95% confidence level exclusion that is to be expected in the absence of a signal and the limits shown in grey represent the range within which 90% of experiments would be expected to fall, the lower line is a standard deviation of 2σ below the expected limit and the upper line 2σ above. Following the CL_s statistical approach, gluino masses below 800 GeV are excluded across all signal regions. No *s*bottom masses are excluded above a gluino mass of 950 GeV in any of the signal regions.

Figure 8.5 shows the observed exclusion limits at 95% confidence level using the Bayesian method in each of the four higher effective mass signal regions[1]. Significantly higher statistics in the lower effective mass signal regions make the use of this method particularly difficult. In the regions it is applied to this statistical approach yields a very comparable prediction for the mass points excluded by the observed limit to that of the CL_s method.

A direct comparison between the limits obtained by the CL_s and Bayesian approaches is now therefore possible and this comparison is displayed in figure 8.6. The comparison is shown in the signal region requiring at least two *b*-tagged jets and an effective mass of at least 700 GeV. The close agreement between the two

[1]Signal regions: 1b, 1c, 2b and 2c

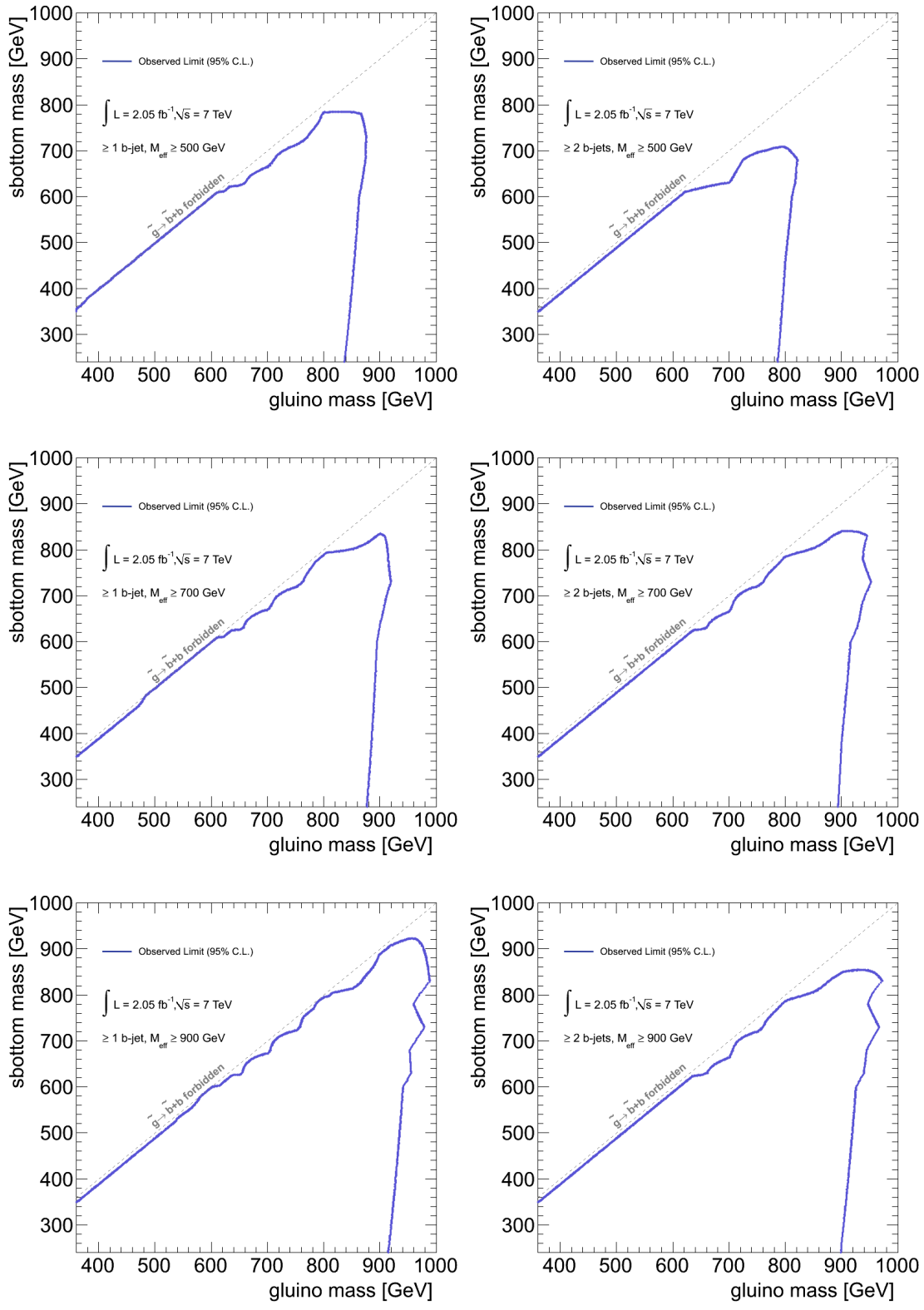

Figure 8.3: The CL_{s+b} observed exclusion limits for each signal region, requiring at least one b-tag (left), two b-tags (right) and $M_{eff} \geq 500$ GeV (top), 700 GeV (middle) and 900 GeV (bottom).

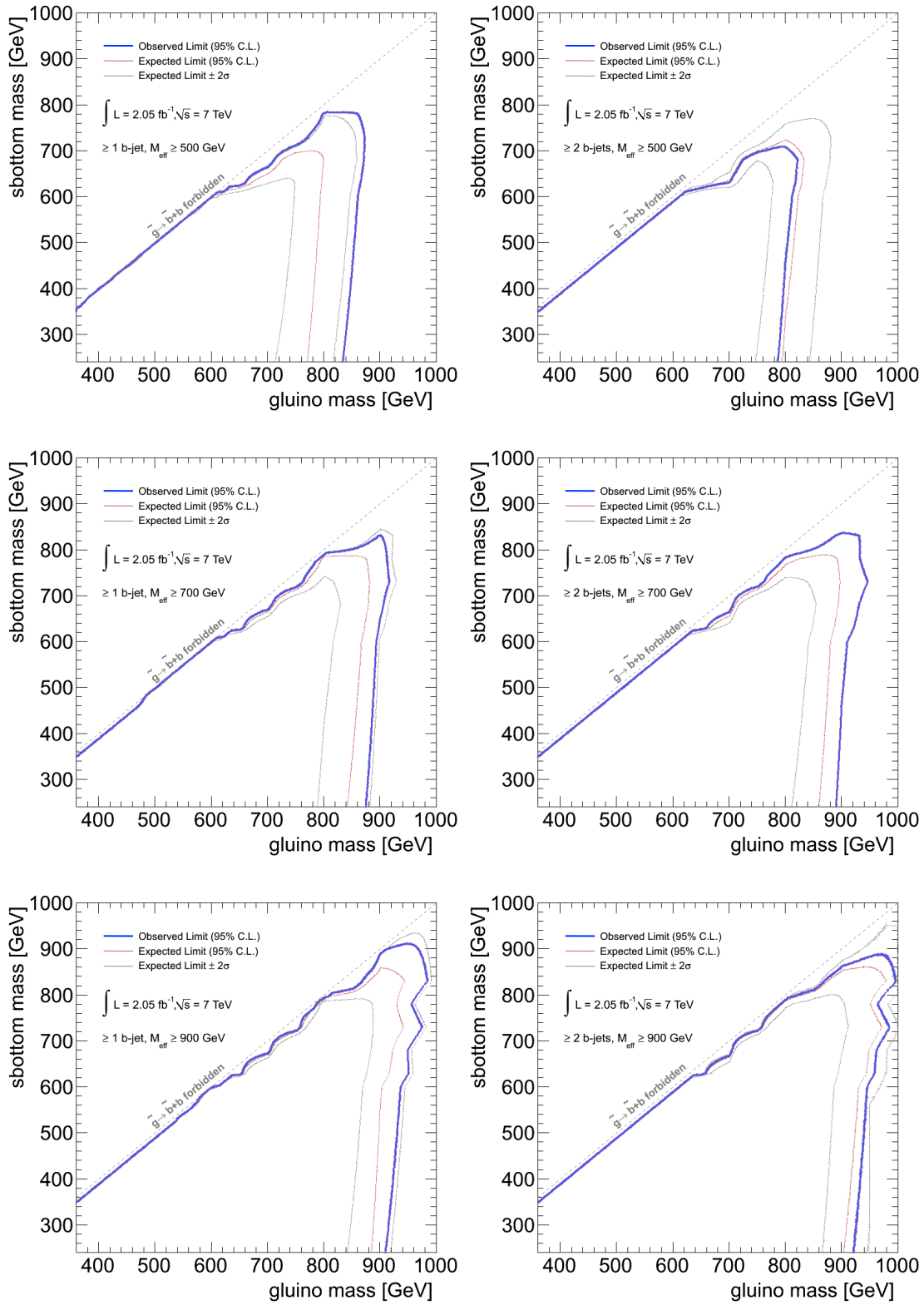

Figure 8.4: The CL_s observed and expected exclusion limits for each signal region, requiring at least one b-tag (left), two b-tags (right) and $M_{eff} \geq 500$ GeV (top), 700 GeV (middle) and 900 GeV (bottom).

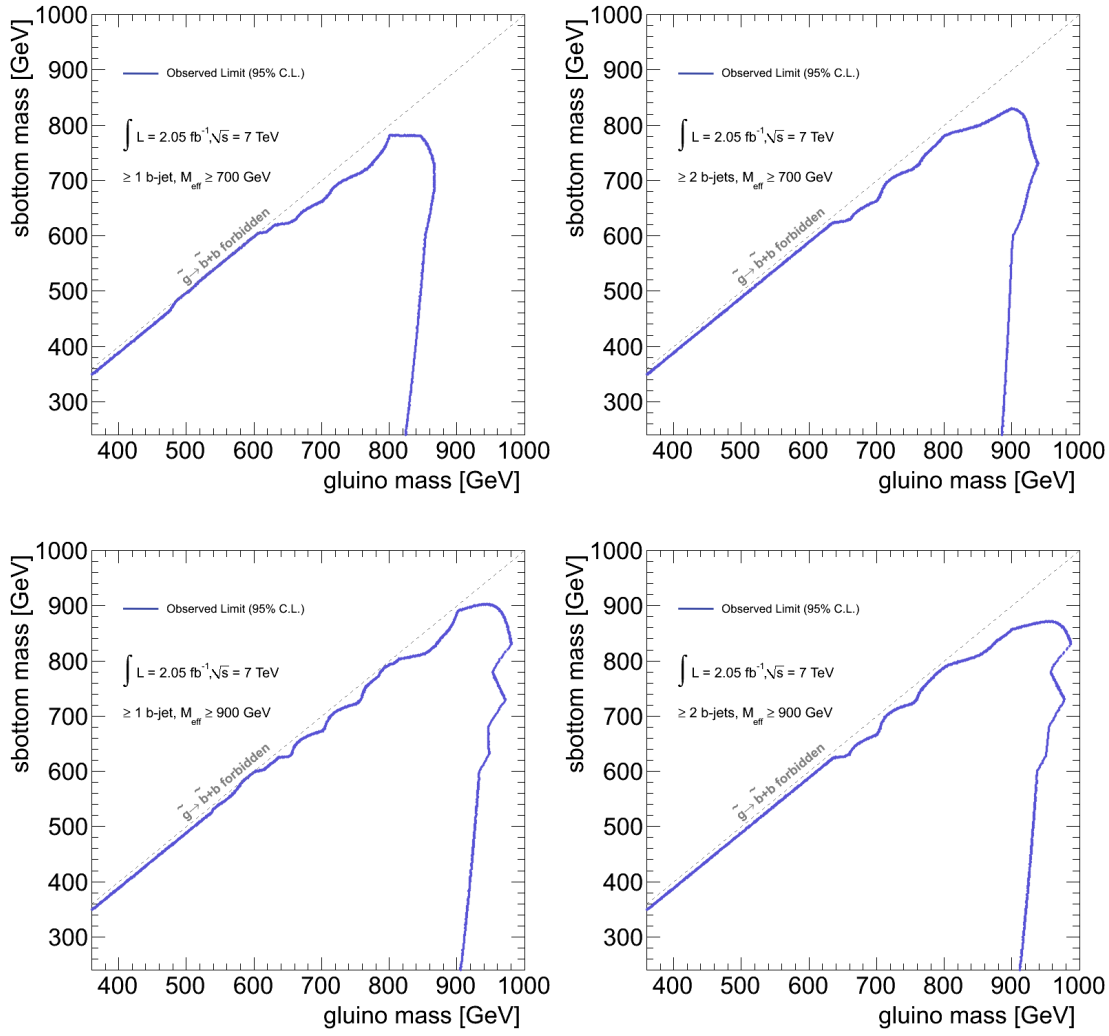

Figure 8.5: The Bayesian observed exclusion limits for each signal region, requiring at least one b-tag (left), two b-tags (right) and $M_{eff} \geq 700$ GeV (top) and 900 GeV (bottom).

methods on which mass points are excluded reinforces the confidence in the limits set. In addition, it also demonstrates the viability of the Bayesian approach to statistics in this application.

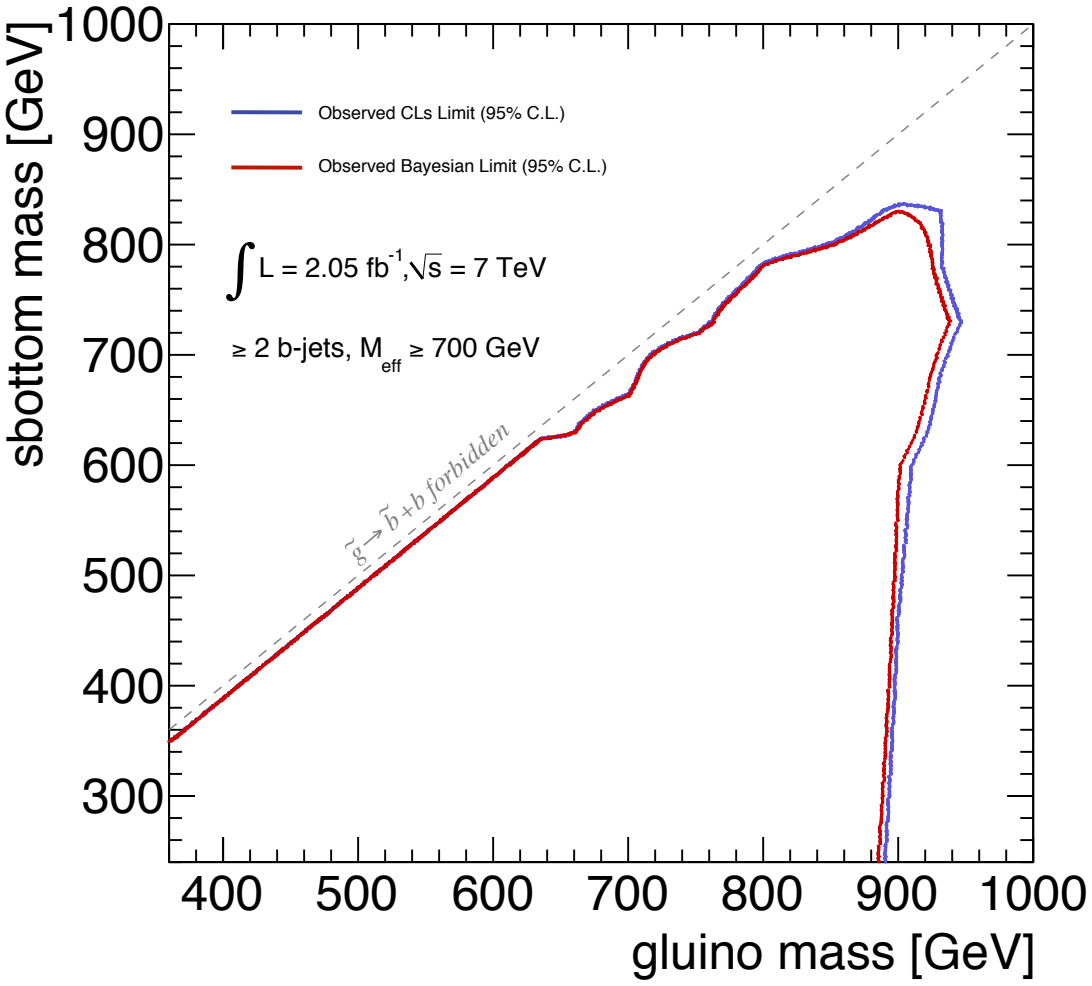

Figure 8.6: A comparison of the observed exclusion limits set using both the CL_s and Bayesian methods in the signal region requiring $M_{eff} \geq 700$ GeV and at least 2 b-tags.

Chapter 9

Summary

A search for the supersymmetric gluino mediated sbottom production process in proton-proton collisions has been presented. This search was performed using 2.05 fb^{-1} of data recorded during 2011 by the ATLAS detector at the LHC, at a centre of mass energy of $\sqrt{s} = 7$ TeV.

The six signal regions studied in this search in order to achieve the maximum sensitivity across the gluino-$s$bottom mass plane were defined as

- **Region 1a -** At least 1 b-jet with a $p_{\mathrm{T}} > 50$ GeV and $M_{eff} \geq 500$ GeV.
- **Region 1b -** At least 1 b-jet with a $p_{\mathrm{T}} > 50$ GeV and $M_{eff} \geq 700$ GeV.
- **Region 1c -** At least 1 b-jet with a $p_{\mathrm{T}} > 50$ GeV and $M_{eff} \geq 900$ GeV.
- **Region 2a -** At least 2 b-jets with a $p_{\mathrm{T}} > 50$ GeV and $M_{eff} \geq 500$ GeV.
- **Region 2b -** At least 2 b-jets with a $p_{\mathrm{T}} > 50$ GeV and $M_{eff} \geq 700$ GeV.
- **Region 2c -** At least 2 b-jets with a $p_{\mathrm{T}} > 50$ GeV and $M_{eff} \geq 900$ GeV.

where in all regions a 0-lepton based selection criteria was also applied to all events prior to consideration, including the requirements of a leading jet $p_{\mathrm{T}} > 130$ GeV, a minimum of two further jets with a $p_{\mathrm{T}} > 50$ GeV, a missing transverse

energy of greater 130 GeV and a ratio between the missing energy and effective mass of at least 0.2.

Two distinct statistical approaches were studied, Frequentist statistics and Bayesian statistics. Three separate and complimentary confidence limits were extracted from the results obtained from each of the signal regions. One being that derived from the Bayesian approach and two, the CL_s and CL_{s+b} methods, derived from the Frequentist approach.

No excess of a significant nature is seen in any of the signal regions and the observed number of events from the data appearing in these signal regions are consistent with the Standard Model prediction. Adopting the CL_s method, utilising a frequentist statistical approach, gluino masses of less than 800 GeV have been explicitly excluded to a 95% confidence level across all signal regions. This is an improvement on exclusion limits for this process set, for both the gluino and sbottom masses, at the tevatron [51] and in previous ATLAS results [60].

The viability of a Bayesian approach to statistical limit setting in supersymmetry searches has also been demonstrated and adopting this approach to the analysis presented here is found to yield limits comparable to those of the common CL_s approach.

Appendix A

Monte Carlo Samples

In this Appendix are listed all the individual Monte Carlo simulated samples utelised in this analysis, for both predicted SUSY signal and Standard Model background. They are further separated within these groups into categories that are explained in the following two sections.

A.1 SUSY Signal Samples

Listed in the three tables A.1-A.2 are the individual simulated MC samples used to characterise the SUSY signal in this analysis. The samples were produced and subsequently used in a form where the events were split into different samples due to the combination of *s*particle masses they assumed.

Table A.1 shows samples representing various gluino and sbottom masses with a fixed neutralino mass of $\widetilde{\chi}_1^0 = 60$ GeV. Table A.2 shows a further extension to this same $\widetilde{\chi}_1^0 = 60$ GeV grid with additional gluino and sbottom masses extending the grid in both directions.

A.2 Standard Model Background Samples

Listed in the five tables A.3-A.7 are the individual samples comprising the different Standard Model background processes. Each table lists the samples representing one type of Standard Model process. The information given for each sample includes the sample identification number (ID), sample name, the Monte Carlo generator used to produce the sample, the total number of events simulated and the Standard Model cross-section for the process simulated in the sample.

In table A.3 the samples constituting the di-jet QCD process are given. The samples are separated by the p_{T} range of the jets they contain, J0 being the lowest and J8 the highest p_{T} ranges. These samples are, in terms of number of simulated events, the largest MC samples used in this analysis.

Tables A.4 and A.5 show the samples constituting the W and Z bosons + jets processes. These samples are separated both by the method of their decay and by the p_{T} ranges of the jets in the events, Np0 being the lowest and Np5 being the highest. In the case of the W + jets process the decay is characterised by the lepton or quark flavour (e/μ/τ for leptons or c/b for quarks) the W boson decays to. In the case of the Z + jets process the decay is similarly characterised by the lepton flavour of the Z decay, with the additional possibility of the decay to neutrinos.

The top process, both single top and top pair production, is given in table A.6. For the single top case the samples are separated by the channel through which the top quark is produced (as illustrated in figure 7.2) as well as by the lepton flavour produced in its subsequent decay. For the case of top pair production the samples are separated by whether the top quark decays are fully hadronic or have a leptonic component.

Table A.7 shows the three separate Di-boson samples, with the different possible combinations of vector bosons, WW, ZZ and WZ.

Sample ID	Gluino Mass [GeV]	sbottom [GeV]	Events
118208	360	240	20,000
118209	360	340	20,000
118210	360	310	20,000
118211	360	280	20,000
118212	400	280	20,000
118213	400	240	20,000
118214	400	380	20,000
118215	400	340	20,000
118216	400	310	20,000
118217	450	310	20,000
118218	450	280	20,000
118219	450	240	20,000
118220	450	420	20,000
118221	450	380	20,000
118222	450	340	20,000
118223	500	280	20,000
118224	500	240	20,000
118225	500	470	20,000
118226	500	420	20,000
118227	500	380	20,000
118228	500	340	20,000
118229	500	310	20,000
118230	600	240	20,000
118231	600	530	20,000
118232	600	470	20,000
118233	600	420	20,000
118234	600	380	20,000
118235	600	340	20,000
118236	600	310	20,000
118237	600	280	20,000
118238	700	380	20,000
118239	700	310	20,000
118240	600	580	20,000
118241	700	580	20,000
118242	700	530	20,000
118243	700	470	20,000
118244	700	420	20,000
118245	700	650	20,000

Table A.1: A list of SUSY Monte Carlo samples used and the individual *s*particle masses for each sample, along with the number of events simulated. These samples were produced assuming a Neutralino mass of $\widetilde{\chi}_1^0 = 60$ GeV

Sample ID	Gluino Mass [GeV]	sbottom [GeV]	Events
139012	550	340	20,000
139013	550	380	20,000
139014	550	420	20,000
139015	550	470	20,000
139016	550	530	20,000
139017	650	280	20,000
139018	650	310	20,000
139019	650	340	20,000
139020	650	380	20,000
139021	650	420	20,000
139022	650	470	20,000
139023	650	530	20,000
139024	650	580	20,000
139025	650	630	20,000
139026	750	310	20,000
139027	750	380	20,000
139028	750	420	20,000
139029	750	470	20,000
139030	750	530	20,000
139031	750	580	20,000
139032	750	630	20,000
139033	750	680	20,000
139034	800	340	20,000
139035	800	420	20,000
139036	800	470	20,000
139037	800	530	20,000
139038	800	580	20,000
139039	800	630	20,000
139040	800	680	20,000
139041	800	730	20,000
139042	800	780	20,000
139043	900	340	20,000
139044	900	420	20,000
139045	900	470	20,000
139046	900	530	20,000
139047	900	580	20,000
139048	900	630	20,000
139049	900	680	20,000
139050	900	730	20,000
139051	900	780	20,000
139052	900	830	20,000
139053	900	880	20,000
139054	1000	420	20,000
139055	1000	470	20,000
139056	1000	530	20,000
139057	1000	630	20,000
139058	1000	730	20,000
139059	1000	830	20,000
139060	1000	880	20,000

Table A.2: A list of SUSY Monte Carlo samples used and the individual *s*particle masses for each sample, along with the number of events simulated. These samples were produced assuming a Neutralino mass of $\widetilde{\chi}_1^0 = 60$ GeV

Sample ID	Sample Name	Generator	Events	Cross-section [nb]
105009	J0 jetjet	Pythia	16,388,258	9.86×10^{6}
105010	J1 jetjet	Pythia	7,382,565	6.78×10^{5}
105011	J2 jetjet	Pythia	2,796,084	4.10×10^{4}
105012	J3 jetjet	Pythia	2,796,879	2.19×10^{3}
105013	J4 jetjet	Pythia	2,793,179	87.7
105014	J5 jetjet	Pythia	2,790,576	2.35
105015	J6 jetjet	Pythia	2,790,601	0.34
105016	J7 jetjet	Pythia	1,395,025	0.14
105017	J8 jetjet	Pythia	1,353,250	0.60×10^{-5}

Table A.3: A list of the di-jet QCD Monte Carlo samples, the generators used to produce them, the number of events simulated and their respective cross-sections. The different datasets J0-J8 represent samples containing increasing jet energies.

Sample ID	Sample Name	Generator	Events	Cross-section [pb]
107680	WenuNp0_pt20	Alpgen Jimmy	3,455,037	6921.60
107681	WenuNp1_pt20	Alpgen Jimmy	641,361	1304.30
107682	WenuNp2_pt20	Alpgen Jimmy	3,768,265	378.29
107683	WenuNp3_pt20	Alpgen Jimmy	1,009,641	101.43
107684	WenuNp4_pt20	Alpgen Jimmy	249,869	25.87
107685	WenuNp5_pt20	Alpgen Jimmy	69,953	7.00
107690	WmunuNp0_pt20	Alpgen Jimmy	3,156,559	6919.60
107691	WmunuNp1_pt20	Alpgen Jimmy	641,867	1304.20
107692	WmunuNp2_pt20	Alpgen Jimmy	1,559,535	377.83
107693	WmunuNp3_pt20	Alpgen Jimmy	1,009,589	101.88
107694	WmunuNp4_pt20	Alpgen Jimmy	254,879	25.75
107695	WmunuNp5_pt20	Alpgen Jimmy	69,958	6.92
107700	WtaunuNp0_pt20	Alpgen Jimmy	2,049,654	6918.60
107701	WtaunuNp1_pt20	Alpgen Jimmy	641,809	1303.20
107702	WtaunuNp2_pt20	Alpgen Jimmy	1,949,307	378.18
107703	WtaunuNp3_pt20	Alpgen Jimmy	1,009,548	101.51
107704	WtaunuNp4_pt20	Alpgen Jimmy	249,853	25.64
107705	WtaunuNp5_pt20	Alpgen Jimmy	63,692	7.04
107280	WbbFullNp0_pt20	Alpgen Jimmy	91,485	47.32
107281	WbbFullNp1_pt20	Alpgen Jimmy	67,475	35.77
107282	WbbFullNp2_pt20	Alpgen Jimmy	33,478	17.34
107283	WbbFullNp3_pt20	Alpgen Jimmy	12,997	6.63
117284	WccFullNp0_pt20	Alpgen	254,955	127.53
117285	WccFullNp1_pt20	Alpgen	206,446	104.68
117286	WccFullNp2_pt20	Alpgen	524,808	52.08
117287	WccFullNp3_pt20	Alpgen	33,984	16.96

Table A.4: The W Vector Boson + jets Monte Carlo samples, the generators that produced them, the number of events simulated and their adjusted cross-sections. The different datasets Np0-Npx represent samples containing increasing jet p_{T} with a minimum cut at 20 GeV.

Sample ID	Sample Name	Generator	Events	Cross-section [pb]
107650	ZeeNp0_pt20	Alpgen Jimmy	6,612,265	668.32
107651	ZeeNp1_pt20	Alpgen Jimmy	1,333,745	134.36
107652	ZeeNp2_pt20	Alpgen Jimmy	404,873	40.54
107653	ZeeNp3_pt20	Alpgen Jimmy	109,942	11.16
107654	ZeeNp4_pt20	Alpgen Jimmy	29,992	2.88
107655	ZeeNp5_pt20	Alpgen Jimmy	8,992	0.83
107660	ZmumuNp0_pt20	Alpgen Jimmy	6,619,010	668.68
107661	ZmumuNp1_pt20	Alpgen Jimmy	1,334,723	134.14
107662	ZmumuNp2_pt20	Alpgen Jimmy	403,886	40.33
107663	ZmumuNp3_pt20	Alpgen Jimmy	109,954	11.19
107664	ZmumuNp4_pt20	Alpgen Jimmy	29,978	2.75
107665	ZmumuNp5_pt20	Alpgen Jimmy	9,993	0.77
107670	ZtautauNp0_pt20	Alpgen Jimmy	6,618,801	668.40
107671	ZtautauNp1_pt20	Alpgen Jimmy	1,334,664	134.81
107672	ZtautauNp2_pt20	Alpgen Jimmy	1,949,307	40.36
107673	ZtautauNp3_pt20	Alpgen Jimmy	109,944	11.25
107674	ZtautauNp4_pt20	Alpgen Jimmy	29,982	2.79
107675	ZtautauNp5_pt20	Alpgen Jimmy	9,993	0.77
107710	ZnunuNp0_pt20_filt1jet	Alpgen Jimmy	60,485	3571.90
107711	ZnunuNp1_pt20_filt1jet	Alpgen Jimmy	909,288	737.84
107712	ZnunuNp2_pt20_filt1jet	Alpgen Jimmy	204,942	223.89
107713	ZnunuNp3_pt20_filt1jet	Alpgen Jimmy	140,929	61.83
107714	ZnunuNp4_pt20_filt1jet	Alpgen Jimmy	32,980	15.75
107715	ZnunuNp5_pt20_filt1jet	Alpgen Jimmy	9,492	4.17

Table A.5: A list of the Z Vector Boson + jets Monte Carlo samples, the generators that produced them, the number of events simulated and their respective cross-sections. The different datasets Np0-Npx represent samples containing increasing jet p_{T}, with a minimum cut at 20 GeV.

Sample ID	Sample Name	Generator	Events	Cross-section [nb]
105200	T1	Jimmy, McAtNlo	14,290,021	166.8
105204	TTbar_FullHad	Jimmy, McAtNlo	1,198,875	166.8
105861	TTbar_PowHeg	Pythia	998,771	166.8
105860	TTbar_PowHeg	Jimmy	998,286	166.8
108340	st_tchan_enu	Jimmy, McAtNlo	899,655	6.97
108341	st_tchan_munu	Jimmy, McAtNlo	899,655	6.97
108342	st_tchan_taunu	Jimmy, McAtNlo	899,655	6.97
108343	st_schan_enu	Jimmy, McAtNlo	899,572	0.5
108344	st_schan_munu	Jimmy, McAtNlo	899,572	0.5
108345	st_schan_taunu	Jimmy, McAtNlo	899,572	0.5
108346	st_Wt	Jimmy, McAtNlo	719,457	15.74
105890	ttbarlnlnNp0	Alpgen Jimmy	58,479	3.466
105891	ttbarlnlnNp1	Alpgen Jimmy	55,471	3.399
105892	ttbarlnlnNp2	Alpgen Jimmy	35,982	2.124
105893	ttbarlnlnNp3	Alpgen Jimmy	89,423	0.947
105894	ttbarlnqqNp0	Alpgen Jimmy	237,284	13.764
105895	ttbarlnqqNp1	Alpgen Jimmy	238,833	8.418
105896	ttbarlnqqNp2	Alpgen Jimmy	146,383	5.364
105897	ttbarlnqqNp3	Alpgen Jimmy	109,395	3.776

Table A.6: The Top quark (single and pair) Monte Carlo samples, the generators that produced them, the number of events simulated and their adjusted cross-sections.

Sample ID	Sample Name	Generator	Events	Cross-section [pb]
105985	Di-boson WW	Herwig	249,906	29.60
105986	Di-boson ZZ	Herwig	249,923	4.60
105987	Di-boson WZ	Herwig	249,906	11.23

Table A.7: The Di-boson Monte Carlo samples, the generators that produced them, the number of events simulated and their adjusted cross-sections.

Bibliography

[1] *CERN, the European Organization for Nuclear Research*, `http://public.web.cern.ch/public/`

[2] *The ATLAS Experiment at the CERN Large Hadron Collider*, ATLAS Collaboration, JINST. **3** S08003 (2008)

[3] Image from `http://en.wikipedia.org/wiki/Standard_Model`

[4] *Particles and Fundamental Interactions: An Introduction to Particle Physics*, S. Braibant, G. Giacomelli and M. Spurio, Springer (2009)

[5] *Gauge Theories in Particle Physics*, I. J. R. Aitchison and A. J. G. Hey, Taylor and Francis (2003)

[6] *Particle Data Group July 2004 Particle Physics Booklet*, Extracted from the Review of Particle Physics, S. Eidelman *et al* , Physics Letters B **592**, 1 (2004)

[7] *Broken Symmetry and the Mass of Gauge Vector Mesons*, F. Englert and R. Brout, Phys. Rev. Lett. **13**, 9 (1964)
Broken Symmetries and the Masses of Gauge Bosons, P. W. Higgs, Phys. Rev. Lett. **13**, 16 (1964)
Global Conservation Laws and Massless Particles, G. S. Guralnik, C. R. Hagen and T. W. B. Kibble, Phys. Rev. Lett. **13**, 20 (1964)

[8] *The Review of Particle Physics*, K. Nakamura *et al.* (Particle Data Group), J. Phys. G **37** (2010)

[9] *Measurement of the Solar Electron Neutrino Flux*, B.T. Cleveland *et al.*, Astrophys. J. **496**, 505 (1998)

[10] *Supersymmetric origin of neutrino mass*, M. Hirsch and J. W. F. Valle, New Journal of Physics **6** (2004) 76
Neutrino mass from R-parity violation in split supersymmetry, E. J. Chun and S. C. Park, JHEP01(2005) 9

[11] *Beyond the Standard Model (In Search of Supersymmetry)*, D. I. Kazakov, `arXiv:hep-ph/0012288v2` (2000)

[12] *Comparison of grand unified theories with electroweak and strong coupling constants measured at LEP*, U. Amaldi, W. de Boer, H. Furstenau, *et al* , Phys. Lett. B **260** (1991) 447.

[13] *A Supersymmetry Primer*, S. Martin, `arXiv:hep-ph/9709356v6`, version 5, (2008)

[14] *Gravitational Microlensing by the Galactic Halo*, B. Paczynski, Astrophys. J. **304**, 1 (1986)
Galactic microlensing as a method of detecting massive compact halo objects, K. Griest, Astrophys. J. **366**, 412 (1991)

[15] *A Case for a Baryonic Dark Halo*, F. De Paolis *et al.*, Phys. Rev. Lett. **74**, 14 (1995)

[16] Image from `http://www.physics.gla.ac.uk/ppt/bsm.htm`

[17] *LHC Design Report*, Volume 3, Chapter 1, *CERN-2004-003-V-1* (2004)

[18] *Tevatron Technical Design Report*, fermilab-design-1984-01 (1983)

[19] *LHC Design Report*, Volume 1 - Chapter 2, *CERN-2004-003-V-1* (2004)

[20] `https://twiki.cern.ch/twiki/bin/view/Atlas/WorkBookAtlasExperiment`

[21] *ATLAS Inner Detector Technical Design Report*, Volume 1, ATLAS Collaboration, *CERN/LHCC/97-16* (1997)

[22] Source images from `http://www.atlas.ch/photos/inner-detector-combined.html`

[23] *The ATLAS Inner Detector commissioning and calibration*, ATLAS Collaboration, Eur. Phys. J. **C70** (2010) `arXiv:1004.5293v2`

[24] *The ATLAS Transition Radiation Tracker (TRT) proportional drift tube: design and performance*, E. Abat et al., JINST **3** P02013 (2008)

[25] *ATLAS Calorimeter Performance Technical Design Report*, ATLAS Collaboration, *CERN/LHCC/96-40* (1997)

[26] *ATLAS Muon Spectrometer Technical Design Report*, ATLAS Collaboration, *CERN/LHCC/97-22* (1997)

[27] *The ATLAS Detector at the LHC*, ATLAS Collaboration, CERN-OPEN-2008-020 (2008)

[28] *Data Quality Monitoring Framework for the ATLAS Experiment at the LHC*, A. Corso-Radu *et al.*, Tech. Rep. IEEE Trans Nucl. Sci. 54 5, ATL-DAQ-CONF-2008-006 (2007)

[29] *The Detector Control System of the ATLAS Experiment*, A. Barriuso Poy *et al.*, J. Instrum., vol. 3, p. P05006, (2008)

[30] *The ATLAS Data Quality Defect Database System*, T. Golling, H. S. Hayward, P. U. E. Onyisi, H. J. Stelzer, P. Waller, Eur. Phys. J. C 72(4), 1960 (2012) `arXiv:1110.6119v2` [physics.ins-det]

[31] *The Data Quality WebTool*, `https://atlasdqm.cern.ch/atlaswebdq/`

[32] *The* SCT *Data Quality WebTool documentation*, `https://twiki.cern.ch/twiki/bin/viewauth/Atlas/SctDqWebTool`

[33] *Data Quality Information for 2010 and 2011 Data*, `https://twiki.cern.ch/twiki/bin/view/AtlasPublic/RunStatsPublicResults2010`

[34] *The* SCT *Data Quality Histograms documentation*, `https://twiki.cern.ch/twiki/bin/viewauth/Atlas/SctDqHistograms`

[35] *Expected performance of the ATLAS experiment: Detector, trigger and physics*, The ATLAS Collaboration, Tech. Rep., CERN- OPEN-2008-020, Geneva (2009)

[36] *The anti-kt jet clustering algorithm*, M. Cacciari, G. P. Salam, and G. Soyez, J. High Energy Phys., **04**, p.063, (2008)

[37] *Performance of the ATLAS Secondary Vertex b-tagging Algorithm in 7 TeV Collision Data*, The ATLAS collaboration, ATLAS-CONF-2010-042 (2010)

[38] *Commissioning of the ATLAS high-performance b-tagging algorithms in the 7 TeV collision data*, The ATLAS Collaboration, ATLAS-CONF-2011-102 (2011)

[39] *A new inclusive secondary vertex algorithm for b-jet tagging in ATLAS*, G. Piacquadio and C. Weiser, J.Phys.Conf.Ser. **119** 032032 (2008)

[40] *Calibrating the b-Tag Efciency and Mistag Rate of the SV0 b-Tagging Algorithm in 3 pb^{-1} of Data with the ATLAS Detector*, The ATLAS collaboration, ATLAS-CONF-2010-099 (2010)

[41] *Calibrating the b-Tag and Mistag Efficiencies of the SV0 b-Tagging Algorithm in 3 pb^{-1} of Data with the ATLAS Detector*, The ATLAS collaboration, ATLAS-COM-CONF-2010-103 (2010)

[42] http://lepsusy.web.cern.ch/lepsusy/ and references for combined results contained therein, LEP SUSY Working Group and the ALEPH, DELPHI, L3 and OPAL Collaborations.

[43] *First tuning of HERWIG/JIMMY to ATLAS data*, The ATLAS Collaboration, tech. rep., CERN, 2010. ATLAS-PHYS-PUB-2010-014.

[44] *GEANT4: A simulation toolkit*, GEANT4 Collaboration, S. Agostinelli et al., Nucl. Inst. Meth. **A506** 250303 (2003)

[45] *A Brief Introduction to PYTHIA 8.1*, T. Sjstrand, S. Mrenna and P. Skands, Comput. Phys. Comm. **178** 852 (2008) arXiv:0710.3820

[46] *ALPGEN, a generator for hard multiparton processes in hadronic collisions*, M.L. Mangano, M. Moretti, F. Piccinini, R. Pittau, A.D. Polosa, JHEP **0307** (2003) arXiv:hep-ph/0206293v2

[47] *The MC@NLO 3.2 Event Generator*, S. Frixione, B. R. Webber, arXiv:hep-ph/0601192 (2006).

[48] *HERWIG++*, M. Bahr et al. arXiv:0812.0529 [hep-ph] (2008).

[49] *SUSYHIT*, A. Djouadi, M. M. Muhlleitner and M. Spira, Acta Phys. Polon., **B38** (2007) 635-644.

[50] *PROSPINO*, R. H. W. Beenakker and M. Spira. http://www.ph.ed.ac.uk/~tplehn/prospino/.

[51] *A Search for Scalar Bottom Quarks from Gluino Decays in $\bar{p}p$ Collisions at $\sqrt{s}$ = 1.96 TeV*, The CDF Collaboration, arXiv:hep-ex/0512072v1 (2005).

[52] *Data-driven estimation of the QCD multijet background to SUSY searches with jets and missing transverse momentum at ATLAS using jet smearing*, S. Owen, tech. rep., CERN, ATL-COM-PHYS-2011-1066 (2011).

[53] *Update on the jet energy scale systematic uncertainty for jets produced in proton-proton collisions at* $\sqrt{s}$ *= 7 TeV measured with the ATLAS detector*, ATLAS Collaboration, ATLAS-CONF-2011-007 (2011)
The Multi-jet JES Uncertainty Provider, `https://twiki.cern.ch/twiki/bin/viewauth/AtlasProtected/MultijetJESUncertai`

[54] *Luminosity Determination Using the ATLAS Detector*, ATLAS Collaboration, ATL-ATLAS-CONF-2010-060 (2010).

[55] *Luminosity Determination in pp Collisions at* $\sqrt{s}$ = 7 TeV *using the ATLAS Detector in 2011*, The ATLAS Collaboration, tech. rep., CERN, ATLAS-CONF-2011-116 (2011).

[56] *Statistics: A Guide to the Use of Statistical Methods in the Physical Sciences*, R. Barlow, chapter 7, John Wiley and Sons (1989).

[57] *Data Analysis: A Bayesian Tutorial*, D. S. Sivia, Oxford University Press (1996).

[58] *Statistical methods used in ATLAS for exclusion and discovery*, D. Casadei, `http://arxiv.org/abs/1108.2288` (2011).

[59] *Presentation of search results: the* CL_s *technique*, A L Read, J. Phys. G **28**, 2693 (2002).

[60] *Search for supersymmetry in pp collisions at* $\sqrt{s}$ *= 7* TeV *in final states with missing transverse momentum, b-jets and no leptons with the ATLAS detector*, ATLAS Collaboration, ATLAS-CONF-2011-098 (2011).